January 2014

Design of Liquid Chromatography Systems for Capture and Purification

Lei Ling
Purdue University

Graduate School Form 30
(Updated 11/20/2014)

PURDUE UNIVERSITY
GRADUATE SCHOOL
Thesis/Dissertation Acceptance

This is to certify that the thesis/dissertation prepared

By Lei Ling

Entitled
Design of Liquid Chromatography Systems for Capture and Purification

For the degree of Doctor of Philosophy

Is approved by the final examining committee:

Nien-Hwa L. Wang

Osman A. Basaran

Michael T. Harris

Ernest R. Blatchley III

To the best of my knowledge and as understood by the student in the Thesis/Dissertation Agreement, Publication Delay, and Certification/Disclaimer (Graduate School Form 32), this thesis/dissertation adheres to the provisions of Purdue University's "Policy on Integrity in Research" and the use of copyrighted material.

Nien-Hwa L. Wang

Approved by Major Professor(s): _____

_____

Approved by: John A. Morgan 12/02/2014

Head of the Department Graduate Program Date

DESIGN OF LIQUID CHROMATOGRAPHY SYSTEMS FOR CAPTURE AND PURIFICATION

A Dissertation

Submitted to the Faculty

of

Purdue University

by

Lei Ling

In Partial Fulfillment of the

Requirements for the Degree

of

Doctor of Philosophy

December 2014

Purdue University

West Lafayette, Indiana

ACKNOWLEDGEMENTS

I would like to express the greatest appreciation to my advisor, Prof. Nien-Hwa Linda Wang, who has been kindly providing me with guidance, encouragement, and supports throughout my Ph.D. study. Without her detailed instructions and thoughtful concerns, it would not have been possible for me to publish well-organized articles, deliver elegant presentations, and accomplish the doctoral thesis. I would like to thank Prof. Osman A. Basaran, Prof. Michael T. Harris, and Prof. Ernest R. Blatchley III for serving as my advisory committee members and providing me with important comments and suggestions for my research.

This dissertation would not have been possible without the financial and technical support of Argonne National Laboratory, specifically provided by Dr. George F. Vandegrift, Dr. Artem V. Gelis, Dr. Amanda Youker, and Dr. Dominique C. Stepinski. I would like to acknowledge Dr. Pei-Lun Chung for laying the foundation of the study of molybdenum-99 recovery and Dr. Shuang Chen for helping me start up the study of rare earth elements separation. I sincerely appreciate the great effort made by Junjie Wang, Phoebe Chang, Lee-Wei Kao, and Shou Zhao helping me carry out experiments and generate critical results.

I would like to thank the colleagues in my research group, Dr. Hung-Wei Tsui, George Weeden Jr., Morgan Crawford, Nicholas Soepriatna, and Dean N. Straub. Their

friendship, support, and feedback always drove me towards the right direction. I also want to thank William Ehlhardt for his excellent work in developing a user-friendly interface for our simulation tool, which was extremely useful in my research.

Finally, I would like to extend my heartiest thanks to my parents and my wife, who have unconditionally devoted all their love to me. Their encouragement, support, and concern strongly backed me up, provided light to my life, and helped me overcome all the difficulties along the memorable journey of my Ph.D. study.

TABLE OF CONTENTS

Page

Page

Page

LIST OF TABLES

Table Page

LIST OF FIGURES

Figure Page

Figure Page

Figure Page

Figure Page

Figure Page

ABSTRACT

Ling, Lei. Ph.D., Purdue University, December 2014. Design of liquid chromatography systems for capture and purification. Major Professor: Nien-Hwa Linda Wang.

Liquid chromatography is a widely used technique for the separation of mixtures, especially for the components with low volatility or thermostability. It can be employed to analyze the types and amounts of components in a sample, or to separate sufficient amounts of substances for production. The performance of chromatography columns in separation can be affected by many factors, such as column length, particle size, flow rate, adsorption isotherms, reaction rates, etc. This results in challenges in design and optimization. Our objective is to understand the fundamentals of how the different variables act on the separation, and to develop systematic methods for designing different types of chromatography systems. Among the cases we investigated in the last five years, the following two are selected to be discussed in the thesis: (1) affinity chromatography for target component capture; (2) ligand-assisted elution chromatography for multi-component purification.

Affinity chromatography has been broadly applied in pharmaceutical industry for recovering a target from a complex mixture. When a feed solution is loaded onto a column, the target solute is selectively captured from the mixture by the sorbent. The challenge in designing a capture process is to maximize sorbent productivity, or minimize

column volume, while satisfying yield, loading time and pressure limit requirements. A general design method based on dimensionless groups has been developed for Langmuir isotherm systems. This method requires only the values of intrinsic parameters, which can be estimated from a small number of bench-scale experiments. Given feed conditions, loading time, and desired yield, the minimum column volume for capture and the maximum operating velocity can be determined readily without simulations. If the design requirements or material properties are varied, their effects on the column volume can be visualized graphically. This method has been verified by Protein A chromatography data for antibody purification, and is applicable to a wide variety of capture systems and production scales.

The general method was applied to design the TiO_2-packed columns for Mo-99 recovery from uranium fission products. Mo-99 is the parent of Tc-99m, which is used annually in 25 million diagnostic procedures worldwide. The minimum column volume and maximum operating velocity for capture were found rapidly using the general design method. Sensitivity analysis was performed to find the safety factor that needs to be considered in response to fluctuations in operating conditions and variations in material properties. Adaptive designs were also carried out for varied material properties, design constraints, and feed conditions.

The optimal stripping conditions for Mo recovery were found based on rate-model simulations. The capacities of multiple adsorption sites of TiO_2 were first estimated from frontal tests with various acids and bases. Appropriate models for Mo adsorption and desorption were then established based on the estimated capacities to simulate the stripping processes. The simulated Mo peaks and the experimental data

agreed closely with each other, indicating the models and parameters were validated. Further simulations were then performed to find the optimal conditions for achieving high product concentration and short stripping time.

When multiple target solutes need to be recovered and purified, an elution chromatography process is commonly used to achieve the goal. In some cases, however, the target solutes have very similar properties (e.g. enantiomers and lanthanides), and the sorbent may therefore have no selectivity for them. To achieve separation, a ligand which can form complexes with the solutes with different equilibrium constants is added into the mobile phase. If the complexed solutes adsorb, the overall selectivity approaches the sorbent selectivity for the complexed solutes at a high ligand concentration. If the complexed solutes do not adsorb, the overall selectivity is approximately the ratio of the sorbent selectivity for the free solutes to the ligand selectivity. Therefore, it will be favorable for the separation if the sorbent and the ligand have opposite affinity sequences for the solutes. A good resolution can be obtained only when the overall selectivity is high and the complexation has comparable strength as the adsorption of free solutes.

The mechanisms we understood from the ligand-assisted elution chromatography were used to develop the separation of lanthanides (Ln's), which are critical materials in many high-tech products. Current production of Ln's relies on multiple sequential and parallel solvent extraction steps, which require large amounts of harsh solvents and are environmentally hazardous. In this study, a ligand which can complex with Ln's with significantly different equilibrium constants was added to the mobile phase of chromatography to increase the overall selectivity. The elution process was demonstrated by separations of Pr, Nd and Sm on TiO_2 using ethylenediaminetetraacetic acid (EDTA)

as the ligand. Both purity and yield for each component were 95% or higher in linear gradient elution and step-wise elution. The ligand-assisted elution chromatography process is simpler than the conventional solvent extraction, because a series of Ln's products can be obtained from a single set of chromatography system. Moreover, this process has less impact on the environment, because the ligand is generally recognized as safe and can be mostly recycled. For large-scale production, the separation of Ln's can be carried out in a continuous mode with step-wise elution to save ligand and to increase sorbent productivity.

In both affinity and elution chromatography, the solute migration behaviors in the column depend on a variety of factors. Instead of trial and error with individual variables, a more sensible way for column design is to study the effect of dimensionless groups on capture or separation, and find out how the dominant groups are related to the output parameters (resolution, purity, yield, etc). This strategy allows one to understand better the fundamentals of chromatography behavior. Furthermore, the designs based on dimensionless groups can be readily generalized to other systems with similar mechanisms but different material properties and operating conditions.

CHAPTER 1. INTRODUCTION

1.1 Background

Liquid chromatography (LC) is a well-known separation technique which is widely used in pharmaceutical, chemical, and food industry. It is capable of separating complex mixtures with high purity and high yield at mild temperatures, which enable purification of nonvolatile or thermo-labile compounds. A typical LC system consists of a mobile phase, which can dissolve and carry the solutes, and a stationary phase (sorbent), which is packed into a column. The separation is based on differential partitioning of various components between the two phases. In general, the component with apparently lower affinity for the sorbent is likely to migrate faster in the column.

If the sorbent is only capable of interacting with a specific solute in the feed, the LC system can be used to selectively capture and recover the target solute. A good example of this application is affinity chromatography (Cuatrecasas and Anfinsen 1971), in which the target solute can strongly but reversibly bind with the sorbent, whereas the impurities do not adsorb. The captured solute can be eluted from the column by a stripping agent, which can either displace the target solute, or lower the affinity of the sorbent for the target solute. To date, the technique of affinity chromatography has been used in Protein A chromatography for monoclonal antibody (mAb) purification (Hober et al. 2007), immobilized metal affinity chromatography (IMAC) for protein and nucleic

acid purification (Porath et al. 1975; Murphy et al. 2003), and capture chromatography for the recovery of medical isotope precursor Mo-99 (Ling et al. 2013).

In many cases, however, we aim to purify multiple target products rather than capture a single target solute. These products may have very similar properties and cannot be efficiently separated by commercially-available sorbents. One approach to solve this problem is to add a ligand, which can form complexes with the solutes, into the mobile phase. If the complexed solutes can adsorb with different affinity for the sorbent, the separation can be obtained based on the sorbent selectivity for the complexed solutes. If the complexed solutes do not adsorb, the solute that binds more strongly with the ligand is likely to elute earlier, on condition that the complexation and the adsorption of free solutes have comparable strengths. The principle of ligand-assisted chromatography has been used in separations of chiral solutes (Owen et al. 1997; Ma et al. 2009), rare earth elements (Spedding et al. 1950; Powell 1964; Moore 2000), and actinides (Lowe et al. 1971; Jenkins 1979).

In the aforementioned LC processes for capture and purification, the performance of chromatography in separation can be affected by many factors, such as column length, particle size, flow rate, diffusivity, feed concentration, adsorption isotherms, and reaction equilibrium constants. As a result, designing LC processes is always a challenging task. To date, most of the designs are based on experimental trial and error, which is straightforward to carry out but is costly and labor-intensive. Numerous variables need to be tested individually at different levels to determine the optimum operating conditions. A number of methods were developed for column scale-up based on bench-scale data (Rudge and Ladisch 1986; Crittenden et al. 1991; Garcia et al. 1999), but they were

unable to determine the optimal column volume and operating conditions that can satisfy specific requirements of feed volume, loading time, capture yield, and pressure drop. In addition, they are not adaptive to variations in feed concentration, adsorption isotherms, and loading time. Therefore, it is highly beneficial to develop systematic, efficient, and adaptive methods for designing LC processes for capture and purification.

1.2 Objectives

The overall objective of this dissertation was to gain a fundamental understanding of how different variables can affect chromatography separations, and to develop systematic methods for designing LC systems for capture and purification. Specifically, we aimed to: (1) develop a systematic and general design method for target solute capture (Chapter 3); (2) apply this method to designing affinity columns for the recovery of medical isotope precursor, Mo-99, and find optimal conditions for stripping Mo-99 from the column (Chapter 4); (3) identify the key factors that affect the ligand-assisted elution chromatography processes for multi-component purification (Chapter 5); (4) apply the knowledge to developing high-purity, high-yield, and cost-effective lanthanides separation processes (Chapter 6).

1.3 Research Methodologies

In order to develop a general design method for capturing a target solute, we first incorporated variables that can affect frontal wave spreading into proper dimensionless groups. These groups, which represent various mass transfer rates relative to convection rate, were derived from coefficients of differential mass-balance equations and boundary

conditions for chromatography systems. We then identified the key dimensionless group controlling the wave spreading and the dimensionless group representing the column utilization. The relations between these two groups under various design constraints (yield, loading time, pressure drop) were used to generate universal solutions of minimum column volume as a function of material properties, design constraints, feed concentration, and production scales. This method was validated by a variety of literature data of antibody purification, and was then used to find the desired column volume, column length, and operating velocity for Mo-99 capture with specific requirements of capture yield, loading time, pressure drop, and batch size.

Design of Mo stripping processes was based on the understanding of how Mo adsorbs and desorbs in a TiO_2-packed column. Appropriate adsorption and mass transfer models were first established based on hypothetical mechanisms, which were verified by the fact that the rate-model simulation results agreed closely with the experimental data. Additional simulations were then carried out based on the validated models and parameters to elucidate the desirable Mo stripping conditions for increasing product concentration and decreasing stripping time.

Study of ligand-assisted elution chromatography started with unearthing representative literature data and finding the intrinsic parameters of adsorption, mass transfer, and reactions. Simulations were implemented to verify the models and parameters, and to generate effluent histories and column profiles under various conditions. The simulation results were then classified based on dimensionless groups, from which the key factors that affect the performance in multi-component purification were identified. The knowledge gained in this study led us to find the desirable ligand

type, ligand concentrations, and operating conditions for lanthanides separation in a TiO_2-packed column. The purity and yield were further improved by using linear gradient elution and step-wise elution strategies.

CHAPTER 2. MATERIALS AND METHODS

2.1 Materials

In the study of molybdenum-99 (Mo-99) recovery from uranium fission products, uranium metal, concentrated nitric acid (70%, Sigma Aldrich, St. Louis, MO), and concentrated sulfuric acid (96%, Sigma Aldrich, St. Louis, MO) were used to prepare uranyl sulfate solutions. Stable Mo was added as sodium molybdate, which was also from Sigma Aldrich. Mo-99 was obtained from a spent Tc-99m generator from Hot Shots Nuclear Medicine using 1 M NH_4OH. Mo-99 in 1 M NH_4OH was evaporated to dryness and re-dissolved in a uranyl sulfate solution containing the proper amount of stable Mo (10^{-4}–10^{-1} mM). Sachtopore S110 (TiO_2 with 110 μm particles and 60 Å pores) manufactured by ZirChrom Separations (Anoka, MN) was used as the sorbent for Mo uptake. Sodium phosphate, sodium hydroxide, and nitric acid (68-70%) were ordered from Mallinckrodt (Paris, KY), and were used to quantify the adsorption sites of TiO_2.

In the study of lanthanides separation, praseodymium (III) nitrate hexahydrate ($Pr(NO_3)_3 \cdot 6H_2O$), neodymium (III) nitrate hexahydrate ($Nd(NO_3)_3 \cdot 6H_2O$), and samarium (III) nitrate hexahydrate ($Sm(NO_3)_3 \cdot 6H_2O$) were ordered from Sigma-Aldrich (St. Louis, MO). The ligands ethylenediaminetetraacetic acid (EDTA) and diethylenetriaminepentaacetic acid (DTPA) were also purchased from Sigma-Aldrich (St. Louis, MO), whereas citric acid was purchased from J. T. Baker (Phillipburg, NJ). The

sorbent Sachtopore 80 (TiO_2, 80 μm, 60 Å) was manufactured by ZirChrom Separations (Anoka, MN). Sodium hydroxide (NaOH), nitric acid (HNO_3), and ammonium hydroxide (NH_4OH) were purchased from Mallinckrodt Baker (Paris, KY). Distilled Deionized Water (DDW) was obtained from a Millipore (Bedford, MA) four stage cartridge system.

2.2 Column packing and characterization

For a given column size, the amount of sorbent was weighed and placed in a beaker. Water was added to the sorbent to form a 20% (v/v) slurry. The slurry was agitated by a digital vortex mixer (Fisher Scientific, Waltham, MA) at 1000 rpm for 3 minutes to remove air from sorbent pores and any impurities that are soluble in water. After the sorbent settles, the excess liquid was decanted. The rinsing and decanting steps were repeated two more times. After the third cycle, the sorbent was soaked in water for 24 hours, and then the excess liquid was decanted to obtain an 80% (v/v) slurry.

The pump, tubing, and column adjusters were first filled with water to remove any bubbles trapped in the flow path. Water was pumped upward through an empty glass column until the level was 0.5 cm above the bottom. The bottom was then disconnected from the pump and plugged. The 80% (v/v) slurry was uniformly mixed and poured into the column. Water was added to the slurry container to transfer any remaining sorbent to the column. After the water level in the column reached the top and sorbent particles settle down, the column was reconnected with the pump. More water was pumped downward through the packed bed at a superficial velocity of 10 cm/min for at least 1 hour. When no more shrink was observed from the packed column, the velocity was

lowered to 1 cm/min. The packing-length adjuster was lowered to the surface of sorbent layer and then tightened.

After the column was packed, pulse tests were performed to measure the bed void and porosity using an ÄKTA explorer 100 unit (GE Healthcare, Piscataway, NJ). The column was presaturated with 0.1 M NaOH, which prevented the adsorption of the tracers. The bed void ε_b was measured by injecting a 0.2 ml 1 g/L albumin pulse through the column, and the total void ε_t by 1 M $NaNO_3$. The UV wavelengths used for detection were 215 nm for albumin and 250 nm for $NaNO_3$. The values of ε_b and ε_t were determined from the retention volumes of albumin ($V_{R,A}$) and sodium nitrate ($V_{R,S}$), the pulse volume (V_P), the total extra-column dead volume (V_D, including the dead volumes of pump, tubing, valves, and column caps), and the column volume (V_C), as shown in Eq. 2.1a and Eq. 2.1b. The particle porosity ε_p was calculated from ε_b and ε_t, Eq. (2.1c).

$$\varepsilon_b = \frac{V_{R,A} - V_D - 0.5V_P}{V_C} \tag{2.1a}$$

$$\varepsilon_t = \frac{V_{R,S} - V_D - 0.5V_P}{V_C} \tag{2.1b}$$

$$\varepsilon_p = \frac{\varepsilon_t - \varepsilon_b}{1 - \varepsilon_b} \tag{2.1c}$$

To quantify the various adsorption sites of the titania sorbent, a freshly packed column was washed successively with 0.1 M NaOH and 0.11 M HNO_3 to remove any impurities adsorbed on different sites. The column was then rinsed with distilled water to remove the adsorbed HNO_3 until the outlet conductivity dropped to 0.002 ms/cm. The clean column was loaded again with 0.11 M HNO_3 until the conductivity reached a

plateau, and the breakthrough volume (V_{br}) was used for estimating the capacity (based on column volume) of the Brønsted Base sites as follows:

$$q_{Sites} = \frac{C_{Fr}(V_{br} - V_D - V_C\varepsilon_t)}{V_C} \quad (2.2)$$

where C_{Fr} is the concentration of the agent used in the frontal tests for estimating the adsorption sites capacities.

After being rinsed with water, the column was loaded with 0.1 M NaOH until a plateau was formed. The breakthrough volume indicated the total capacity of the BA sites and the LA sites. The value was also calculated using Eq. (2.2). The column was then loaded successively with 0.11 M HNO_3, 0.1 M NaOH and 0.11 M HNO_3. The changes in conductivity served as additional supports for the capacity estimation. A water wash step was then conducted to clean up the acid in the column, and was followed by a frontal of 0.1 M Na_3PO_4. The breakthrough volumes were used for estimating the respective capacities of the LA sites and the BA sites.

2.3 Recovery of molybdenum from uranyl sulfate solutions

2.3.1 Preparation of uranyl sulfate solutions

Uranium metal plates (~150 g each) were dissolved in 8 M nitric acid using a heating mantle, reaction kettle, kettle cover, and reflux condenser. The solution was dried, and the product was placed directly in a round bottom flask, which was connected to a rotary evaporator. Sulfuric acid (1-18 M) was added directly to the uranyl nitrate solution to form uranyl sulfate. The rotary evaporator has a water-cooled condenser that was kept under a vacuum of 80 mbar. An oil bath was used to heat the solution to drive off nitric

acid to form uranyl sulfate. Ion chromatography measurements with a Dionex AS18 anion-exchange (quarternary ammonium) column showed that about 1 to 5% of the initial amount of nitrate remained in the solution after rotary evaporation.

2.3.2 Batch equilibrium tests

The uptake of Mo as a function of Mo concentration was determined by contacting 1 mL of a Mo-99 spiked aqueous solution with a known amount (10 ± 1 mg) of sorbent for 24 hours at 60 °C using a thermostated shaker bath. The aqueous solutions contained 10^{-4}–10^{-1} mM Mo in 0.38 M, 0.55 M, and 0.64 M uranyl sulfate, which was the model fission source. The pH was adjusted to 1, under which other potential fission products are unable to adsorb. After equilibration, the solution was withdrawn and filtered using a syringe fitted with a 0.22 μm pore size PVDF membrane filter. Blank experiments had shown that the filter does not uptake Mo-99. The amount of radioactivity remaining in the aqueous samples was determined using a germanium detector. Mo-99 was quantified by measurement of its 739 keV ray. Blank tests were done in parallel to correct the effect of decay. The errors in the measurements were less than 10%. The Mo concentration in the solid phase in equilibrium with the final concentration in the solution can be calculated as follows:

$$q = \frac{(C_o - C_s)V}{W}\rho_{packing} \tag{2.3}$$

where C_o is the initial Mo concentration in the solution; C_s is the final Mo concentration in the solution; q is the Mo concentration in the solid phase in equilibrium with the final concentration in the solution; V is the volume of the solution; W is the weight of dry

sorbent; $\rho_{packing}$ is the packing density of the sorbent, which is defined as the ratio of the sorbent dry weight to the packing volume. The unit of q is mmol/L packing volume. For the titania sorbent used in this study, $\rho_{packing}$ is nearly a constant of 1300 g/L.

2.3.3 Molybdenum loading and stripping tests

The Mo loading tests were performed on freshly packed titania columns at 60 °C, which is close to the temperature of the real nuclear broth. The feed solutions contained Mo as Na_2MoO_4 and tracer Mo-99 in uranyl sulfate at pH 1. The column was pre-equilibrated with 10 column volumes of 0.05 M H_2SO_4, and the feed solutions were then loaded in the upflow direction for two hours. After the feed loading, the columns were washed in the upflow direction, with 10 column volumes of 0.05 M H_2SO_4 and then with 10 column volumes of distilled water. Mo was then stripped from the column using 30 column volumes of 1 M NH_4OH or 0.1 M NaOH in the downflow direction. Eight to fifteen fractions of the effluent were collected and then gamma counted using a germanium detector.

2.4 Separation of lanthanides

2.4.1 Displacement test

A freshly packed titania column (1.16 cm *ID* × 49 cm *L*) was rinsed with 0.2 M NaOH, 0.2 M HNO_3, and DDW, to remove any impurities adhering to the sorbent. A 30 mL solution of Pr, Nd and Sm (0.02 N for each element) was then fed into the column. A solution of 0.05 M HNO_3 was pumped into the column to displace the adsorbed lanthanides. The linear velocities for loading and displacement were both 0.2 cm/min. Pr,

Nd, and Sm were detected using an online UV-vis detector at 444 nm, 575 nm, and 401 nm, respectively. No interference was observed. The breakthrough of HNO_3 front was monitored using an online pH sensor. After the bands of Pr, Nd, and Sm were displaced by the HNO_3 front, the displacement was stopped and the column was washed with DDW for 50-100 column volumes until the pH returned to 6 and the conductivity dropped to 0.002 mS/cm, which was the baseline for DDW.

2.4.2 Ligand-assisted elution test

In ligand-assisted elution tests, the S80 column (49 cm *L* × 1.16 cm *ID*) was first preloaded with a ligand solution, the pH of which was adjusted to a target value by titrating with NH_4OH. The lanthanides (Pr, Nd, and Sm) were dissolved in the same ligand solution, and the concentrations were 0.02 N for each element. The column was then fed with 30 mL of the lanthanide solution, and subsequently eluted by the ligand solution. The linear velocities for loading and elution were both 0.2 cm/min. Pr, Nd, and Sm were detected at 444 nm, 575 nm, and 404 nm, respectively.

Diethylene triamine pentaacetic acid (DTPA, pH 9), ethylenediaminetetraacetic acid (EDTA, pH 9), and citric acid (pH 7) were tested for isocratic elution, whereas EDTA (pH 9) was also tested for linear gradient elution and stepwise elution. In isocratic elution tests, the eluant was the same as the ligand solution used for preloading. In gradient elution, the ratio of the two pumps was programmed as a function of time, so that the ligand concentration could increase linearly from the preloading concentration to a target value. In stepwise elution, the pump ratio was adjusted at certain times to create step changes of ligand concentration in the eluant. Prior to switching to a different ligand

system, the column was washed with 0.2 M NaOH, 0.2 M HNO_3, and then DDW, until the pH returns to 6 and the conductivity drops to 0.002 mS/cm.

2.4.3 Frontal tests for isotherm estimation

The adsorption isotherms for the lanthanides were obtained by multiple frontal tests using a small S80 titania column (4.8 cm *L* × 1.5 cm *ID*), which was washed in sequence with 0.2 M NaOH, 0.2 M HNO_3, and DDW prior to the tests. The isotherm measurement was first conducted in the absence of ligand. The solutions prepared for the isotherm measurement were 0.002 N, 0.005 N, 0.01 N, 0.02 N, 0.05 N, and 0.1 N of Pr, Nd, and Sm in DDW. A more concentrated solution was loaded to the column once the sorbent was equilibrated with a less concentrated solution. After all the concentrations were tested for one element, the column was washed with 0.2 M HNO_3 and DDW, and then used for a different element. The lanthanide concentration in the sorbent, which is in equilibrium with a solution phase concentration, can be calculated as follows:

$$q_{i+1} = q_i + \frac{(C_{i+1} - C_i)V_{br,i+1}}{V_C} \tag{2.4}$$

where C_i and C_{i+1} are the solution phase concentrations at the i^{th} and $(i+1)^{th}$ frontals; q_i and q_{i+1} are the sorbent phase concentration in equilibrium with C_i and C_{i+1}, respectively. When i=0, C_i and q_i are both zero. $V_{br,i+1}$ is the net breakthrough volume (dead volume and void volume are subtracted) for the $(i+1)^{th}$ frontal.

The measurement of adsorption isotherm of lanthanides on the ligand-loaded sorbent was conducted on the same column (4.8 cm *L* × 1.5 cm *ID*), which was preloaded with 0.4 M EDTA (pH 9). Before the lanthanides were loaded, the system was washed by

1 column volume (V_C) of DDW to avoid complexation of lanthanides and EDTA in the tubing. The solutions prepared for the isotherm measurement were 0.001N, 0.002 N, 0.005 N, 0.01 N, 0.02 N, 0.05 N, and 0.1 N of Pr, Nd, and Sm in DDW. Unlike the ligand-free isotherm tests, the column was regenerated by the 0.4 M EDTA solution and washed by 1 V_C of DDW each time before it was loaded with a different concentration or a different element. As a result, the sorbent phase lanthanide concentration can be calculated by

$$q_i = \frac{C_i V_{br,i}}{V_C} \tag{2.5}$$

2.5 Versatile separation and reaction (VERSE) model and simulations

VERSE is a well-known general rate model developed by Wang and associates in 1991 (Berninger et al. 1991). It takes into account multiple mass-transfer effects (axial dispersion, film mass transfer, intra-particle pore and surface diffusion) in chromatography, and incorporates a variety of models for adsorption (Langmuir, Bi-Langmuir, Freundlich, Mass action, etc) and reactions (aggregation, decomposition, isomerization, etc). To date, a simulation program with a user-friendly interface has been developed to numerically solve the partial differential mass balance equations in the bulk phase and the particle phase. A variety of chromatography processes (frontal, elution, displacement, carousel, simulated moving bed, etc) can be simulated by specifying the boundary and initial conditions differently. The effluent histories and dynamic column profiles can be displayed and exported when the simulations are completed. The figures

and animations generated by the simulations are important for verifying the models and the separation mechanisms.

All the simulation results shown in this dissertation, unless otherwise noted, were based on the pore diffusion model. The assumptions and equations have been reported elsewhere (Berninger et al. 1991) and are elucidated in Appendix A. The equations of Langmuir or Bi-Langmuir models were used to correlate the adsorption isotherms. The Chung and Wen correlation (Chung and Wen 1968) was used to estimate the axial dispersion coefficient. The Wilson and Geankoplis correlation (Wilson and Geankoplis 1966) was used to estimate the film mass-transfer coefficient.

The pumps, valves, tubing, and caps outside the packed column can be considered as a combination of a completely stirred tank reactor (CSTR) and a plug flow vessel. The CSTR results in additional wave spreading, whereas the plug flow only causes a delay in wave migration. In the simulations, the extra-column dead volume was modeled by two equal-sized CSTRs attached at the inlet and the outlet of a column, respectively. The equation used to describe the concentration change in a CSTR is:

$$V_D \frac{dC_{out,i}}{dt} = F\left(C_{in,i} - C_{out,i}\right) \tag{2.6}$$

where V_D is the extra-column dead volume; F is the flow rate; $C_{in,i}$ and $C_{out,i}$ are the concentrations of species i at the CSTR inlet and outlet, respectively. The CSTR mixing behavior in the dead volume has been justified by Wang and associates in a variety of previous studies (Xie et al. 2002; Yu et al. 2006; Chung et al. 2010; Ling et al. 2013).

CHAPTER 3. A GENERAL METHOD FOR DESIGNING AFFINITY CHROMATOGRAPHY FOR TARGET CAPTURE

3.1 Introduction

Affinity chromatography is widely used for selectively recovering a target solute from a complex mixture (Cuatrecasas and Anfinsen 1971). The separation is based on specific interactions between a sorbent and a solute. Examples are immobilized metal affinity chromatography (IMAC) for protein fractionation (Porath et al. 1975), Protein A chromatography for antibody purification (Hober et al. 2007), and capture chromatography for medical isotope precursor recovery (Ling et al. 2013).

In general, an affinity chromatography process involves four steps: (1) pre-equilibrating the column with a buffer; (2) loading the feed and capturing the target solute; (3) washing the column with the buffer to remove non-adsorbing impurities; and (4) eluting the target solute using a stripping agent. The most challenging aspect of designing a capture process is the selection of column size and operating velocity to achieve high yield and high column utilization, while satisfying the requirements of loading time and pressure limit. Achieving these goals by experimental trial and error can be costly and time-consuming. Furthermore, the results of a specific design may not apply if the feed concentration, feed volume, loading time, operating velocity, column length, or sorbent are different from those in the tested case. It is also difficult to predict how material

properties, such as particle size, particle porosity, bed void fraction, adsorption isotherm, and intra-particle diffusivity, affect the column volume or the operating velocity.

The yield and column utilization in a capture process depend on the shape of the frontal wave, which depends on the adsorption isotherm and mass transfer rates. For linear isotherm systems, Rosen considered film diffusion and intra-particle diffusion effects. He obtained an analytical solution of the effluent concentration as a function of the loading time for sufficiently long columns (Rosen 1952; 1954). For nonlinear isotherm systems, most of the published design methods are based on the solutions for "constant-pattern" waves, and apply only if the feed volume and the column length are sufficiently large for the frontal wave to reach a constant pattern (Michaels 1952; Hritzko et al. 2000; Naja and Volesky 2006; Moreno-Pirajan et al. 2008). In many affinity chromatography systems, a constant pattern is unattainable when the column length, the feed volume, or the loading time is small. For high affinity systems with highly non-linear "rectangular" adsorption isotherms, Carta and coworkers obtained correlations between the dynamic column capacity and the solute residence time (Perez-Almodovar and Carta 2009; Carta 2012). The correlations, which are valid for constant pattern or non-constant pattern systems, can be used to predict the maximum loading time for a given column if the breakthrough concentration and the velocity are specified.

In this study, a general and efficient method was developed for designing affinity chromatography systems with Langmuir isotherms (Ling et al. 2014). The goal of the design method is to achieve the desired yield and loading time while minimizing the column volume for either constant pattern or non-constant pattern systems. The method was tested with published affinity chromatography data (Ng. et al. 2012; Novasep

product data profile; Miyahara et al. 2012; Katoh et al. 2007; Perez-Almodovar and Carta 2009). We also aimed to understand how yield, loading time, material properties, feed concentration and feed volume affect the minimum column volume required for capture.

The design method is based on key dimensionless groups derived from rate model equations. It is applicable to any Langmuir isotherm systems with different scales. Only certain material properties (adsorption isotherm parameters, bed void fraction, diffusivity, and porosity) are needed for the design and they can be obtained from a small number of bench-scale experiments. The conditions for the formation of constant pattern waves were found. The effects of material properties and design criteria (feed concentration, feed volume, loading time, and yield) on the column volume were elucidated. In general, high productivity can be achieved with a small loading time. A small column volume for capture can be achieved with a high feed concentration, a high equilibrium capacity, and a small diffusion time relative to the loading time.

3.2 Fundamentals of the design method

3.2.1 Key dimensionless groups

During the feed loading step, the frontal wave spreads as a result of various mass transfer effects. This wave spreading prevents complete utilization of the equilibrium column capacity if all of the target solute in the feed needs to be captured. Column utilization is related to the degree of wave spreading and dimensionless breakthrough concentration (Fig. 3.1a-f), which is linked to the capture yield as discussed in Section 3.2.3. Wave spreading can be affected by many factors, such as the sorbent particle radius (R), the column length (L), the bed void (ε_b), the particles porosity (ε_p), the superficial

velocity (u_s), the feed concentration (C_f), the Langmuir isotherm parameters (a and b), the intra-particle diffusivity (D_p), the axial dispersion coefficient (E_b), and the film mass transfer coefficient (k_f). Studying the individual effects of these factors on wave spreading can be quite tedious. To reduce the number of variables, several dimensionless groups were used for characterizing column utilization and the effects of mass transfer and thermodynamic sharpening on wave spreading.

The general rate-model equations in terms of dimensionless variables for batch and simulated moving bed chromatography have been reported elsewhere (Berninger et al. 1991). The equations were solved numerically for specific isotherms and operating conditions. The solutions of the effluent history and the column profiles are governed by the dimensionless groups in the differential mass-balance equations, the isotherm equations, and the boundary conditions. The resulting independent dimensionless groups related to convection, axial dispersion, film diffusion, and intra-particle diffusion are Pe_b, N_f, and N_D. The definition and the physical significance of each group are summarized in Table 3.1. The spreading of a frontal wave is related to the three dimensionless groups.

For low-pressure chromatography systems (R>20 μm), it has been found that N_D usually ranges from 0.1 to 1, while Pe_b and N_f are in the magnitudes of 10^2 to 10^3, indicating that intra-particle diffusion, or the value of N_D, controls the wave spreading (Ling et al. 2013).

Thermodynamic sharpening, which counters diffusional spreading, also affects the shape of a frontal wave. Its effects are controlled by the dimensionless group bC_f in the Langmuir isotherm equation.

Table 3.1 Key dimensionless groups for designing affinity chromatography processes

Dimensionless groups	Physical significance	Definitions
Pe_b	$\frac{\text{Convection rate}}{\text{Axial dispersion rate}}$	$\frac{u_s L}{E_b \varepsilon_b}$
N_f	$\frac{\text{Film diffusion rate}}{\text{Convection rate}}$	$\frac{3L(1-\varepsilon_b)k_f}{Ru_s}$
N_D	$\frac{\text{Intra-particle diffusion rate}}{\text{Convection rate}}$	$\frac{(1-\varepsilon_b)\varepsilon_p D_p L}{u_s R^2}$

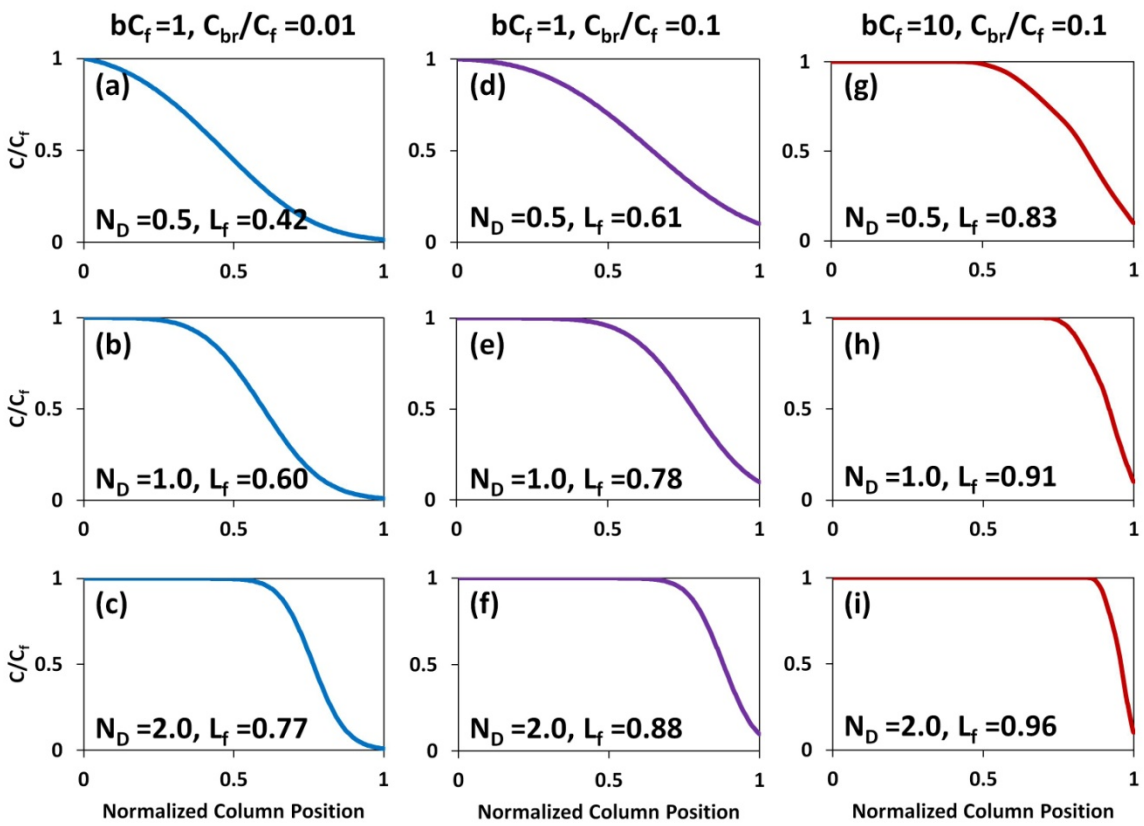

Figure 3.1. Dimensionless column profiles at the end of feed loading for different values of N_D, bC_f, and C_{br}/C_f.

$$q_f = \frac{aC_f}{1+bC_f} = a^*C_f \tag{3.1}$$

where q_f is the equilibrium concentration of the adsorbed solute (adsorbed solute per packing volume) at a feed concentration of C_f. The Langmuir a value is also defined based on per packing volume; a^* is defined as $a^*=a/(1+bC_f)$, which can be considered as an effective a value at a specific concentration for a nonlinear isotherm system. The group bC_f can be considered as an "overloading" factor or a “thermodynamic wave sharpening” factor. As the bC_f value increases, the frontal wave becomes sharper, as shown in the comparison between Fig. 3.1d-f and Fig. 3.1g-i. For this reason, column utilization is also affected by bC_f in addition to N_D and the breakthrough concentration**.**

The column utilization can be described by another dimensionless group, the loading fraction L_f, which is defined as the ratio of the dynamic loading amount to the equilibrium loading capacity at a specific feed concentration C_f:

$$L_f \equiv \frac{C_f V_f}{q_f V_C} \tag{3.2}$$

where V_f is the feed volume, and V_C is the column packing volume.

The loading fraction for a Langmuir isotherm system can be written as follows:

$$L_f = \frac{(1+bC_f)V_f}{aV_C} = \frac{V_f}{a^*V_C} = \frac{u_s t_L}{a^* L} \tag{3.3}$$

where t_L is the loading time for a feed volume of V_f. When the equilibrium capacity at the given feed concentration C_f is fully utilized, the value of L_f is 1.

3.2.2 Constant breakthrough-limit curve (BL curve)

As shown in Fig. 3.1d-f, the loading fraction L_f is related to N_D at a fixed breakthrough concentration of 10% of the feed concentration (C_{br}/C_f =0.1). As N_D increases, the frontal wave is less spread and L_f increases. The curve relating L_f to N_D at a fixed breakthrough concentration is defined as a constant breakthrough limit curve, or BL curve (Fig. 3.2a). For a BL curve to approach L_f =1, the frontal wave must have little spreading, which requires a large value of N_D (>>1). Along the BL curve, the breakthrough limit C_{br}/C_f =0.1 is satisfied. Above the curve, C_{br}/C_f is greater than 0.1, whereas below the curve, C_{br}/C_f is less than 0.1.

As shown in Fig. 3.1, the loading fraction is also affected by C_{br}/C_f and bC_f in addition to N_D, so that the BL curve is a function of both C_{br}/C_f and bC_f (Fig. 3.2b). When C_{br}/C_f is reduced from 0.1 to 0.01, the loading fraction L_f decreases for the same N_D, and the BL curve shifts downwards. When bC_f increases from 1 to 10, the frontal wave becomes sharper, L_f increases for the same N_D, and the BL curve shifts upwards.

3.2.3 Relation between breakthrough limit and capture yield

In the previous section, the loading fraction is related to the breakthrough limit instead of the yield, because the breakthrough concentration is easier to be identified from experiments or rate-model simulations than the capture yield. In general, a lower breakthrough concentration results in a higher capture yield, but a lower loading fraction (Fig. 3.2b). One may need to consider a trade-off between the yield and the column utilization in cost optimization. For this reason, the yield is related to the breakthrough limit in Fig. 3.3.

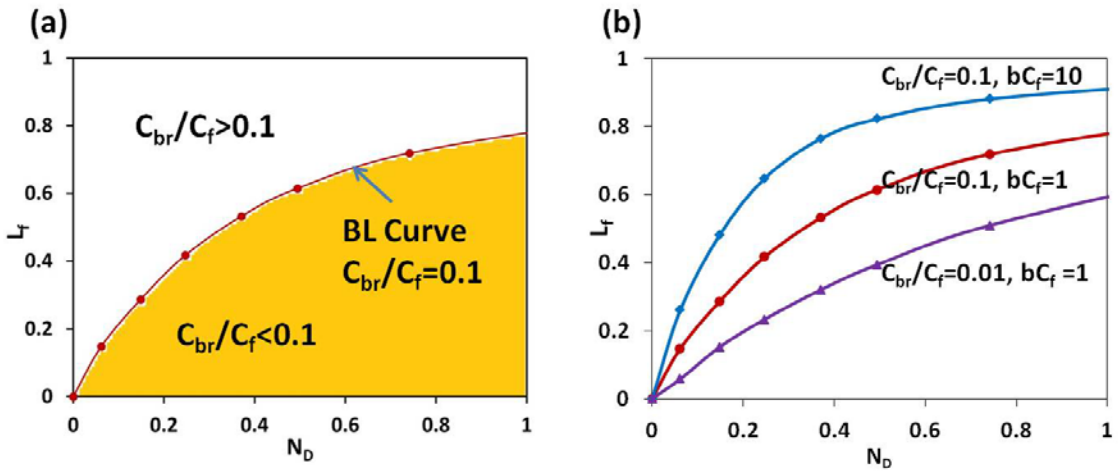

Figure 3.2. (a) Constant breakthrough limit curve (BL curve) for bC_f=1 and C_{br}/C_f =0.1.

(b) BL curves for various bC_f and C_{br}/C_f values.

For linear isotherm systems (bC_f=0), there is no thermodynamic sharpening. As the breakthrough limit C_{br}/C_f increases, the yield decreases as expected (Fig. 3.3a). At a fixed breakthrough limit, the yield also depends on N_D, which affects wave spreading. As N_D increases, the frontal wave becomes sharper, and the yield loss becomes smaller.

For nonlinear isotherm systems (bC_f>0), the shape of a frontal wave also depends on thermodynamic sharpening effects, or the value of bC_f. At a fixed breakthrough limit, a larger bC_f value results in a sharper frontal wave and a smaller yield loss (Fig. 3.1). Therefore, the curve relating the yield to the breakthrough limit shifts upward as bC_f increases (Fig. 3.3a-d). For bC_f >30, no further changes in Fig. 3.3d are observed. Apparently, thermodynamic sharpening effects approach a limit.

In general, a larger bC_f value allows a larger breakthrough limit and a smaller N_D value for achieving the same yield. For a system with a known bC_f value, for example, bC_f =10, one can find from Fig. 3.3c that the capture yield within a wide N_D range ($0.1<N_D<1$) is above 97% for C_{br}/C_f=0.15, above 98% for C_{br}/C_f=0.1, and above 99% for C_{br}/C_f=0.05. If the yield requirement is, for example, greater than 98%, one should refer to the BL curve for C_{br}/C_f=0.1 and bC_f=10, which is shown in Table 3.2 in Section 3.3.3. For any bC_f values not shown in Fig. 3.3, one can apply linear interpolation to the curves in Fig. 3.3a-d to estimate the C_{br}/C_f value for a desired yield.

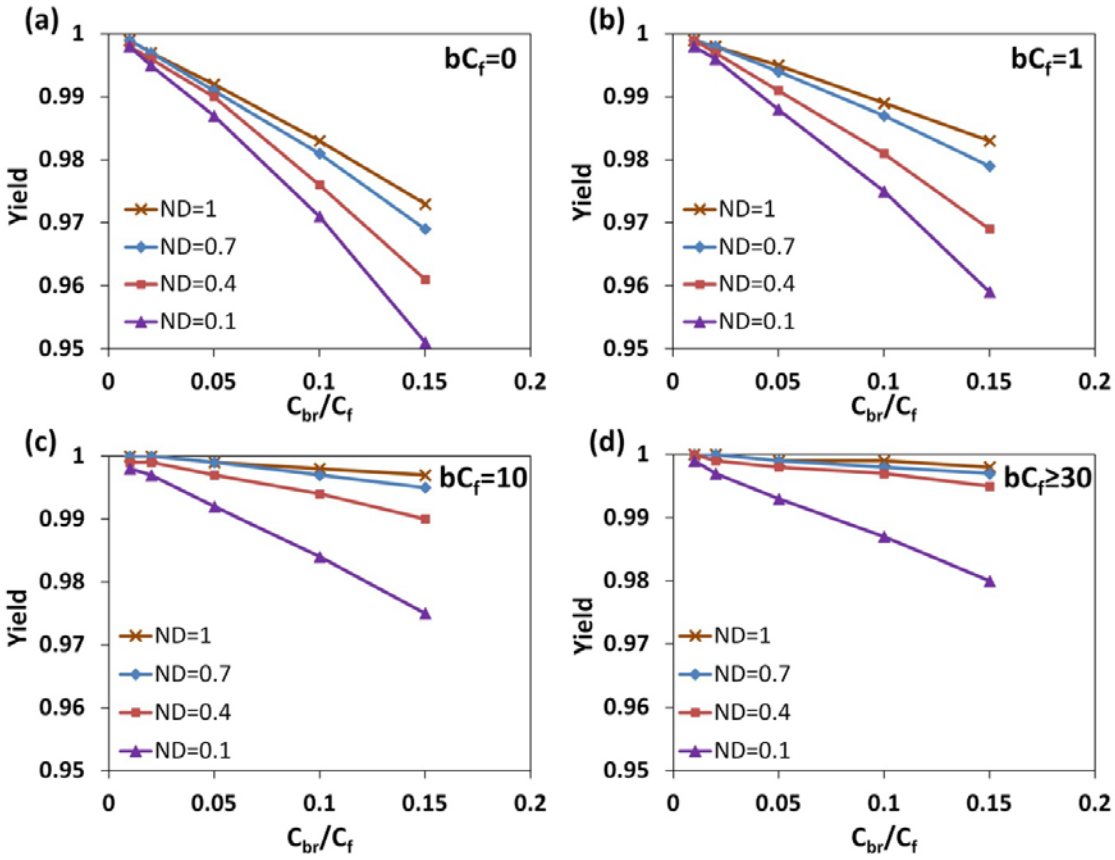

Figure 3.3. Relation between the capture yield and the breakthrough limit C_{br}/C_f for different values of bC_f and N_D.

3.2.4 Constant loading-time curve (LT curve)

In affinity chromatography, some target solutes such as proteins or radioactive isotopes are unstable, and must be captured within a short loading time. If a loading time t_L is fixed, and the feed concentration C_f is known, one can derive from Eq. (3.3) and the definition of N_D in Table 3.1 that the product of L_f and N_D is a constant.

$$N_D L_f = \frac{(1-\varepsilon_b)\varepsilon_p D_p}{R^2}\frac{(1+bC_f)}{a}t_L = \frac{(1-\varepsilon_b)\varepsilon_p D_p}{a^* R^2}t_L \equiv t^* \tag{3.4}$$

where t^* is defined here as the dimensionless loading time. The hyperbolic curve of L_f vs. N_D is defined here as a constant loading-time curve, or LT curve (Fig. 3.4). Along this curve, t^* is fixed, while the residence time L/u_s and the breakthrough limit C_{br}/C_f are varied. As the loading time t_L increases, t^* increases, the curvature of the LT curve decreases, and the curve shifts to the upper right (Fig. 3.4). At a fixed N_D value, a larger dimensionless loading time t^* results in a larger loading fraction.

Furthermore, t^* can be considered as the ratio of the loading time t_L and a characteristic intra-particle diffusion time t_D with a weighting factor of a^*.

$$t_D = \frac{R^2}{\varepsilon_p D_p (1-\varepsilon_b)} \tag{3.5a}$$

$$t^* = \frac{t_L}{t_D a^*} = \frac{t_L(1+bC_f)}{t_D a} = \frac{t_L C_f}{t_D q_f} \tag{3.5b}$$

As shown in Eq. (3.4), decreasing the particle size R or the a^* value has a similar effect on t^* as increasing the loading time t_L. A smaller a^* value results from a smaller equilibrium capacity q_f or a higher feed concentration C_f, Eq. (3.5b).

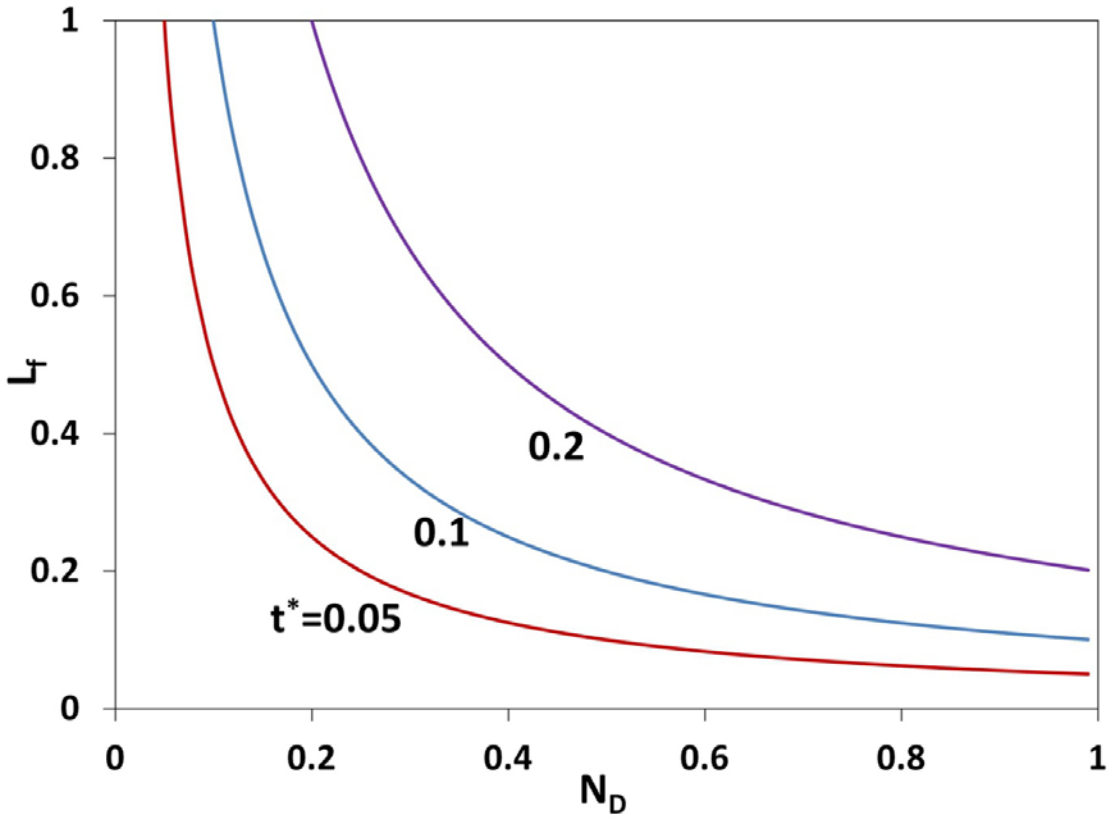

Figure 3.4. Constant loading-time curves (LT curves) for different values of t^*. Along each LT curve, the product $N_D L_f = t^*$ is constant. As t^* decreases, the LT curve shifts towards the origin.

3.2.5 Minimum column volume

The BL curve and the LT curve represent the constraints of the breakthrough limit C_{br}/C_f and the loading time t_L, respectively. The intersection point of the two curves represents the solution that satisfies both constraints (Fig. 3.5). One can calculate from the values of L_f and N_D at the intersection point the minimum column volume. A detailed algorithm is given below.

First, the intrinsic parameters (ε_b, ε_p, D_p, a and b) need to be obtained from a small number of batch equilibrium tests or column tests for a selected sorbent at a given temperature. Second, once these parameters are known, the LT curve can be plotted for the specified values of C_f and t_L. Third, the BL curve for the given bC_f and C_{br}/C_f can be generated by the method described in Section 3.3. The intersection point of the LT curve and the BL curve gives the maximum L_f (L_{fmax}) and the minimum N_D (N_{Dmin}) that satisfy both the breakthrough limit and the loading time requirements (Fig. 3.5). The minimum column volume V_{Cmin} can be determined from L_{fmax} and the feed volume V_f using Eq. (3.3). Any column volume that is smaller than V_{Cmin} will result in a lower yield than the specified yield, since the breakthrough concentration at the given loading time will exceed the breakthrough limit. The value of N_{Dmin} gives the minimum residence time L/u_s that meets the loading time and breakthrough requirements.

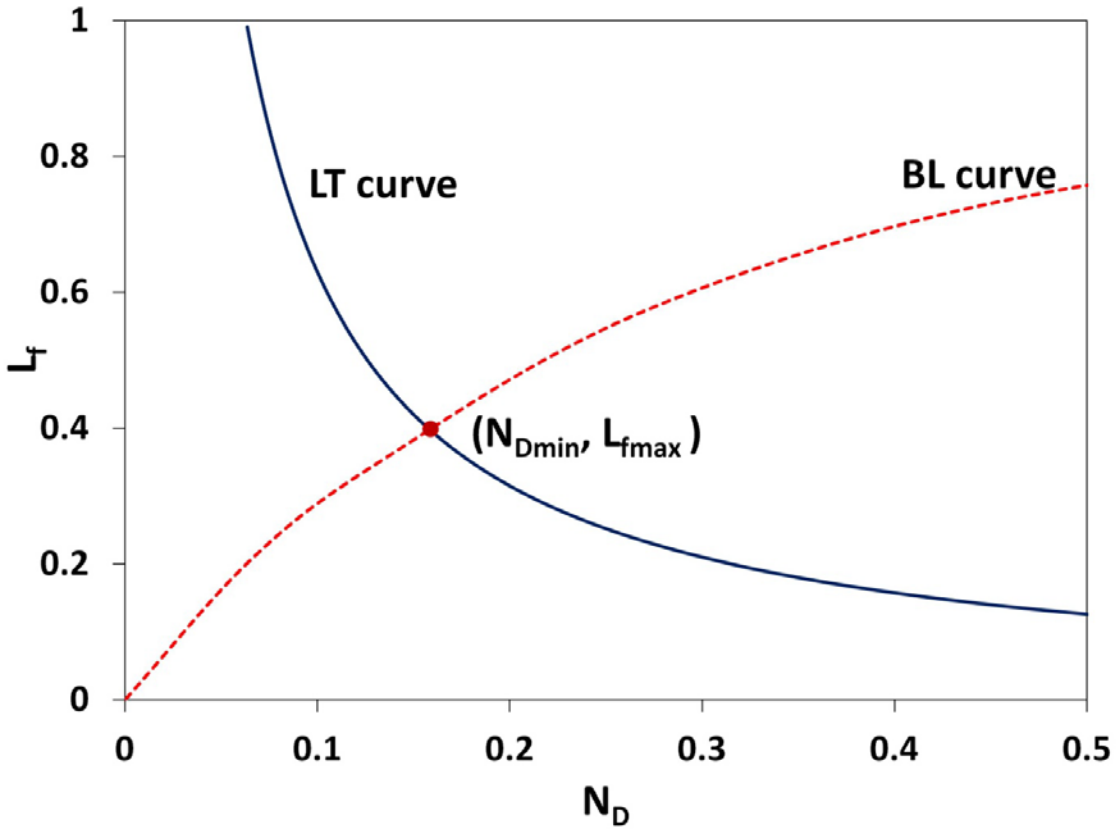

Figure 3.5. Illustration of the minimum-column-volume design method. The intersection point of the LT and the BL curves is the point (N_{Dmin}, L_{fmax}), which satisfies the loading time and the breakthrough limit requirements. The value of L_{fmax} can be used to determine the minimum column volume V_{Cmin} using Eq. (3.3).

3.2.6 Pressure-drop limit

While the intersection point of the LT and BL curves gives the minimum column volume required for capture, it does not specify the column diameter or the column length. Many different combinations of column length and diameter can be used for capture, as long as the residence time L/u_s satisfies the N_{Dmin} requirement. If there is a pressure limit requirement, the maximum column length can be estimated from the pressure-drop limit. For laminar flow in a packed bed, the Reynolds number based on the particle diameter is less than 1, and the pressure drop in the column can be estimated from the simplified Ergun equation.

$$\Delta P = L \times \left[150 \frac{\left(1-\varepsilon_b\right)^2}{\varepsilon_b^{\,3}} \frac{\mu u_s}{4R^2} \right] \tag{3.6}$$

where ΔP is the pressure drop over a column length of L and μ is the viscosity of the mobile phase.

The mechanical strength of sorbent material may pose a limit on the maximum pressure drop per unit column length, or $(\Delta P/L)_{\max}$. In this case, the maximum operating velocity u_{smax} can be obtained directly from Eq. (3.6). Then the maximum column length L_{max} is determined from u_{smax} and N_{Dmin}, which is obtained from the intersection of the LT curve and the BL curve.

If a maximum overall pressure drop ΔP_{max} is specified, the maximum column length L_{max} and the corresponding u_{smax} can be obtained from Eq. (3.6) and the definition of N_D in Table 3.1.

$$L_{\max} = \sqrt{\frac{4R^4 \Delta P_{\max} \varepsilon_b^{\,3} N_{D\min}}{150\left(1-\varepsilon_b\right)^3 \mu \varepsilon_p D_p}} \tag{3.7a}$$

$$u_{s\max} = \frac{(1-\varepsilon_b)\varepsilon_p D_p L_{\max}}{N_{D\min} R^2} \tag{3.7b}$$

The pressure-drop limit does not affect the column volume or the sorbent productivity, but only the dimensions of the column.

3.3 Generalization of the design method to Langmuir isotherm systems

3.3.1 BL curves for constant pattern and non-constant pattern systems

As explained in Section 3.2.5, the fundamental idea of this design method is to plot the breakthrough limit and the loading time constraints as two curves in the same two-dimensional plane, and the minimum column volume that satisfies both constraints can be found from the intersection point. The LT curve can be plotted using the explicit algebraic equation, Eq. (3.4), if the loading time, the feed concentration and the intrinsic parameters (a, b, ε_b, ε_p, R, D_p) are known. The BL curve, however, does not have an obvious correlation. One way to generate a BL curve is to use VERSE simulations. Each point on the curve needs to be generated individually from a simulated frontal wave (Ling et al. 2013). The generated BL curve is specific for the given C_{br}/C_f and bC_f. If the feed concentration is varied, a new curve has to be generated by running additional simulations. This process can be time-consuming, so that it is highly desirable to develop general correlations for the BL curves for Langmuir isotherm systems.

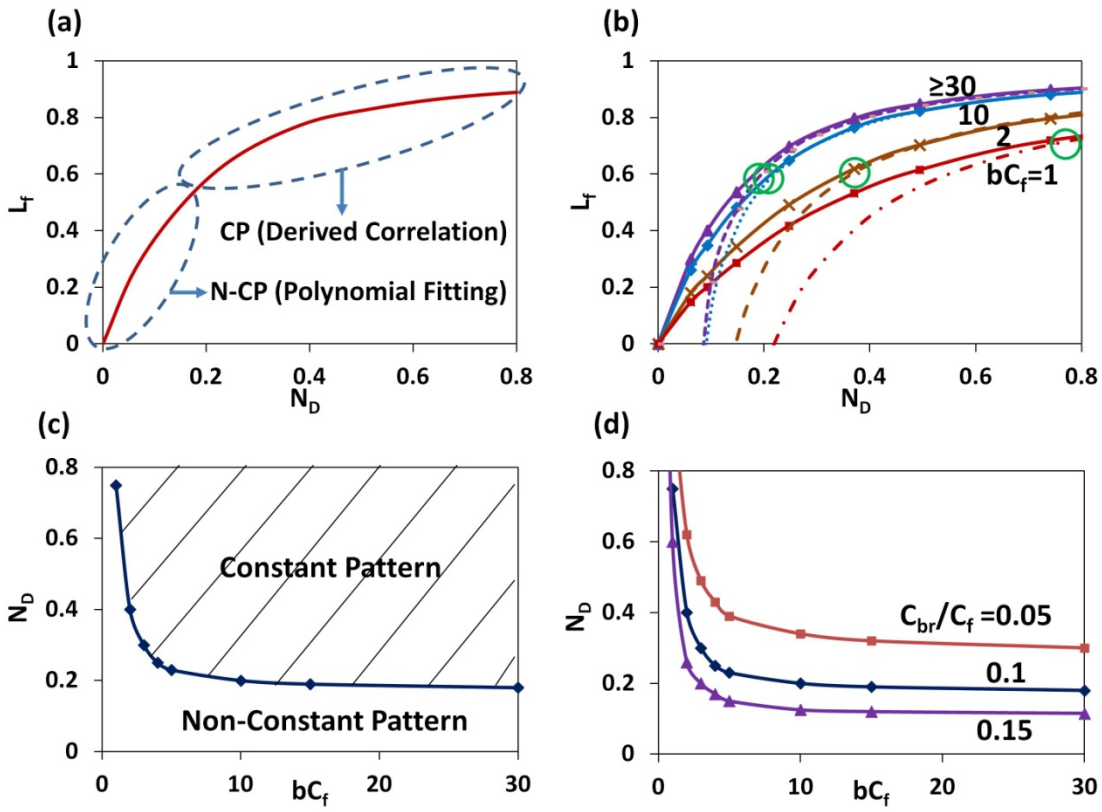

Figure 3.6. (a) Illustration of the method for generating a BL curve. For constant pattern (CP) systems, the BL curves can be generated by using Eq. (3.8); for non-constant pattern (N-CP) systems, the BL curves can be generated by using simulations and then fitted by polynomials. (b) BL curves for C_{br}/C_f=0.1 at different bC_f values. The solid lines were generated based on numerical simulations; the dashed lines were generated using analytical correlations for CP systems. The circles highlight the merging points of the numerical and the analytical solutions. (c) N_D values at the merging points in (b) as a function of bC_f values for C_{br}/C_f=0.1. The shaded region above the curve shows the N_D values required to reach CP when C_{br}/C_f =0.1. (d) The minimum N_D values required to reach CP for C_{br}/C_f=0.05, 0.1 and 0.15.

If the feed concentration is in the nonlinear isotherm region ($bC_f \geq 1$), thermodynamic focusing can counterbalance the wave spreading due to mass transfer effects. If the column length and the loading volume are sufficiently large, the frontal wave can develop into a constant pattern wave (Cooney and Lightfoot, 1965; Garg and Ruthven, 1975). In this case, an approximate correlation of L_f as a function of N_D and bC_f can be derived from the analytical solutions for constant-pattern waves (see the Appendix B). In many affinity systems, however, the frontal wave does not reach a constant pattern, as a result of a small column length, a short loading time, or a small feed volume. In general, constant pattern waves cannot form in the systems with small L_f and N_D values (Fig. 3.6a). For these non-constant pattern systems, the BL curves have to be generated by experiments or simulations. In this study, simulations were first used to generate the BL curves for non-constant pattern systems, and the curves were then fitted by using polynomial equations (see next section).

3.3.2 Conditions for the formation of constant pattern waves

Since the BL curves for constant pattern and non-constant pattern systems are generated separately, it is important to identify the conditions under which a constant pattern wave is formed. It is also of fundamental importance to predict from the intrinsic parameters whether the column length or the velocity at a given feed concentration (C_f) is sufficient to form a constant pattern wave. The BL curves for C_{br}/C_f=0.1 obtained from the analytical solutions for constant pattern systems were compared with those generated from simulations in Fig. 3.6b. For each BL curve with a specific bC_f, a merging point is observed at a sufficiently large N_D value. This point indicates the N_D value that is needed

to form a constant pattern wave for the specific bC_f when C_{br}/C_f=0.1. By connecting the merging points in Fig. 3.6b, one can obtain a curve that divides the constant pattern-region and the non-constant pattern region.

Fig. 3.6c shows how the N_D value at the merging point for C_{br}/C_f=0.1 increases as bC_f decreases. The self-sharpening effect becomes weaker for a smaller bC_f value, and a constant pattern wave can only form at a larger N_D. As bC_f approaches zero (for a linear isotherm system), a constant pattern wave cannot form, resulting in a vertical asymptote in Fig. 3.6c. In the shaded region of this figure, constant pattern waves can form before the breakthrough concentrations reach 10% of the feed concentrations. Below this curve, the N_D values are too small to form constant pattern waves.

The curve dividing the constant pattern and non-constant pattern regions also depends on the values of the breakthrough limit (Fig. 3.6d). As the breakthrough limit becomes smaller, this curve shifts upward, indicating that a larger N_D (a longer column or a smaller velocity) is needed to reach constant pattern before the smaller breakthrough concentration reaches the column outlet.

3.3.3 General correlations of the BL curves

If intra-particle diffusion dominates wave spreading, the correlations for the constant pattern BL curves are derived from the well-known solutions for constant pattern waves for Langmuir isotherm systems (Garg and Ruthven, 1975) and the relation between the overall mass transfer coefficient and the intra-particle diffusivity (Ruthven, 1984). The assumptions and derivations are explained in detail in the Appendix B. The general form obtained is

$$L_f = 1 - \frac{1}{2}\left[(-1 + 2\frac{1+bC_f}{bC_f})\ln(\frac{1-C_{br}/C_f}{C_{br}/C_f})\right]\frac{1}{15N_D} \qquad (3.8)$$

For non-constant pattern waves, Eq. (3.8) does not apply. The BL curves for a specific breakthrough limit were generated from numerical simulations for various values of N_D and bC_f. The curves were then fitted with third order polynomial functions of N_D. The three coefficients of the polynomials were then correlated as functions of bC_f (Table 3.2). When bC_f=0, the polynomial curves approach the numerical BL curves for linear isotherm systems. The correlations for both constant pattern and non-constant pattern BL curves developed for the breakthrough limits of 0.05, 0.10, and 0.15 in the range of N_D from 0 to 0.8 are listed in Table 3.2.

The correlations for the BL curves with different bC_f and C_{br}/C_f values agree closely with the numerical BL curves (Fig. 3.7a-c). The results indicate that the correlations can replace the numerical simulations for generating the BL curves, allowing the design of a capture column to be more efficient.

Table 3.2 Correlations for BL curves with Langmuir isotherms

C_{br}/C_f	Constant Pattern	Non-Constant Pattern*
0.05	$L_f = 1-(-1.47+2.94\frac{1+bC_f}{bC_f})\frac{1}{15N_D}$	$L_f = (0.56+\frac{0.51bC_f}{1+0.07bC_f})N_D{}^3-(1.16+\frac{1.03bC_f}{1+0.11bC_f})N_D{}^2+(1.13+\frac{0.84bC_f}{1+0.21bC_f})N_D$
0.1	$L_f = 1-(-1.1+2.2\frac{1+bC_f}{bC_f})\frac{1}{15N_D}$	$L_f = (1.06+\frac{0.77bC_f}{1+0.11bC_f})N_D{}^3-(1.98+\frac{1.44bC_f}{1+0.15bC_f})N_D{}^2+(1.57+\frac{1.03bC_f}{1+0.27bC_f})N_D$
0.15	$L_f = 1-(-0.867+1.734\frac{1+bC_f}{bC_f})\frac{1}{15N_D}$	$L_f = (1.61+\frac{1.07bC_f}{1+0.16bC_f})N_D{}^3-(2.86+\frac{1.89bC_f}{1+0.20bC_f})N_D{}^2+(2+\frac{1.24bC_f}{1+0.35bC_f})N_D$

* Range for the polynomial correlation: $0 \le bC_f \le 30$, $0 \le N_D \le 0.8$

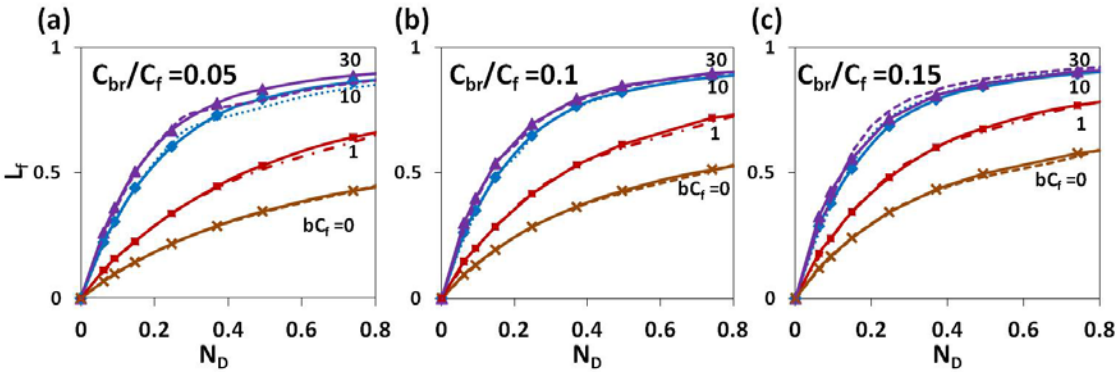

Figure 3.7. BL curves generated for C_{br}/C_f=0.05 (a), 0.1 (b), and 0.15 (c) at different bC_f values. The solid lines with symbols were generated from numerical simulations, and the dashed lines were generated using the correlations listed in Table 3.2.

3.3.4 Testing of the new design method based on the correlations of the BL curves

Fourteen published breakthrough curves for Protein A affinity chromatography were used to test the accuracy of the new design method based on the correlations. Table 3.3 and 3.4 summarize the material properties, column sizes, feed concentrations, and dimensionless groups for the literature cases (Ng et al. 2012; Novasep product data profile; Miyahara et al. 2012; Katoh et al. 2007; Perez-Almodovar and Carta 2009). In some of the references, the isotherm parameters (Ng et al. 2012; Perez-Almodovar and Carta 2009) and the intra-particle diffusivities (Perez-Almodovar and Carta 2009) were reported. If the values were not reported, the two isotherm parameters were estimated from the reported maximum equilibrium capacity and the mass center of the frontal curves. The diffusivities were estimated by fitting the reported experimental breakthrough curves with simulated breakthrough curves with different diffusivity values.

In testing the new method, the breakthrough time t_{br} for C_{br}/C_f =0.1 was first identified from a reported frontal curve, and then the corresponding loading volume V_{br} was calculated from the loading time and the flow rate. The correlation of the BL curve was used in the design method to find the minimum column volume for C_{br}/C_f=0.1 from the feed volume V_{br} and the loading time t_{br}. In this case, the minimum column volume was expected to be the same as the experimental column volume. Two examples from Ng et al. 2012 are shown in Fig. 3.8a-b. In both cases, the differences between the theoretical column volume and the experimental column volume are less than 7%.

Table 3.3 Material properties and column dimensions for the data of Protein A chromatography

Sorbent	Ref	R (μm)	ε_b	ε_p	$D_p \times 10^6$ (cm^2/min)	a	b (L/g)	L (cm)	ID (cm)
AbSolute	Ng et al.[a]	22	0.35	0.69	5.0	224	3.2	5	0.5
AbSolute	Novasep[a]	22	0.35	0.69	8.0	102	1.5	5	0.5
A-D-50-1000AW	Miyahara et al.[a]	25	0.35	0.78	8.0	246	3.5	10	0.46
Alkali-treated M.S.GEL D-50-60A	Katoh et al.[a]	22	0.35	0.78	10.0	80.7	1.15	2.5	0.5
UNOsphere SUPrA	Perez-Almodovar et al.[b]	28.5	0.35	0.62	5.6	2736	72	2	0.5

[a]The intrinsic parameters (ε_b, ε_p, D_p, a and b) are estimated from the information provided by the references.

[b]The intrinsic parameters (ε_b, ε_p, D_p, a and b) are provided by the reference.

Table 3.4 Loading conditions and dimensionless groups for the Protein A chromatography data

Sorbent	Ref	C_f (g/L)	u_s (cm/min)	t_L for C_{br}/C_f=0.1 (min)	N_D	t^*	$V_{Cmin}{}^*$
AbSolute	Ng et al.	0.9	5.0	40.9	0.465	0.329	1.41
			25.0	2.6	0.093	0.021	4.46
AbSolute	Novasep	1.5	10.0	10	0.372	0.233	1.60
A-D-50-1000AW	Miyahara et al.	0.5	5.0	154	1.298	1.120	1.16
			8.3	85	0.782	0.619	1.25
Alkali-treated M.S.GEL D-50-60A	Katoh et al.	0.4	2.3	42.6	1.139	0.807	1.39
			5.0	16	0.524	0.303	1.73
UNOsphere SUPrA	Perez-Almodovar et al.	2.1	2.6	7.7	0.214	0.119	1.83
			5.1	3.3	0.109	0.051	2.16
			10.2	1.2	0.055	0.019	2.90
			12.8	0.70	0.044	0.011	4.02
			15.3	0.48	0.036	0.007	4.90
			17.9	0.36	0.031	0.006	5.63
			20.4	0.25	0.027	0.004	6.99

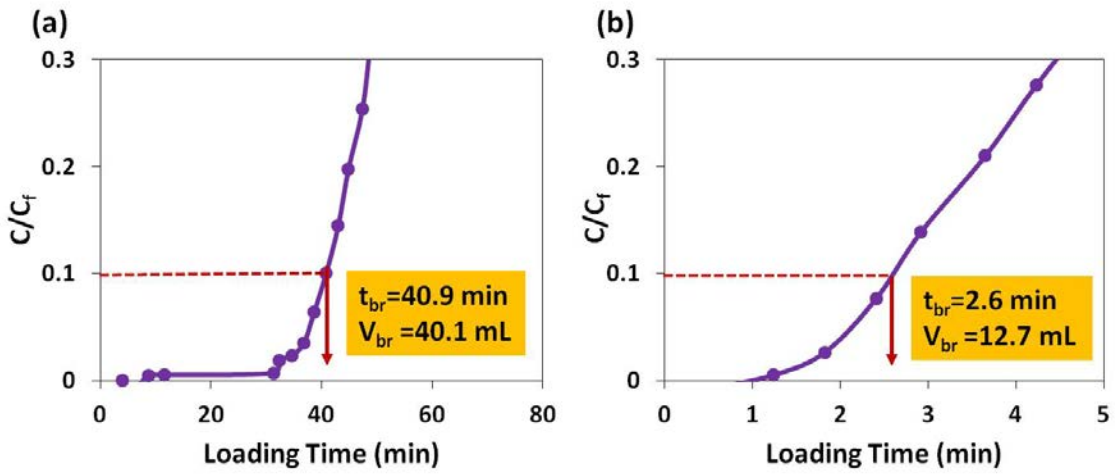

Predicted V_{Cmin} (mL)	Experimental V_C (mL)
0.965	0.982

Predicted V_{Cmin} (mL)	Experimental V_C (mL)
0.917	0.982

Figure 3.8. Breakthrough curves for IgG in Protein A chromatography. The experimental data points (•) were obtained from Ng et al. (2012) and they were connected by solid lines. The breakthrough time t_{br} and the breakthrough volume V_{br} for C_{br}/C_f=0.1 were identified from the chromatograms. The column dimension and feed concentration are shown in Tables 3.3 and 3.4. The superficial velocities were 5 cm/min (a) and 25 cm/min (b). The predicted V_{Cmin} values were obtained from the graphical method using the t_{br} and V_{br} in the figures along with the material properties and feed concentration given in Table 3.4.

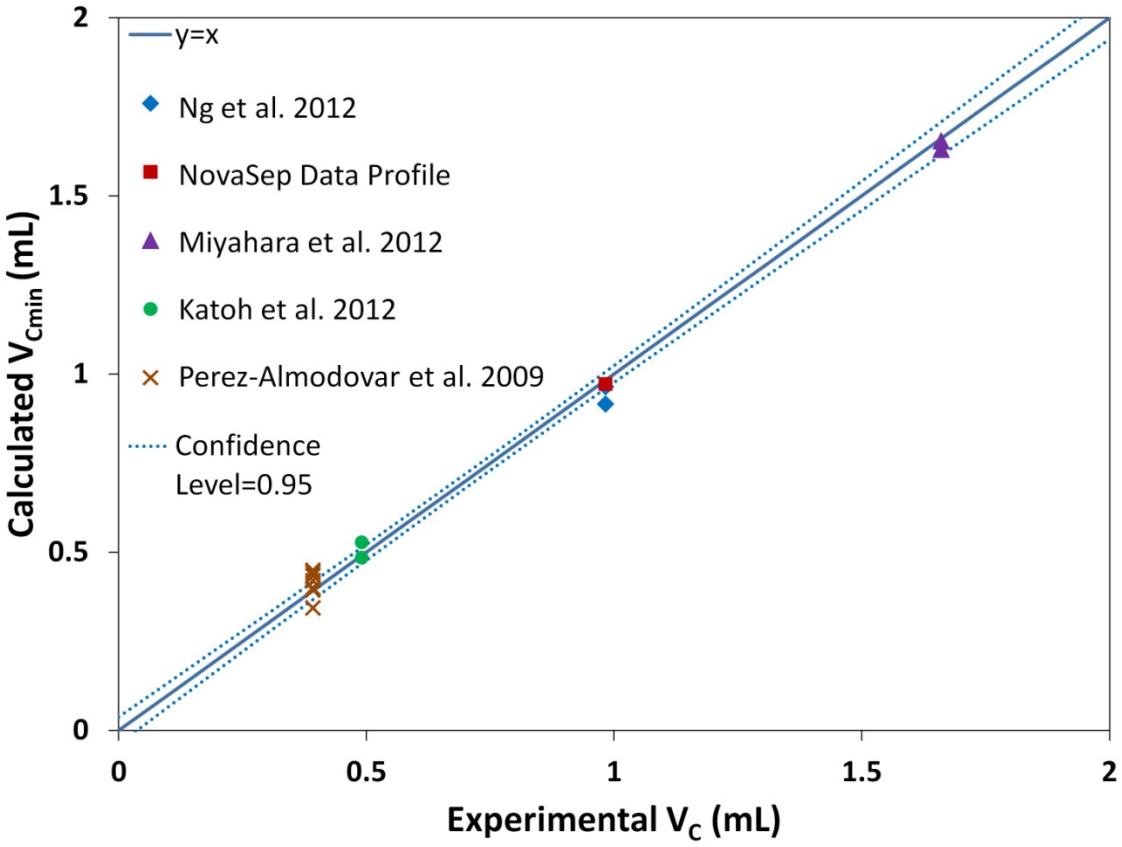

Figure 3.9. Comparison of the calculated minimum column volumes and the experimental column volumes reported in the references. The confidence interval of 0.95 was generated using the method described in Montgomery et al. (2012).

Fig. 3.9 shows a comparison of 14 calculated minimum column volumes to the experimental column volumes reported in the literature. The data points are close to the y=x line with a standard deviation of 0.039. The curves corresponding to the 95% confidence interval were obtained using the standard method (Montgomery et al. 2012). The curves are close to the y=x line, indicating close agreement between the theoretical and the experimental column volumes. The results indicate that the design method based on the correlations is accurate for finding the minimum column volumes.

3.3.5 Trade-off between column volume and loading time

The previous sections are focused on finding the minimum column volume (V_{Cmin}) if the loading time and the breakthrough limit (or yield) are fixed. The V_{Cmin} value corresponds to the maximum sorbent productivity for the fixed loading time and yield. In certain applications, the loading time is not fixed and needs to be optimized for the lowest cost or the largest amount of active product. In general, a short loading time leads to a high sorbent productivity, but results in a large column volume for capture.

The LT curves for different dimensionless loading times t^* are plotted in Fig. 3.10, where the intersection points with the BL curves for C_{br}/C_f =0.1 are shown. The BL curves are plotted by using the correlations in Table 3.2. When the bC_f values are less than 1, the N_D values required to reach constant pattern are greater than 0.8, which is beyond the accuracy of the polynomial correlations. For these cases, the BL curves for N_D >0.8 in Fig. 3.10 were obtained from simulations.

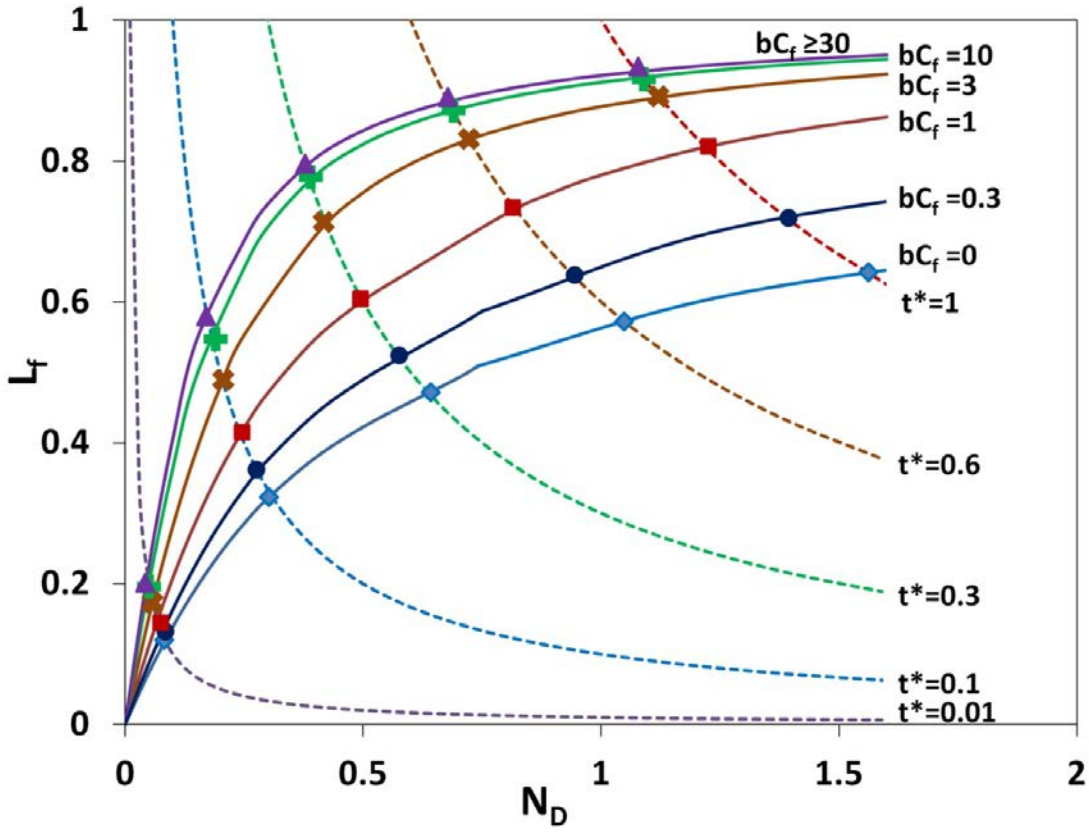

Figure 3.10. LT curves (dashed lines) with various t^* values and BL curves (solid lines) with various bC_f values. For bC_f=0 and bC_f=0.3, the BL curves for N_D>0.8 were generated based on numerical simulations. The intersection points of BL curves and LT curves correspond to different minimum column volumes for capture.

As shown in Fig. 3.10, when the loading time t^* in Eq. (3.4) decreases from 1 to 0.01, the loading fraction L_f at the intersection points decreases from 0.64 to 0.12 for linear systems (bC_f =0), and from 0.93 to 0.21 for highly nonlinear systems ($bC_f \geq 30$). All the other BL curves for nonlinear systems ($0<bC_f<30$) fall between these two BL curves and the intersection points with the LT curves show similar relations between t^* and L_f. The results suggest that a larger column volume is required for a shorter loading time to meet the same breakthrough or yield requirement.

The intersection points in Fig. 3.10 give the minimum column volumes that satisfy the required loading times and the breakthrough limit of 0.1. To show explicitly the relation between the minimum column volume and the loading time, we define a dimensionless minimum column volume V_{Cmin}^* as below.

$$V_{C\min}^* = \frac{1}{L_{f\max}} = \frac{a^* V_{C\min}}{V_f} = \frac{aV_{C\min}}{(1+bC_f)V_f} \tag{3.9}$$

The dimensionless minimum column volume V_{Cmin}^* obtained from the intersection points of Fig. 3.10 are plotted as a function of the dimensionless loading time t^* for C_{br}/C_f=0.1 in Fig. 3.11a. The differences between the curves for linear systems bC_f =0 and for nonlinear systems bC_f >0 are due to the thermodynamic sharpening effects. As bC_f increases, the frontal wave becomes sharper, resulting in a smaller V_{Cmin}^* for a given t^*. When bC_f increases to above 30, the BL curves do not change (Fig. 3.6b). As a result, the V_{Cmin}^* vs. t^* curves for bC_f >30 also remain the same as that for bC_f =30. All the possible solutions of V_{Cmin}^* vs. t^* for Langmuir systems for C_{br}/C_f=0.1 fall between the curve for linear systems (bC_f =0) and the curve for highly non-linear systems ($bC_f \geq 30$).

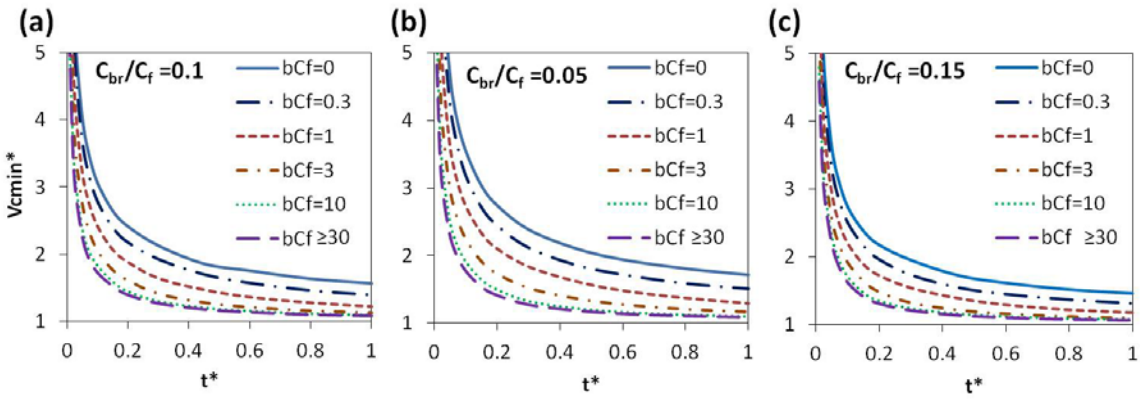

Figure 3.11. Relations between dimensionless minimum column volume V_{Cmin}^{*} and dimensionless loading time t^{*} for C_{br}/C_f=0.1 (a), 0.05 (b), and 0.15 (c).

Along one curve, as t^* decreases to below 0.1, the dimensionless minimum column volume V_{Cmin}^* increases sharply, because of a sharp decrease of the loading fraction in this region. In contrast, for $t^* \geq 0.5$, V_{Cmin}^* decreases slowly to a limit, and further increase in t^* only results in a marginal increase in loading fraction. For a $C_{br}/C_f = 0.1$ and $t^* = 1.0$, the limiting V_{Cmin}^* is about 1.6 for linear systems ($bC_f = 0$) and about 1.1 for highly nonlinear systems ($bC_f \geq 30$).

As the breakthrough limit decreases from 0.1 to 0.05, the curve for linear isotherm systems ($bC_f = 0$) shifts slightly upward (Fig. 3.11b), because the minimum column volume for capture is larger for a higher capture yield. In contrast, as the breakthrough limit increases from 0.1 to 0.15, the curve for linear isotherm systems ($bC_f = 0$) shifts slightly downward (Fig. 3.11c). For highly nonlinear systems, $bC_f \geq 30$, the frontal waves are almost vertical. Therefore, L_f or V_{Cmin}^* remains almost the same for different breakthrough limits, and the differences in V_{Cmin}^* vs. t^* curves are negligible.

In Fig. 3.11a-c, all the theoretical solutions of V_{Cmin}^* at a given t^* for nonlinear systems ($bC_f > 0$) fall between the V_{Cmin}^* for linear systems ($bC_f = 0$) and that for highly nonlinear systems ($bC_f \geq 30$). For this reason, all the experimental data for Langmuir systems with various bC_f values should be between the upper bound, the curve for $bC_f = 0$, and the lower bound, the curve for $bC_f \geq 30$. Fourteen pairs of the V_{Cmin}^* and t^* values for $C_{br}/C_f = 0.1$ were calculated from the literature data (Table 3.4) and were compared with the theoretical curves in Fig. 3.12. The literature data indeed are between the two curves.

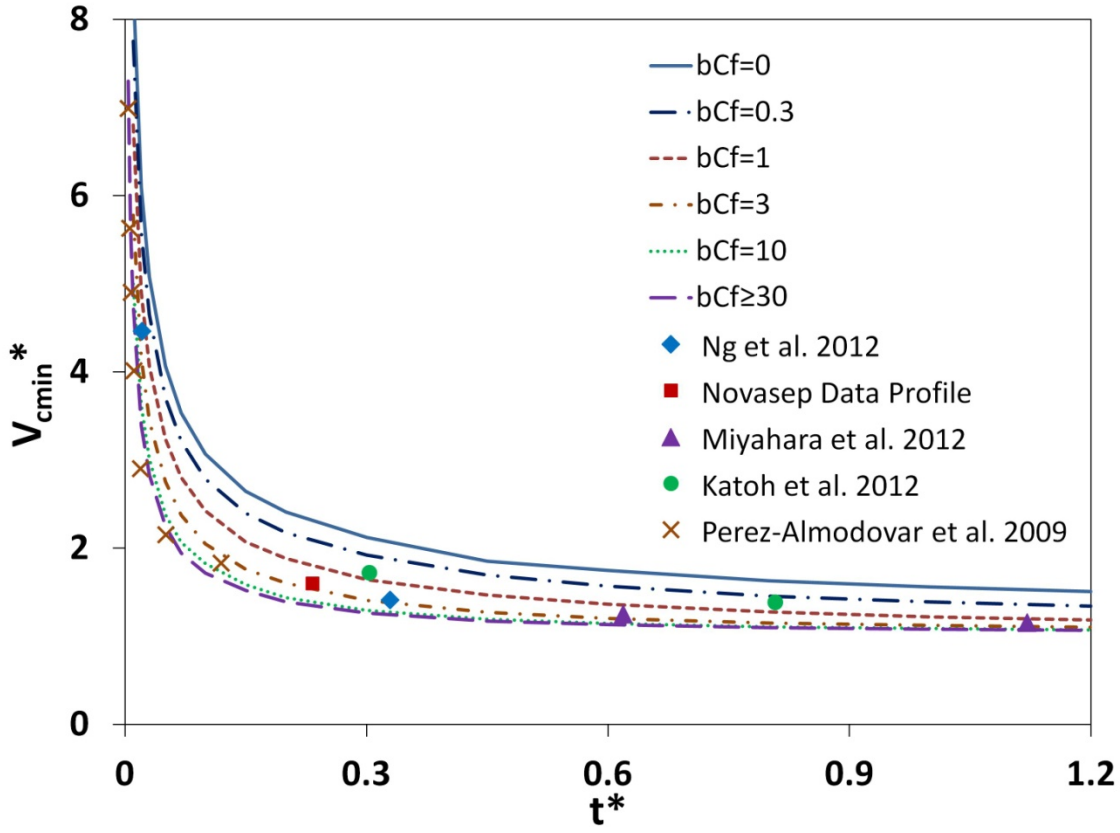

Figure 3.12. Comparison of literature data points (t^*, $V_{Cmin}{}^*$) and theoretical relations between $V_{Cmin}{}^*$ and t^*.

3.4 Effects of material properties, loading time, and feed conditions on minimum column volume and maximum productivity

3.4.1 Ideal systems

For an ideal system without mass transfer resistances, the frontal wave is vertical, or a step function, and $V_{Cmin}^{*}=1/L_{fmax}=1$. As a result, Eq. (3.9) can be rearranged as below.

$$V_{C\min,ideal}=\frac{V_f}{a^*}=\frac{V_f(1+bC_f)}{a} \tag{3.10}$$

Eq. (3.10) shows that column volume is only affected by feed volume, feed concentration and adsorption isotherms. A small V_f or a large a^* value leads to a small column volume.

For a given loading time, the minimum column volume gives the maximum productivity, which is defined as the ratio of dynamic loading amount to the product of the minimum column volume and loading time.

$$Pr_{\max}=\frac{C_fV_f}{t_LV_{C\min}} \tag{3.11}$$

The maximum productivity of an ideal system can be derived from Eqs.(3.10) and (3.11).

$$Pr_{\max,ideal}=\frac{a^*C_f}{t_L}=\frac{q_f}{t_L} \tag{3.12}$$

Eq. (3.12) indicates that a high feed concentration C_f, a large a^* value, or a short loading time t_L results in a high productivity. When $bC_f>>1$, a^* approaches a/bC_f, and $Pr_{max,ideal}$ approaches a/bt_L, or q_{max}/t_L.

3.4.2 Non-ideal, constant pattern systems

For a non-ideal system, both V_{Cmin} and Pr_{max} are affected by loading time and mass transfer effects. For constant pattern systems (Fig. 3.6c-d), an explicit solution for the intersection point of the BL curve and the LT curve (L_{fmax}, N_{Dmin}) can be obtained from Eqs. (3.4) and (3.8). Since V_{Cmin}^{*} equals $1/L_{fmax}$, Eq. (3.9) can be used to express V_{Cmin} as a function of a^{*}, V_f, t^{*}, bC_f, and C_{br}/C_f. The final form is shown below.

$$V_{C\min} = V_f \left[\frac{1}{a^{*}} + \frac{1}{2} \frac{\ln\left(\frac{1-C_{br}/C_f}{C_{br}/C_f}\right)\left(-1+2\frac{1+bC_f}{bC_f}\right)}{15 a^{*} t^{*}} \right] = V_f \left[\frac{1+bC_f}{a} + \frac{1}{2} \frac{t_D \ln\left(\frac{1-C_{br}/C_f}{C_{br}/C_f}\right)\left(-1+2\frac{1+bC_f}{bC_f}\right)}{15 t_L} \right] \qquad (3.13)$$

The first term in Eq. (3.13) arises from ideal adsorption. The second term is due to non-ideal mass transfer effects. A long diffusion time t_D or a short loading time t_L results in a large column volume. The term $(1+bC_f)/bC_f$ is related to thermodynamic sharpening effects. A small bC_f value results in a large V_{Cmin}. If bC_f is much larger than 1, thermodynamic sharpening reduces this term to unity. In addition, a high yield or a small C_{br}/C_f also results in a large V_{Cmin}.

The maximum productivity corresponding to the V_{Cmin} for non-ideal systems can be derived by combining Eq. (3.11) and Eq. (3.13).

$$Pr_{\max} = \frac{C_f}{\left[\frac{t_L}{a^{*}} + \frac{1}{2} \frac{t_D \ln\left(\frac{1-C_{br}/C_f}{C_{br}/C_f}\right)\left(-1+2\frac{1+bC_f}{bC_f}\right)}{15} \right]} = \frac{1}{\left[\frac{t_L}{q_f} + \frac{1}{2} \frac{t_D \ln\left(\frac{1-C_{br}/C_f}{C_{br}/C_f}\right)\left(-1+2\frac{1+bC_f}{bC_f}\right)}{15 C_f} \right]} \qquad (3.14)$$

In general, the minimum column volume V_{Cmin} for a non-ideal system is larger, while the maximum productivity is lower, than those for the corresponding ideal system.

3.4.3 Non-ideal, non-constant pattern systems

If the N_{Dmin} value obtained from Eqs. (3.4) and (3.8) are below the boundary curve for constant pattern in Fig. 3.6c, the frontal wave does not reach a constant pattern when C_{br}/C_f=0.1. The equations in Section 3.4.2 do not apply. The V_{Cmin} can be estimated from Fig. 3.11a-c, or by solving the LT equation, Eq. (4), in conjunction with the correlation equations of the BL curves in Table 3.2. The resulting V_{Cmin} does not have simple analytical expressions, but the effects of the different variables on V_{Cmin} and Pr_{max} are similar as those for constant pattern systems, Eqs. (3.13) and (3.14).

3.4.4 Effects of material properties and loading conditions on minimum column volume and productivity

For ideal systems, diffusion time and yield have no effect on V_{Cmin} or Pr_{max}. For non-ideal systems, a higher yield requires a larger column volume and results in a lower sorbent productivity. The effects of material properties, loading time, feed concentration, and feed volume on V_{Cmin} and Pr_{max} are similar for both constant pattern and non-constant pattern systems. A summary of the various effects is shown in Table 3.5.

A small particle size, a small bed void fraction, or a large diffusivity results in a short diffusion time and a sharp wave front, leading to a small V_{Cmin} and a large Pr_{max}, as expected from Eq. (3.13) and Eq. (3.14), respectively. A large a value or a small b value gives a large a^* value, which also results in a small V_{Cmin} and a large Pr_{max}.

Table 3.5 Effects of material properties and loading conditions on the minimum column volume and the maximum productivity

Variation of parameters	Effect on V_{Cmin}	Effect on Pr_{max}
Yield ↑ (C_{br}/C_f ↓)	V_{Cmin} ↑	Pr_{max} ↓
t_D ↓ (R ↓, ε_b ↓,D_p ↑,ε_p ↑)	V_{Cmin} ↓	Pr_{max} ↑
a ↑	V_{Cmin} ↓	Pr_{max} ↑
b ↓	V_{Cmin} ↓	Pr_{max} ↑
t_L ↑	V_{Cmin} ↓	Pr_{max} ↓
C_f ↑ (V_f fixed)	V_{Cmin} ↑	Pr_{max} ↑
C_f ↑ (C_fV_f fixed)	V_{Cmin} ↓	Pr_{max} ↑
V_f ↑	V_{Cmin} ↑	None

An increase in loading time can sharpen the wave front and reduce the V_{Cmin}, Eq. (3.13). However, the Pr_{max} also decreases with increasing loading time, Eq. (3.14). A short loading time can achieve a high productivity, and a short diffusion time can keep the column volume small. The results indicate that to achieve both small column volume and high productivity, one should use a short loading time and a sorbent with a small particle size or a high diffusivity.

As feed concentration increases, the feed amount becomes larger and the a^* value becomes smaller, resulting in a larger V_{Cmin}, Eq. (3.13). If the total amount of the target solute, or C_fV_f, is fixed, the feed volume decreases as the feed concentration increases. Then the V_{Cmin} is reduced when the feed is concentrated, Eq. (3.13). The Pr_{max} always increases with increasing feed concentration, Eq. (3.14). The results indicate that if the amount of solute to be captured is fixed, a concentrated feed can reduce the column volume and increase the productivity.

If the capture process is scaled up by increasing the feed volume, the V_{Cmin} will increase proportionally, Eq. (3.13), but the productivity will remain the same, Eq. (3.14).

3.4.5 Graphical analysis

The effects of varying material properties or loading conditions on V_{Cmin}^* can be visualized graphically from the plot of V_{Cmin}^* vs. t^*. We consider a typical sorbent, which has similar intrinsic properties as the commercial sorbent AbSolute (Novasep, Boothwyn, PA): a=200, b=3 Lg^{-1}, and R=25 μm. The other intrinsic parameters are the same as those of Ng et al. 2012 in Table 3.3. The feed concentration C_f is 1 g L^{-1}, and the loading time

is 30 min. The effects of loading time, particle size, the Langmuir *a* and *b*, and the feed concentration are shown in Fig. 3.13a-d.

For bC_f=3, as the loading time t_L increases from 30 to 60 or 120 min, the t^* value, which equals t_L/a^*t_D, increases from 0.215 to 0.43, or 0.86, respectively, while $V_{Cmin}{}^*$ decreases from 1.58 to 1.29 and 1.14 (Fig. 3.13a). The V_{Cmin}, which equals $V_fV_{Cmin}{}^*(1+bC_f)/a$, Eq. (3.9), also decreases accordingly. When the t_L is greater than 60 min (t^*=0.43), further increase in t_L does not reduce significantly the column volume.

For a highly nonlinear system, bC_f=30, the value of t^*, which is proportional to $(1+bC_f)$, is much larger than that for bC_f =3 at the same t_L (Fig. 3.13a), resulting in a smaller $V_{Cmin}{}^*$. When t_L=15 min, t^*=0.84, and $V_{Cmin}{}^*$=1.1. This indicates that a small loading time can still achieve a high loading fraction if the thermodynamic sharpening effect is strong. By contrast, for a linear system, bC_f=0, t^* is much smaller at the same t_L. In the absence of the thermodynamic sharpening effects, the small t^* results in a large $V_{Cmin}{}^*$. For a given t_L, the actual column volume V_{Cmin} for bC_f =3 is still smaller than that for bC_f=30 if V_f is fixed, because V_{Cmin} is proportional to $V_{Cmin}{}^*(1+bC_f)$, Eq. (3.9).

The effects of varying particle radius *R* on V_{Cmin} are shown in Fig. 3.13b. As *R* decreases, the diffusion time decreases with R^2, Eq. (3.5a), resulting in a larger $t^*$and a smaller $V_{Cmin}{}^*$. For bC_f=3, as *R* decreases from 50 μm to 25 μm, t^* increases from 0.054 to 0.215, and $V_{Cmin}{}^*$ decreases from 2.68 to 1.58. Thus, the actual column volume V_{Cmin} also decreases. If *R* is further reduced from 25 μm to 15 μm, the $V_{Cmin}{}^*$ only decreases from 1.58 to 1.21, indicating that further decrease in the particle size will be ineffective in reducing the column volume or increasing the productivity. As $V_{Cmin}{}^*$ approaches 1, V_{Cmin}/V_f approaches $1/a^*$=0.02, which is the limiting value for an ideal system, Eq. (3.10).

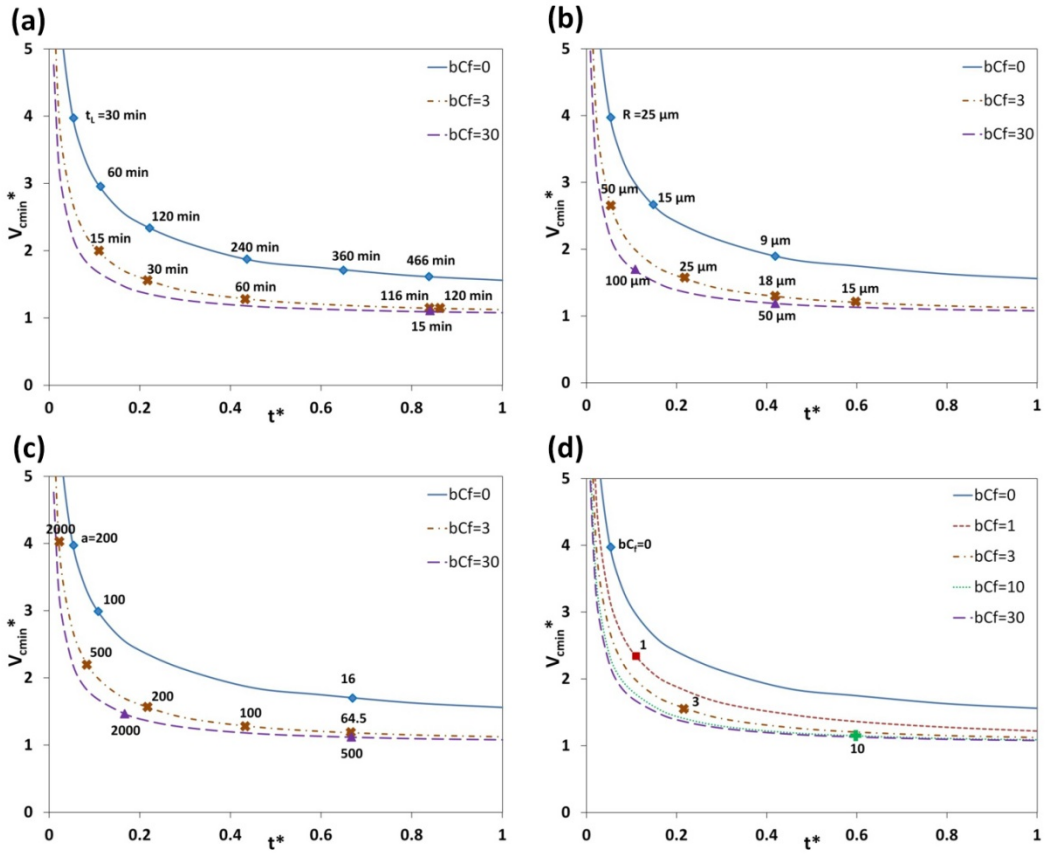

Figure 3.13. Effect of loading time (a), particle size (b), Langmuir *a* value (c), and feed concentration (d) on minimum column volume. The parameters used in the benchmark case are: a=200, t_L=30 min, R=25 µm, ε_b=0.35, ε_p=0.69, D_p=5×10^{-6} cm^2 min^{-1}, C_{br}/C_f=0.1.

For R=50 μm, when bC_f increases from 3 to 30, t^* increases from 0.054 to 0.419. The results suggest that highly nonlinear systems with large particles can achieve the same loading fraction as less nonlinear systems with smaller particles. For a given R, the actual column volume V_{Cmin} for bC_f =3 is still smaller than that for bC_f=30 if V_f is fixed.

The effects of a are shown in Fig. 3.13c. For bC_f =3, as a increases by 10 fold, from 200 to 2,000, t^* decreases from 0.2 to 0.02, and $V_{Cmin}{}^*$ increases 2.6 times, from 1.58 to 4.06. Although $V_{Cmin}{}^*$ increases with increasing a, the actual column volume V_{Cmin}, which is proportional to ($V_{Cmin}{}^*/a$), decreases 4 times, because of the larger a value. The results indicate that a 10-fold increase in the equilibrium capacity q_f does not lead to a 10-fold decrease in column volume required for capture, because of poor capacity utilization at the small dimensionless loading time, t^*=0.02.

For a highly nonlinear system, bC_f =30, the t^* values for the various a values are larger than those for bC_f =3, and the $V_{Cmin}{}^*$ values become smaller. The results indicate that highly nonlinear systems require large a values to reach the same loading fraction as less nonlinear systems. For a given a value, the actual column volume for bC_f =3 is still smaller than that for bC_f=30 if V_f is fixed.

The effects of bC_f are shown in Fig. 3.13d. If the feed volume is fixed, increasing b has a similar effect as increasing C_f. As bC_f increases from 0 to 1, 3, or 10, t^* increases from 0.054 to 0.108, 0.215, or 0.592, respectively, and $V_{Cmin}{}^*$ decreases from 3.96 to 2.37, 1.58, or 1.15. Further increases in bC_f will only have marginal gains in the loading fraction. Since V_{Cmin} is proportional to $V_{Cmin}{}^*(1+bC_f)$, the actual column volume still increases with increasing bC_f.

If the total amount of solute is fixed, an increase in C_f leads to a decrease in V_f. For example, if C_f increases 10 fold, from 0.33 g/L to 3.3 g/L, V_f reduces by 10 fold, and the bC_f value increases from 1 to 10. The V_{Cmin}^* decreases from 2.37 to 1.15, Fig. 3.13d. The actual volume V_{Cmin}, which equals $V_f V_{Cmin}^*(1+bC_f)/a$, decreases by about 73%.

In summary, to reduce the minimum column volume for capture and to maximize sorbent productivity, the sorbent should have a large a value and a small b value to provide a large equilibrium capacity**.** The diffusion time should be small compared to the loading time to yield a large dimensionless loading time t^*. A small diffusion time can be achieved with small particles, small bed void fractions, and large diffusivities. When t^* is larger than 0.5, further increases in t^* has only marginal gains in the loading fraction. If the amount of solute to be recovered is fixed, a more concentrated feed requires a smaller column volume for capture, and leads to a larger sorbent productivity. Decreasing loading time always increases both minimum column volume and maximum sorbent productivity.

3.5 General design and scale up of a capture process

The general graphical solutions shown in Fig. 3.11a-c are valid for Langmuir systems with all production scales. If the yield, the feed concentration, the feed volume, and the loading time are specified and the material properties are known, one can calculate t^* and find V_{Cmin}^* from one of the figures that satisfies the yield requirement. V_{Cmin} can be calculated from V_{Cmin}^* using Eq. (3.9).

If a maximum pressure drop is specified, the maximum column length L_{max} and the corresponding maximum velocity u_{smax} can be calculated from Eq. (3.7). The value of N_{Dmin} can be calculated from t^* and V_{Cmin}^* since $N_{Dmin}=t^* V_{Cmin}^*$. The minimum column

diameter can be calculated from the minimum column volume V_{Cmin} and the maximum column length L_{max}. Any column length smaller than L_{max} can meet the design requirements if the velocity u_s meets the residence time requirement, $L/u_s = L_{max}/u_{smax}$. If the sorbent mechanical strength poses a limit on $(\Delta P/L)_{\max}$, the u_{smax} can be obtained directly from Eq. (3.6). Then the L_{max} can be determined from u_{smax} and N_{Dmin}.

If the column volume needed for capture V_C is fixed and the feed concentration C_f, the feed volume V_f, and the yield are specified, the velocity u_s and the loading time t_L can be estimated using Fig. 3.11a-c. V_{Cmin}^* can be calculated from the given V_C, C_f, V_f, and the a and b values. The value of t^* can be found from the graph that satisfies the yield requirement. Then the loading time can be found from t^*, the diffusion time t_D, and the value of a^*. The velocity u_s can be found from Eq. (3.7b) and N_{Dmin}.

Instead of using the graphs (Fig. 3.11a-c), V_{Cmin} can be found using the correlations for the BL curves shown in Section 3.3.3. The two unknowns, N_{Dmin} and L_{fmax}, can be solved analytically from the LT curve equation, Eq. (3.4), and the BL curve equation that meets the yield requirement, Table 3.2. The t^* value in Eq. (3.4) can be calculated from the given loading time t_L and the material properties. The minimum column volume, the maximum column length and the maximum velocity can be calculated from N_{Dmin} and L_{fmax}.

The intrinsic parameters and dimensionless groups, which are independent of process scales, are used in this method. If the material properties, design requirements, or production scales change, one can rapidly find the new column volume or loading time by using the graphs or by solving the equations for the LT curve and the BL curve.

3.6 Summary and conclusions

A new general method has been developed for designing affinity chromatography processes. For Langmuir isotherm systems, if the material properties and feed conditions are known, the minimum column volume V_{Cmin} for the required yield and loading time can be determined without simulations. The material properties consist of particle size R, porosity ε_p, adsorption isotherm parameters a and b, diffusivity D_p, and bed void fraction ε_b. The particle size and porosity are usually known. The remaining properties can be determined from a small number of bench-scale tests. If the systems of interests have similar bC_f values as shown in Fig. 3.11a-c, one can use the graphs to find the V_{Cmin}. For other bC_f values, one can use the correlations to construct the BL curves and find the V_{Cmin} from the intersection point of the BL curve and the LT curve. The maximum column length and the maximum velocity can be estimated from the pressure-drop limit and the simplified Ergun equation.

The breakthrough limit C_{br}/C_f is inversely related to the capture yield- the smaller the breakthrough limit, the higher the yield. At a fixed breakthrough limit, the yield increases with increasing dimensionless diffusion rate N_D and overloading factor bC_f (Fig. 3.3). For N_D >0.1, when C_{br}/C_f=0.1, the capture yield for all Langmuir systems is higher than 97%; for C_{br}/C_f=0.05, the yield is higher than 98 %.

The correlations for the BL curves have been developed for Langmuir isotherm systems with either constant pattern or non-constant pattern waves (Table 3.2). The values of N_D and bC_f required for the formation of constant pattern waves were found for various C_{br}/C_f values (Fig. 3.6d). For bC_f >5 and N_D >0.2, constant pattern waves can form when the breakthrough concentration is 0.1 C_f.

The accuracy of the design method and the correlations of the BL curves has been verified using 14 frontal curves of Protein A affinity chromatography reported by the literature. The values of V_{Cmin} predicted by the design method agree closely with the experimental column volumes.

The effects of material properties, loading time, and feed conditions on V_{Cmin} can be found from the graphs of V_{Cmin}^{*} vs. t^{*} (Fig. 3.11a-c). When the dimensionless loading time t^{*} is less than 0.1, V_{Cmin}^{*} decreases rapidly with increasing t^{*}. When t^{*} is greater than 0.5, the loading fraction approaches 1, and the minimum column volume approaches that for an ideal system. If the total amount of solute to be recovered is fixed, a small column volume can be achieved with a high feed concentration, a large equilibrium capacity, and a small diffusion time relative to the loading time. A small loading time results in a large productivity but also a large column volume.

The intrinsic parameters and dimensionless groups, which are independent of the scale of the capture process, are used in this design method. The method is efficient, scalable, and should be widely applicable. If the scale of production, the feed conditions (C_f and V_f), the material properties (a, b, R, D_p, ε_b and ε_p), or the design requirements (t_L, C_{br}/C_f, and ΔP_{max}) change, the minimum column volume and the maximum productivity for capture can be quickly re-estimated.

CHAPTER 4. DESIGN OF AFFINITY CHROMATOGRAPHY FOR MOLYBDENUM-99 RECOVERY FROM URANIUM FISSION PRODUCTS

4.1 Introduction

Molybdenum-99 (Mo-99) is the precursor of technetium-99m (Tc-99m), an isotope used in 70,000 diagnostic scans per day (Van Noorden 2013). The primary source of Mo-99 is the fission of Uranium-235 (U-235) (Chuen et al. 2006). Currently, about 95% of Mo-99 is produced using highly enriched uranium (HEU) targets (Vandegrift 2005). The global supply relies mainly on four government-subsidized reactors built in 1950-1960. In 2009, two of the reactors were temporarily shut down for maintenance. In 2016, the reactor in Canada, which supplies over 60% of the Mo-99 demanded by the U. S., will end production. Therefore, there has been a significant demand for developing U. S.-based sources of Mo-99. Moreover, it is important for national security reasons to replace HEU with low-enriched uranium (LEU) in either uranyl nitrate or uranyl sulfate solutions (Ball 1997; Glenn 2011; Piefer 2011) for producing Mo-99.

Argonne National Laboratory and Purdue University are developing an affinity chromatography process for recovering Mo-99 from uranyl sulfate solutions containing LEU. The process has four major steps: pre-equilibration, capture, washing, and stripping (Fig. 4.1).

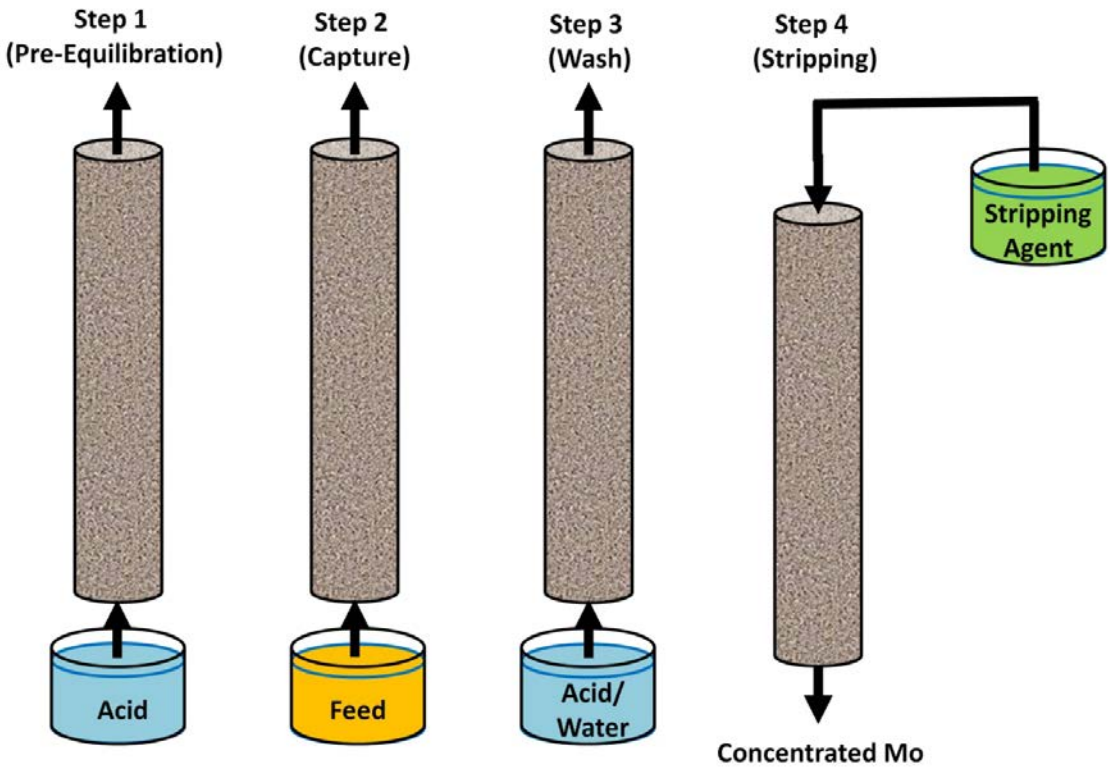

Figure 4.1. Procedures for Mo-99 capture and stripping.

A chromatography column is first pre-equilibrated with a solution which has the same pH as the feed. A feed solution containing Mo, uranium, and other fission products is then loaded onto the column. The Mo is selectively captured by the sorbent, whereas the other species are nearly non-adsorbing and hence pass through the column. A subsequent washing step removes the non-adsorbing species remaining in the voids and pores. In the stripping step, the flow direction is reversed. A species that can compete for the adsorption sites is used to strip Mo from the sorbent, and a concentrated product peak is then obtained.

Since U-235 experiences α decay and many of its fission products undergo β decay, robust materials have to be used in this process to resist radiation. In nuclear facilities, vacuum/gravity fluid transfer methods are preferred over pressurized systems, so that the pressure drop has to be lower than 1 atm. The time for capture and stripping must be kept within several hours because Mo-99 has a short half-life (66 hrs). The sorbent must have high selectivity and capacity for Mo to ensure high purity and productivity. The operating conditions of loading and stripping processes should be carefully selected so that Mo can be fully recovered with reasonably high concentration, and the stripping agent usage can be minimized. Therefore, developing an efficient capture and stripping process for Mo recovery is challenging.

Preliminary screenings indicated that a titania (TiO_2) sorbent, which is resistant to radiation, has a high selectivity and capacity for Mo in concentrated uranyl nitrate or uranyl sulfate solutions (Stepinski et al. 2007; 2010). The adsorption mechanisms of Mo and the stripping agents on the sorbent were investigated. The capture and stripping processes were properly modeled and simulated. The general

design method introduced in Chapter 3 was used to find the minimum TiO_2 column volume, the maximum column length, and the maximum velocity that satisfy the desired capture yield, loading time and pressure drop for Mo capture. VERSE simulations were used to find the optimal stripping conditions for achieving high product concentration and short stripping time.

4.2 Adsorption mechanisms and isotherm models

4.2.1 Adsorption sites of titania sorbent

Titania is a complex sorbent with multiple adsorption sites (McNeff et al. 2005), which are the Brønsted acid (BA) sites, the Brønsted base (BB) sites, and the Lewis acid (LA) sites. At a high pH, the OH^- in the solution can react with the protons on the BA sites (TiOH) to form TiO^- ions, which have a high affinity for cations (Fig. 4.2a). At a low pH, the BB sites (Ti-O-Ti) can bind with protons in the solution, and then become attractive to anions (Fig. 4.2b). The LA sites (Ti) are coordinatively unsaturated titanium atoms, which have vacant orbitals to accept electrons (Fig. 4.2c). Many Lewis bases with extra electrons, such as OH^-, PO_4^{3-}, SO_4^{2-}, and MoO_4^{2-}, can adsorb onto the LA sites. The adsorbed multivalent anions on the LA sites can serve as additional adsorption sites for cations.

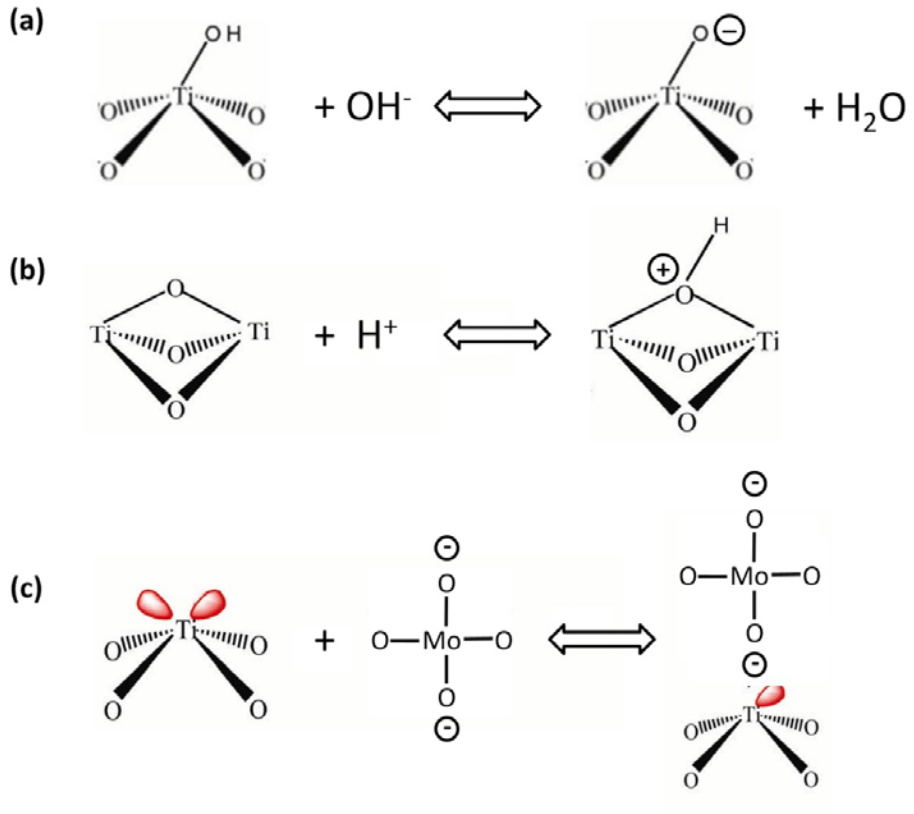

Figure 4.2. Properties of (a) Brønsted acid sites, (b) Brønsted base sites, (c) Lewis acid sites in TiO_2.

Fig. 4.3 shows the proposed mechanisms for Mo loading and stripping. At a low Mo concentration (<1 mM), Mo-99 is in the form of MoO_4^{2-} in the solution at pH 1 (Stepinski et al. 2010). The TiO_2 sorbent is first presaturated with pH 1 sulfuric acid, which can adsorb onto the BB sites and the LA sites. During the feed loading, Mo can adsorb onto the BB sites and the LA sites to replace some of the sulfate groups. In the stripping step with strong bases, the OH^- ions can react with the protons on the BA sites, neutralize the acids adsorbed on the BB sites, and displace the adsorbed sulfate and molybdate from the LA sites. These mechanisms were assumed in the modeling and the simulations of the loading and stripping processes.

4.2.2 Effective single-component Langmuir isotherm for Mo capture

When the adsorption and desorption rates are much faster than the mass transfer rates, the solid-phase concentration and the solution-phase concentration can reach local equilibrium, and can be correlated by an equilibrium adsorption isotherm equation. In this study, the Langmuir isotherm equation was used to describe the adsorption of various species. For Mo capture, the feed solution was mainly composed of sodium molybdate and uranyl sulfate. The isotherm equation for Mo can be written as:

$$q_{Mo} = \frac{a_{Mo} C_{Mo}}{1 + b_{US} C_{US} + b_{Mo} C_{Mo}} \tag{4.1}$$

where a_{Mo} and b_{Mo} are the linear and nonlinear Langmuir isotherm parameters of molybdate, respectively; b_{US} is the nonlinear Langmuir isotherm parameter of uranyl sulfate; q_{Mo} is the solid phase concentration of molybdate in equilibrium with the solution phase concentration C_{Mo}; C_{US} is the solution phase concentration of uranyl sulfate.

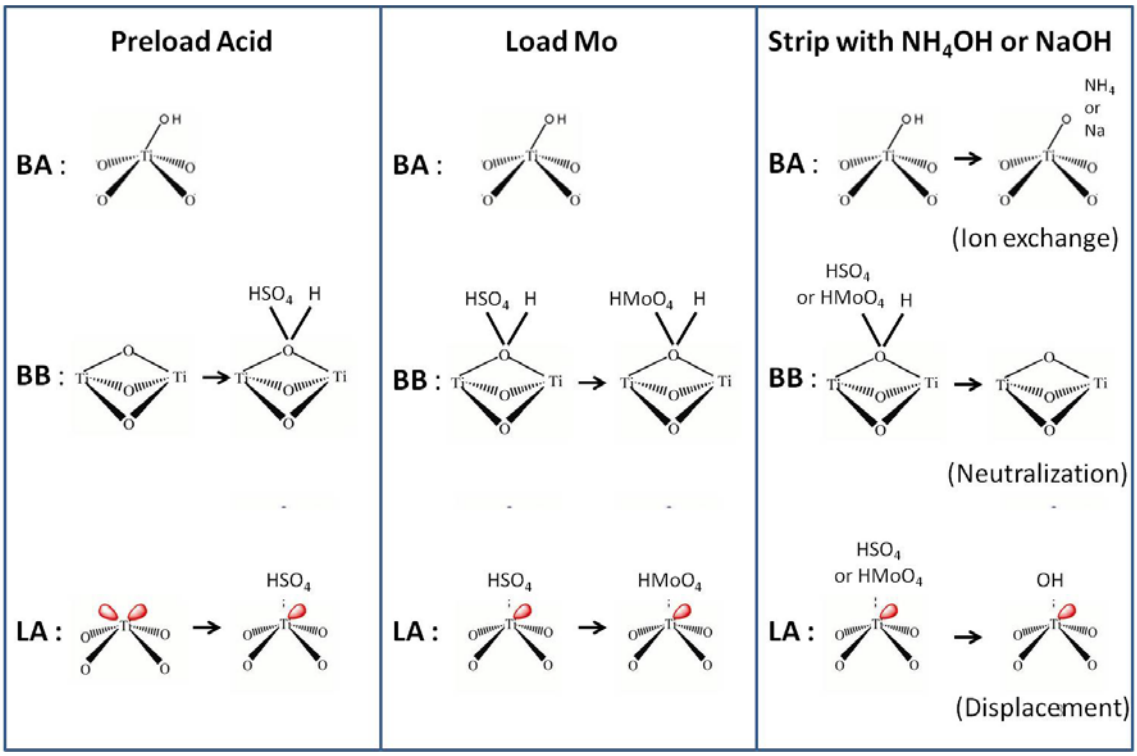

Figure 4.3. Hypothetical mechanisms for Mo loading and stripping.

Since the feed solutions of interests have low Mo concentrations (<0.1 mM) and high uranyl sulfate concentrations (0.38-0.63 M), and the affinity of uranyl sulfate for the sorbent was found to be orders of magnitude lower than that of molybdate, the frontal wave of uranyl sulfate migrates much faster than that of Mo. Therefore, the Mo adsorption can be considered to occur in the presence of a constant uranyl sulfate concentration. In this case, the multi-component Langmuir isotherm equation, Eq. (4.1), can be simplified into an effective single-component isotherm equation as follows:

$$q_{Mo} = \frac{(\frac{a_{Mo}}{1+b_{US}C_{US}})C_{Mo}}{1+(\frac{b_{Mo}}{1+b_{US}C_{US}})C_{Mo}} = \frac{aC_{Mo}}{1+bC_{Mo}} \tag{4.2}$$

where the parameters *a* and *b* are varied with uranyl sulfate concentration in the background solution.

4.2.3 Multi-component Bi-Langmuir isotherm for Mo stripping

As shown in Section 4.2.1, the stripping agent can interact with different adsorption sites. This feature is important for predicting the elution volume and the concentration of the product peaks. The Bi-Langmuir isotherm model thus was needed for simulating the stripping process. Since Mo can adsorb onto the BB sites and the LA sites, we defined Site 1 in the Bi-Langmuir model as the total of the two sites, which do not need to be distinguished from each other. Site 2 was defined as the BA sites, which can only interact with the stripping agent. Based on this model, Mo can only adsorb on Site 1 as a single component during the capture. In the

stripping step, the stripping agent can adsorb on Site 2, and also displace Mo from Site 1.

$$q_{SA} = \frac{a_1 C_{SA}}{1 + b_1 C_{SA}} + \frac{a_2 C_{SA}}{1 + b_2 C_{SA}} \tag{4.3}$$

where the subscripts "1" and "2" represent Site 1 and Site 2, respectively; q_{SA} is the solid phase concentration of the stripping agent in equilibrium with the solution phase concentration C_{SA}.

For the sorbent loaded with sulfuric acid, uranyl sulfate, and sodium molybdate, the effective adsorption capacity for the stripping agent is different from the actual capacity. On the BB sites, 1 mole of adsorbed H_2SO_4 or H_2MoO_4 needs 2 moles of OH^- to neutralize. On the LA sites, 1 mole of adsorbed Lewis base needs 1 mole of OH^- to displace and another 1 mole of OH^- to neutralize. As a result, the apparent capacities of the BB sites and the LA sites for the monovalent stripping agent (e.g., NaOH or NH_4OH) are twice the actual capacity.

4.3 Design of titania column for Mo capture

4.3.1 Estimation of intrinsic parameters

The Mo adsorption isotherm in the presence of 0.38 M, 0.55 M, and 0.64 M uranyl sulfate were obtained via batch adsorption equilibrium tests at 60 °C. The conditions were similar as those for the broth obtained from the fission of uranium. The effective single-component Langmuir isotherm model was applied to fit the data (Fig. 4.4). The best fitted Langmuir isotherm parameters are listed in Table 4.1.

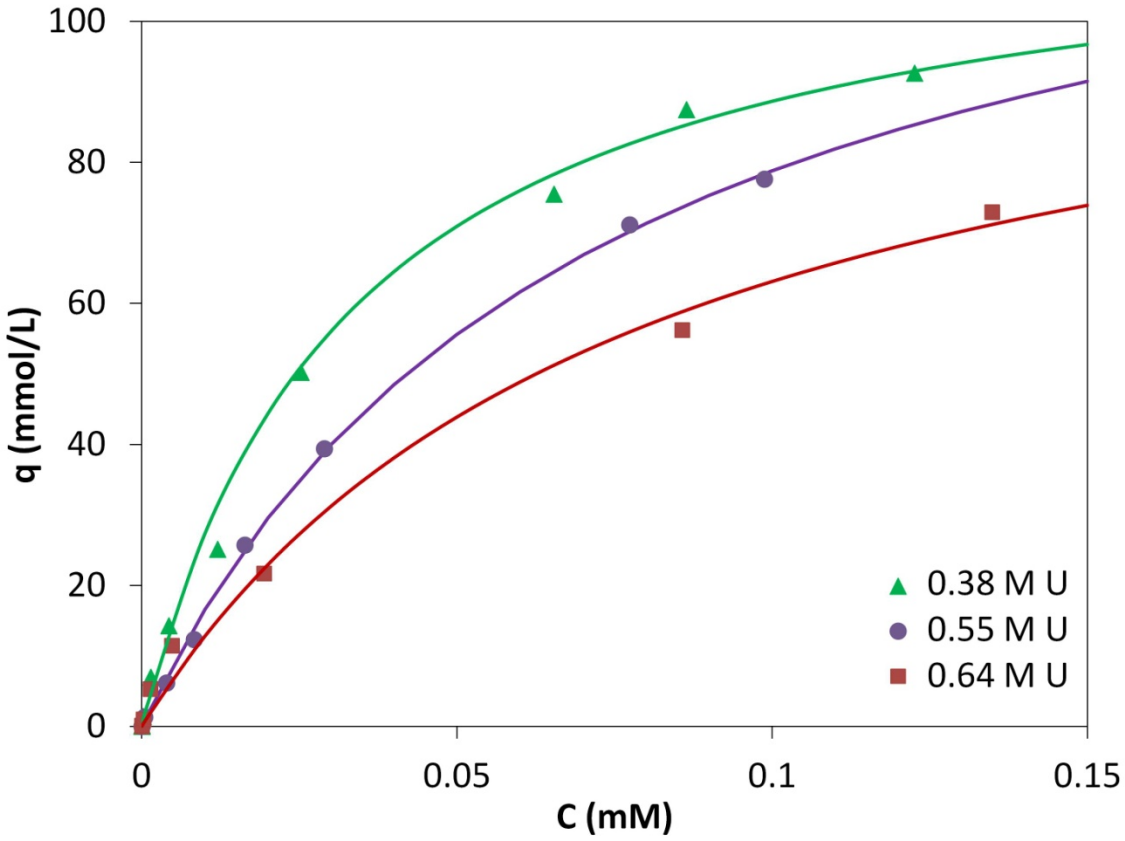

Figure 4.4. Mo adsorption isotherms at 60 °C under different uranyl sulfate concentrations. The curves are Langmuir fitting of the data points.

Table 4.1 Effective Mo isotherm parameters at 60 °C under different uranyl sulfate concentrations

Uranyl sulfate Conc.	*a*	*b* (1/mM)
90 g-U/L (0.38 M)	3547	30.0
130 g-U/L (0.55 M)	1892	14.0
150 g-U/L (0.64 M)	1441	12.8

Pulse tests using 1 g/L albumin and 1 M $NaNO_3$ were used to determine the bed void fraction and the porosity, respectively. The values of ε_b and ε_p were determined from the retention volumes of the tracers using Eq. (2.1a-c). The average bed void fraction of this sorbent was found to be 0.35 ± 0.01, and the average porosity was 0.40 ± 0.02.

The Brownian diffusivity (D_b) of MoO_4^{2-} in water at 25 °C was reported to be 8.3 × 10^{-4} cm^2/min (Marcus 1997). The Stokes-Einstein equation was used to correct for viscosity and temperature effects. The result showed that D_b=1.41 × 10^{-3} cm^2/min in 0.38 M uranyl sulfate solution at pH 1 and 60 °C. Two Mo frontal curves were obtained from 1 cm *L* × 0.66 cm *ID* columns at 3 and 5 cm/min, respectively, with 0.38 M uranyl sulfate in the feed. VERSE simulations were implemented to find the D_p value that can fit the experimental data for both runs. The best fitting indicated that D_p=4.0 × 10^{-5} cm^2/min, or D_b/D_p=35 (Fig. 4.5a-b). The intrinsic, system, and numerical parameters used in the VERSE simulations for frontal curve fitting are listed in Table 4.2.

4.3.2 Testing of the design method

Two Mo breakthrough curves were obtained from 5 cm *L* × 0.66 cm *ID* columns at 10 cm/min with 0.38 M uranyl sulfate in the feed. The Mo concentrations in the feed were 0.01 and 0.1 mM, respectively (Fig. 4.6a-b), and the corresponding bC_f values were 0.3 and 3. The breakthrough times t_{br} for C_{br}=0.1C_f were found to be 293 and 162 min, and the loading volumes V_f were 996 and 549 mL. The theoretical minimum column volumes V_{Cmin} for the given loading times and loading volumes can be found from Fig. 3.11a. The results are summarized in Table 4.3, which shows that the differences between the experimental column volume and the predicted column volume were less than 10%.

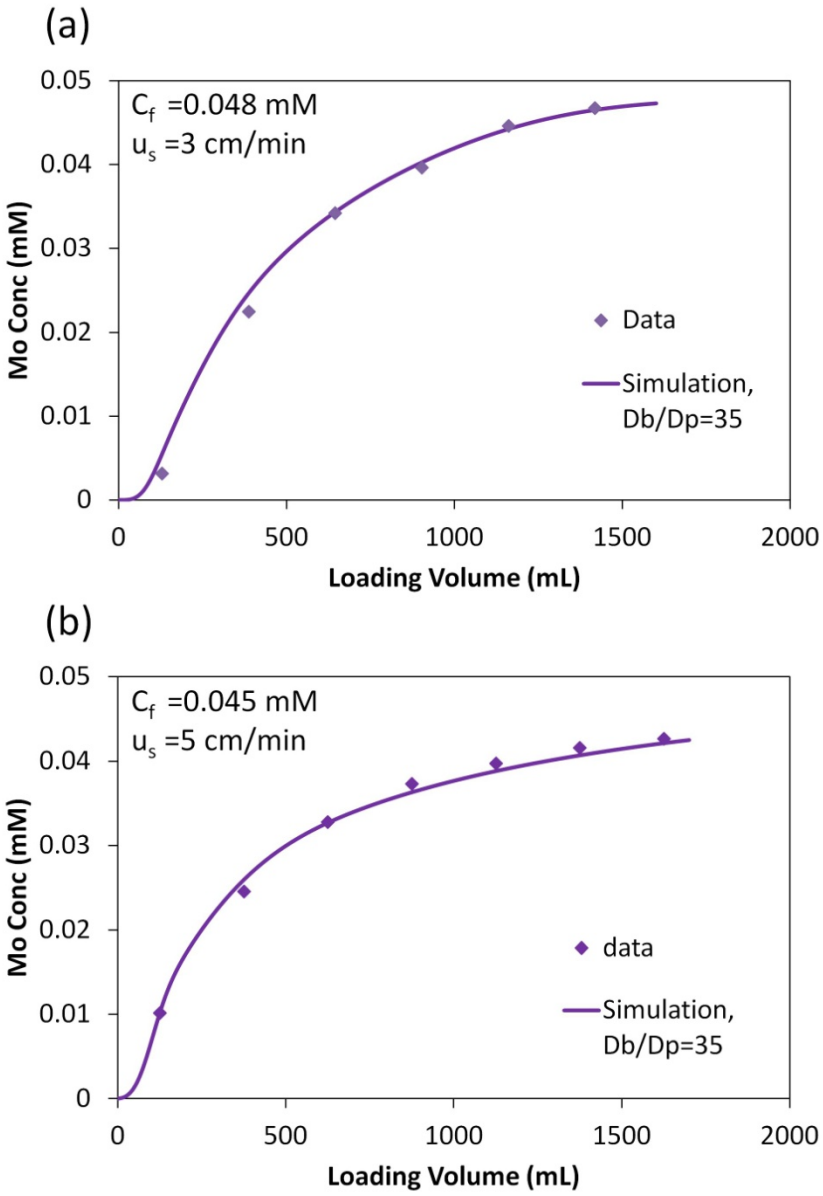

Figure 4.5. Frontal curves of Mo loading with various velocities: (a) 3 cm/min, (b) 5 cm/min. The column size is 1 cm *L* × 0.66 cm *ID*. The feed concentrations were slightly different: (a) 0.048 mM ; (b) 0.045 mM. The diamonds are the Mo concentrations determined by gamma counting, and the curves were obtained from VERSE simulations with the best fitting of D_p.

Table 4.2 Parameters used in VERSE simulations for Mo capture

System Parameters			
Sorbent	R (μm)	ε_b	ε_p
Sachtopore	55	0.35	0.4
Mass Transfer Parameters			
D_b (cm^2/min)	D_p (cm^2/min)	k_f (cm/min)	E_b (cm^2/min)
0.00141	0.00004	From Wilson and Geankoplis (1966)	From Chung and Wen (1968)
Isotherm Parameters (Langmuir)			
a (L solution volume/L packing volume)		b (1/mM)	
3547		30	

Numerical Parameters					
Axial Elements	Step Size ($L\varepsilon_b/u_s$)	Collocation Points		Tolerance	
		Axial	Particle	Absolute (mM)	Relative
50	0.1	4	6	10^{-9}	10^{-6}

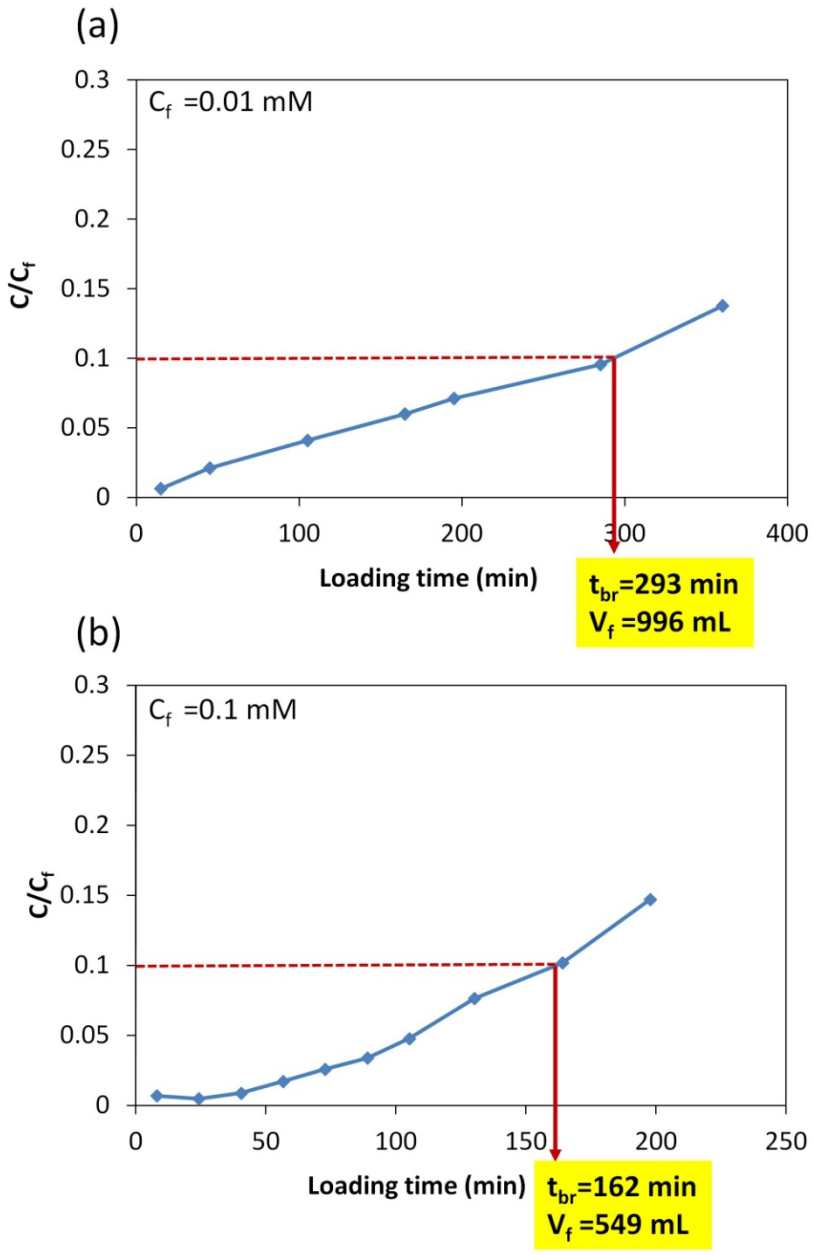

Figure 4.6. Effluent histories of the breakthrough tests with different feed concentrations: 0.01 mM (a); 0.1 mM (b). The column size was 5 cm *L* × 0.66 cm *ID*, and the velocity was 10 cm/min. The breakthrough times and loading volumes identified for 0.1 C_f were 293 min/996 mL (a); and 162 min/549 mL (b). The minimum column volumes obtained from the t_{br} and V_{br} using the general design method are shown in Table 4.3.

Table 4.3 Comparison of experimental V_C and calculated V_{Cmin}

	(a)	(b)
C_f (mM)	0.01	0.1
V_C (mL)	1.71	1.71
V_{Cmin} (mL)	1.56	1.54
Error (%)	8.8	9.9

4.3.3 Production-scale design and sensitivity analysis

The general method introduced in Chapter 3 was employed to design a production-scale column for Mo capture. A batch of 250 L feed solution, which contains 0.002 mM Mo and 0.38 M uranyl sulfate, is required to be captured within 2 hours. The Mo breakthrough concentration should be 10% of the feed concentration and the maximum pressure drop should be 0.8 atm. Since the bC_f value is less than 0.1, we can approximately use the curve for bC_f =0 in Fig. 3.11a to estimate V_{Cmin}, L_{max} and u_{smax}. The intrinsic parameters (ε_b, ε_p, R, a, b, D_p) and the design solutions are listed in Table 4.4.

In practice, however, the feed concentration may vary among different batches. The sorbent particle size, pore structure, and porosity may differ among different lots. The bed void fraction may vary because of inconsistent packing. The variation of flow rate can affect the total loading volume. The fluctuation of temperature can affect the isotherm parameters and the intra-particle diffusivity. Hence, the values of C_f, R, ε_p, ε_b, V_f, a, b, and D_p can deviate from their targets. These variations, except that of feed volume V_f, can affect the value of t^*. The possible errors for each variable and the upper bound (UB) and lower bound (LB) for t^* are shown in Table 4.5. The resulting difference in $V_{Cmin}{}^*$, as shown in Fig. 4.7a, indicates the maximum variations of the estimated V_{Cmin} that needs to be considered in the production-scale design.

In addition, the variation of V_f caused by the flow rate fluctuation can also affect the calculation of V_{Cmin}, Eq. (3.9). A safety factor for V_{Cmin} can be calculated by taking into account the variations of $V_{Cmin}{}^*$ and V_f.

$$\text{Safety Factor} \equiv \frac{V_{C\min}(UB)}{V_{C\min}(LB)} = \frac{V_f(UB)}{V_f(LB)} \frac{V_{C\min}{}^*(UB)}{V_{C\min}{}^*(LB)} \tag{4.4}$$

Table 4.4 Production-scale design

Intrinsic parameters					
ε_b	ε_p	R (μm)	a	b (1/mM)	D_p (cm^2/min)
0.35	0.4	55	3547	30	4×10^{-5}
Design requirements					
C_{br}/C_f			ΔP_{max} (atm)		
0.1			0.8		
Loading conditions and target solutions					

Conditions			Solutions				Verifications
C_f (mM)	V_f (L)	t_L (min)	V_{Cmin} (mL)	u_{smax} (cm/min)	ID_{min} (cm)	L_{max} (cm)	C_{br}/C_f at u_{smax} (Simulation)
0.002	250	120	575.3	50.8	7.2	14.0	0.092

Table 4.5 Possible errors for variables in the determination of V_{Cmin}

Variables	Possible Errors (%)
ε_b	±10
ε_p	±10
D_p	±20
C_f	±10
a,b	±10
R	±10
Upper Bound (UB) of t^*	+90
Lower Bound (LB) of t^*	-50
V_f	±5

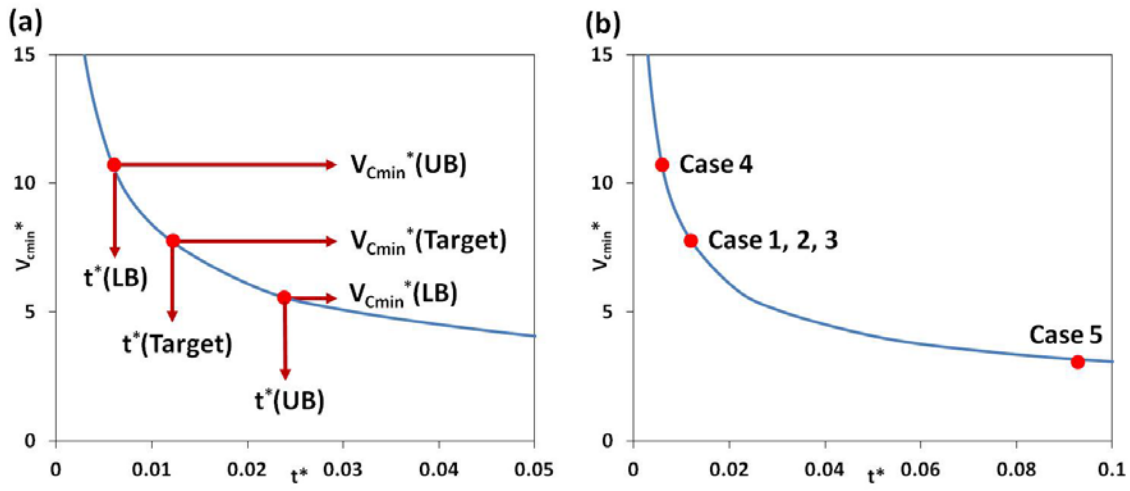

Figure 4.7. (a) Production-scale design and sensitivity analysis, in which "LB" refers to the lower bound shift, and "UB" refers to the upper bound shift. The design requirements, loading conditions, and target solutions are listed in Table 4.4. (b) Adaptive designs for variations in loading conditions and material properties. The design requirements and target solutions for each case are listed in Table 4.6.

As shown in Fig. 4.7a, a safety factor of 2 was found to be sufficient for designing the column.

4.3.4 Adaptive designs to variations in loading conditions and material properties

The column design obtained in the previous section can be easily adapted to variations in loading conditions and material properties. For the sake of simplicity, the safety factor is not considered here. The requirements and results listed in Table 4.4 are used as the benchmark, which is marked as Case 1 in Table 4.6. In Case 2, the loading volume V_f is doubled from that of Case 1, and the other variables remain the same. Since t^* is not affected by feed volume, $V_{Cmin}{}^*$ remains unchanged on the curve (Fig. 4.7b). Therefore, $N_{Dmin}=t^*V_{Cmin}{}^*$ is unchanged, and the maximum column length L_{max} and velocity u_{smax} remain the same, Eq. (3.7). The minimum column volume $V_{Cmin}=V_{Cmin}{}^*V_f/a^*$ is proportional to V_f and is thus doubled from that of Case 1. To remain the same L_{max}, the minimum column cross-sectional area A_{Cmin} should be doubled.

In Case 3, the total loading amount C_fV_f is fixed, but the loading volume V_f and the feed concentration C_f are varied. Since the value of bC_f is small, t^* is approximately fixed, and $V_{Cmin}{}^*$ remains unchanged. The resulting u_{smax} and L_{max} remain the same. The value of V_{Cmin} and A_{Cmin} are, again, proportional to V_f, and the results end up the same as those for Case 2.

In Case 4, the loading time is decreased by half from 2 hrs to 1 hr, and the other variables are kept the same. As a result, t^* is also reduced by half, and $V_{Cmin}{}^*$ increases by 36% (Fig. 4.7b). The value of V_{Cmin} increases proportionally with $V_{Cmin}{}^*$, because a faster loading causes more serious wave spreading. In general, there is a trade-off between

throughput and column utilization. Since $N_{Dmin}=t^{*}V_{Cmin}^{*}$ decreases, L_{max} also decreases, whereas u_{smax} becomes higher, Eq. (3.7). A larger V_{Cmin} but a smaller L_{max} leads to a larger A_{Cmin}.

In Case 5, the particle radius is decreased from 55 μm to 20 μm, which is the smallest size supplied by the manufacturer. The t^{*} value increases some 7.6 fold and the V_{Cmin}^{*} value decreases by 59% (Fig. 4.7b) . The value of V_{Cmin} decreases proportionally with V_{Cmin}^{*}, as a result of a shorter diffusion time and less wave spreading. Although $N_{Dmin}=t^{*}V_{Cmin}^{*}$ increases, both L_{max} and u_{smax} decrease at a smaller particle size, Eq. (3.7). The cross-sectional area A_{Cmin} is found to be larger than that for Case 1.

The design solutions for the above examples were obtained graphically and were input to VERSE for verification. The simulated breakthrough concentrations were all close to but slightly lower than $C_{br}/C_{f}=0.1$ (Table 4.6). The small deviations arises from the approximation of $bC_{f} \approx 0$, but they were advantageous in terms of conservative designs. The results indicate that the column designs can be carried out with sufficiently high accuracy without running rate-model simulations .

Table 4.6 Adaptive designs to variations in loading conditions and sorbent particle size

Design requirements									
C_{br}/C_f				ΔP_{max} (atm)					
0.1				0.8					
Conditions and solutions									
Case	Conditions				Solutions				Verifications
	C_f (mM)	V_f (L)	t_L (min)	R (μm)	V_{Cmin} (ml)	u_{smax} (cm/min)	ID_{min} (cm)	L_{max} (cm)	C_{br}/C_f at u_{smax} (Simulation)
1	0.002	250	120	55	575.3	50.8	7.2	14.0	0.092
2	0.002	500	120	55	1150.6	50.8	10.2	14.0	0.091
3	0.001	500	120	55	1150.6	50.8	10.2	14.0	0.089
4	0.002	250	60	55	784.5	61.5	9.3	11.6	0.090
5	0.002	250	120	20	235.3	28.9	9.6	3.3	0.095

4.4 Design of Mo stripping processes

4.4.1 Capacity of the adsorption sites of titania sorbent

The design of Mo stripping processes was based on reliable models and simulations, which require fundamental understandings of adsorption/desorption mechanisms and quantitative analysis of each adsorption site. As described in Section 2.2, the capacity of the BB sites was determined from the breakthrough volume of HNO_3 (Fig. 4.8a) using Eq. (2.2). The value is 0.24 mol/L column volume. The total capacity of the BA sites and the LA sites was found from the breakthrough volume of NaOH (Fig. 4.8b), and the value is 0.69 mol/L column volume.

To further confirm the adsorption mechanisms and capacities, the NaOH-preloaded column was fed with 0.11 M HNO_3. Based on the features of different adsorption sites, the loaded HNO_3 could: (1) replace Na^+ with H^+ on the BA sites and form $NaNO_3$ in the solution; (2) adsorb onto the BB sites; (3) neutralize the NaOH on the LA sites and form $NaNO_3$ in the solution. Therefore, prior to the breakthrough of HNO_3, a $NaNO_3$ zone was formed with the following concentration (Fig. 4.8c):

$$C_{NaNO_3} = 0.11\,(\frac{0.69}{0.69+0.24}) = 0.082\ M \tag{4.5}$$

The HNO_3-presaturated column was then fed with 0.1 M NaOH, which had the following actions: (1) replace H^+ with Na^+ on the BA sites; (2) neutralize HNO_3 on the BB sites and form $NaNO_3$ in the solution; (3) adsorb onto the LA sites. Thus, a $NaNO_3$ zone was also formed ahead of the NaOH front (Fig. 4.8d), with the concentration of

$$C_{NaNO_3} = 0.11\,(\frac{0.24}{0.69+0.24}) = 0.026\ M \tag{4.6}$$

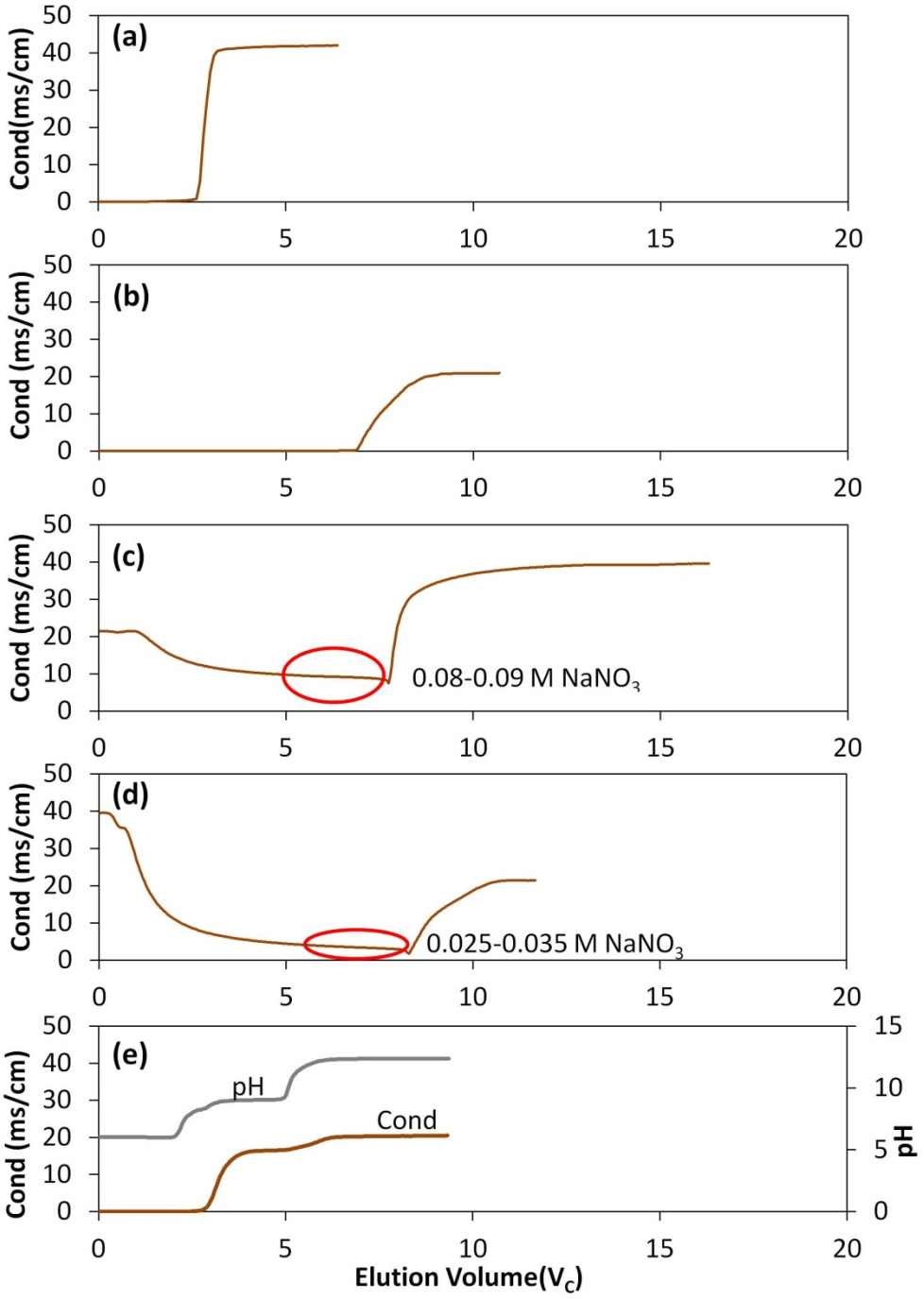

Figure 4.8. Frontal tests for estimating the capacities of different adsorption sites. (a) 0.11 M HNO_3 loaded to a clean column; (b) 0.1M NaOH loaded to a clean column; (c) 0.11 M HNO_3 loaded to a NaOH preloaded column; (d) 0.1 M NaOH loaded to a HNO_3 preloaded column; (e) 0.1 M Na_3PO_4 loaded on to a clean column.

Table 4.7 Preloading and loading conditions of the frontal tests for estimating the adsorption capacities for each sites. Column size: 6 cm *L* x 1.5 cm *ID* (V_C=10.6 mL); *F*=5 mL/min (u_s =2.8 cm/min)

Run #	Preloading	Loading
Figure 4.8a	H_2O	0.11 M HNO_3
Figure 4.8b	H_2O	0.1 M NaOH
Figure 4.8c	0.1 M NaOH	0.11 M HNO_3
Figure 4.8d	0.11 M HNO_3	0.1 M NaOH
Figure 4.8e	H_2O	0.1 M Na_3PO_4

When 0.1 M Na_3PO_4 was loaded onto the water-rinsed column, the PO_4^{3-} group can adsorb onto the LA sites, and the Na^+ can exchange with H^+ at the BA sites, because of a high pH in the solution (pH~12.4). Thus, it was not surprising to see two breakthroughs in the frontal test (Fig. 4.8e). The first breakthrough indicates the saturation of the LA sites, and the species on the plateau was Na_2HPO_4 (pH~9.0). The capacity of the LA sites was found to be 0.26 mol/L column volume, and the capacity of the BA site was calculated by 0.69-0.26=0.43 mol/L column volume. The second breakthrough corresponds to the saturation of the BA sites, and the species on the plateau was Na_3PO_4, which has the same conductivity and pH as the feed. The preloading and loading conditions for Fig. 4.8a-e are summarized in Table 4.7.

4.4.2 Mo stripping data and simulations

In the stripping tests, the feed solutions containing Mo and uranyl sulfate were first loaded onto a TiO_2 column for two hours. The adsorbed Mo was then stripped by 0.1 M NaOH (Fig. 4.9a-c) or 1 M NH_4OH (Fig. 4.10a-c). The elution volumes shown in Figs. 4.9-4.13 do not include the extra-column dead volumes. The average Mo product concentrations and stripping yields are listed in Table 4.8. The Mo product concentrations varied from 8 times to 56 times of the feed concentrations, and the yields ranged from 89% to 100%. The variations in yield could be due to assay errors at such low Mo concentrations ($C_f \approx 2$ μM).

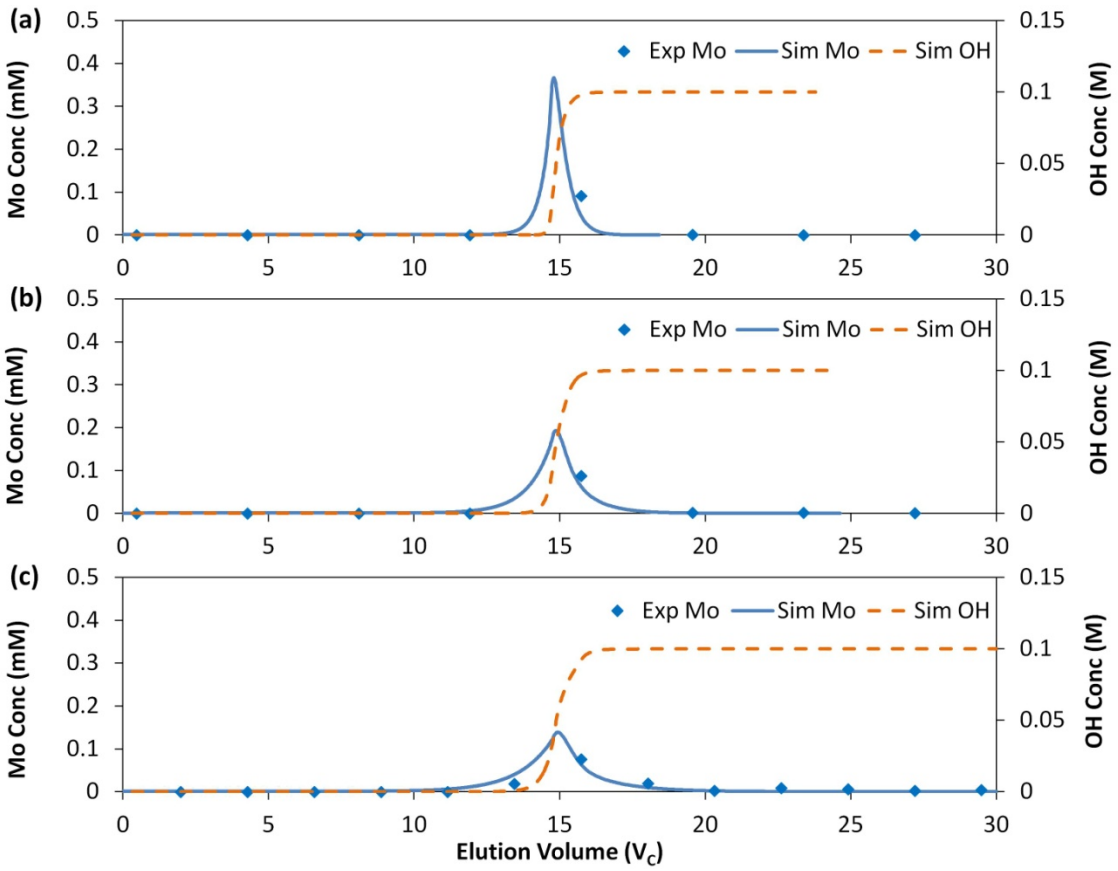

Figure 4.9. Experimental data and simulations results for Mo stripping using 0.1 M NaOH. The conditions, product concentrations, and yields are listed in Table 4.8. The parameters used in simulations are listed in Table 4.9.

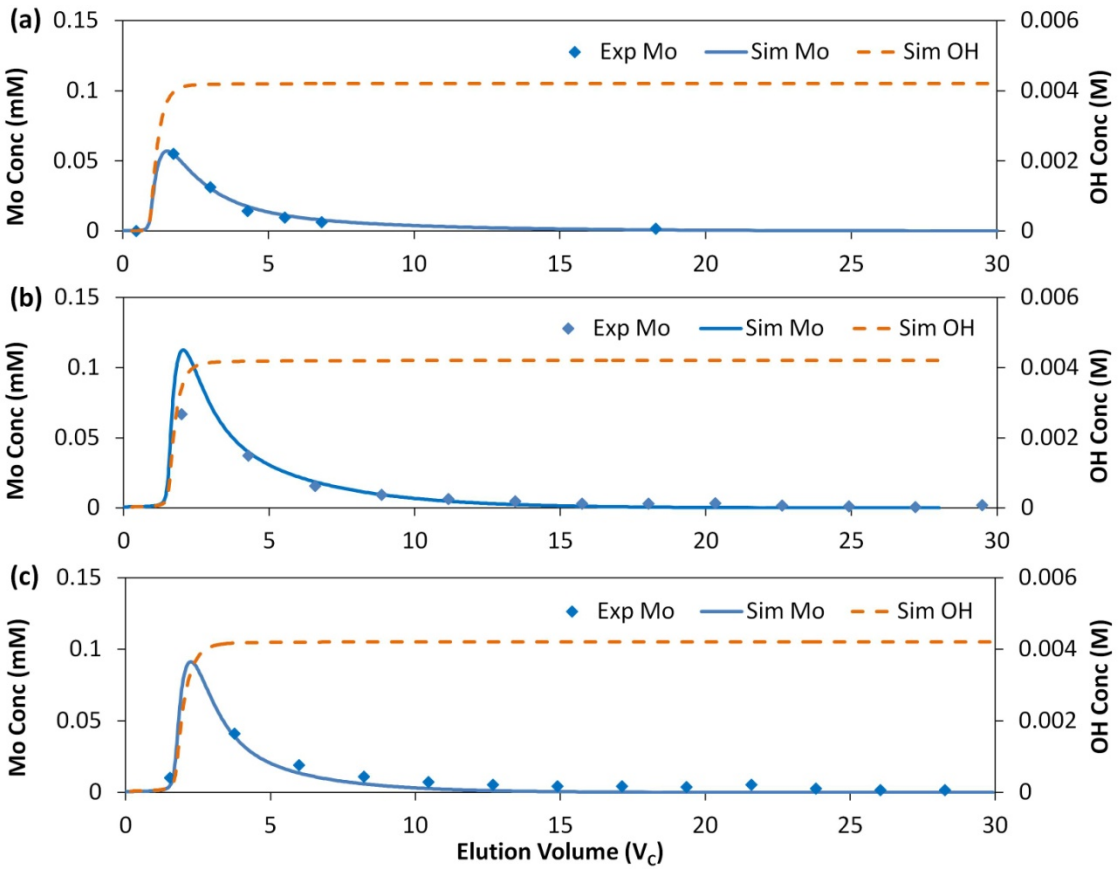

Figure 4.10. Experimental data and simulations results for Mo stripping using 1 M NH_4OH. The conditions, product concentrations, and yields are listed in Table 4.8. The parameters used in simulations are listed in Table 4.9.

Table 4.8 Experimental conditions, product concentrations, and yields of the stripping tests using 1 M NH_4OH and 0.1 M NaOH

Run#	*L*×*ID* (cm×cm)	u_s (Load) (cm/min)	t_L (min)	C_f (mM)	Background Solution	Stripping Agent	u_s (Strip) (cm/min)	Avg. Prod. Conc (C_f)	Yield (%)
Fig. 4.9a	5×1	7.0	120	0.0021	130 g-U/L (0.55 M)	0.1 M NaOH	1.0	56	100
Fig. 4.9b	5×1	7.0	120	0.0021	130 g-U/L (0.55 M)	0.1 M NaOH	3.0	28	100
Fig 4.9c	5×1	7.0	120	0.0021	130 g-U/L (0.55 M)	0.1 M NaOH	5.0	21	89
Fig. 4.10a	5×1	4.0	120	0.0017	90 g-U/L (0.38 M)	1 M NH_4OH	4.0	8	100
Fig. 4.10b	5×1	7.0	120	0.0021	130 g-U/L (0.55 M)	1 M NH_4OH	3.5	12	100
Fig. 4.10c	4×1	3.8	120	0.0036	146 g-U/L (0.64 M)	1 M NH_4OH	3.8	11	92

As shown in Fig. 4.9, the Mo stripping curves obtained using NaOH are relatively sharp, because OH^- adsorbs more strongly than Mo, and hence can displace Mo favorably from the sorbent. The peaks become more spread at a higher velocity because of a lower diffusion rate relative to convection rate. The loading and stripping processes were simulated by VERSE, and the results agree with the data. For Mo, the isotherm parameters used in the simulations were obtained from Table 4.1, and the diffusivity was obtained from Table 4.2. For NaOH, the effective capacities were estimated by using the strategies described in Section 4.2.3. The Brownian diffusivity was estimated from the literature data (Cussler 1984) with a temperature correction. The pore diffusivity was estimated from the Brownian diffusivities and the tortuosity (D_b/D_p) of this sorbent. The isotherm parameters were estimated by fitting the simulated curve shapes with the data. A summary of all the parameters used in the simulations are shown in Table 4.9. The feed concentrations and loading/stripping velocities are reported in Table 4.8.

When NH_4OH was used as the stripping agent, the Mo peaks show a great tailing (Fig. 4.10). The possible reason is that NH_4OH is a weak base and the reaction $NH_4^+ + OH^- \leftrightarrow NH_4OH$ has a large equilibrium constant ($5.65\times10^4\ M^{-1}$). This reaction lowers the effective affinity of OH^- for the sorbent and the concentration of OH^- in the solution. As a result, the OH^- can only unfavorably displace MoO_4^{2-} from the sorbent, leading to diffuse Mo desorption waves. This hypothesis was verified by taking into account the reaction in VERSE simulations, which generated very similar stripping curves as the data (Fig. 4.10). The sorbent capacity for NH_4OH is lower than that for NaOH, which was experimentally verified and considered in the simulations. The experimental conditions and simulation parameters are also listed in Table 4.8 and 4.9, respectively.

Table 4.9 Parameters used in VERSE simulations for Mo stripping

System Parameters

L (cm)	ID (cm)	R (μm)	ε_b	ε_p	CSTR (mL)
4 or 5	1	55	0.35	0.4	2

Isotherm Parameters

	a_1	b_1 (1/mM)	a_2	b_2 (1/mM)
Mo	3547 (0.38 M U) 1892 (0.55 M U) 1441 (0.64 M U)	30.0 (0.38 M U) 14.0 (0.55 g-U/L) 12.8 (0.64 M U)	0	0
NaOH	8,000	8	8,000	18.4
NH_4OH	8,000	50	8,000	115

Reaction Parameters

Reaction	k_+ ($mM^{-1}min^{-1}$)	k_- (min^{-1})	K_b (mM^{-1})
$NH_4^+ + OH^- \leftrightarrow NH_4OH$	565	10	56.5

Mass Transfer Parameters

	D_b (cm^2/min)	D_p (cm^2/min)	k_f (cm/min)	E_b (cm^2/min)
Mo	0.00141	0.00004	From Wilson and Geankoplis (1966)	From Chung and Wen (1968)
NaOH/ NH_4OH	0.0068	0.00023		

Numerical Parameters

Axial Elements	Step Size ($L\varepsilon_b/u_s$)	Collocation Points		Tolerance	
		Axial	Particle	Absolute (mM)	Relative
100	0.1	4	2	10^{-7} (Mo) 10^{-3} (NaOH/NH_4OH)	10^{-4}

To exclude the effect of extra-column mixing on peak spreading, simulations were run without the system dead volume for the NH_4OH stripping cases. The simulated peaks were similar as those with the system dead volume in Fig. 4.10, indicating that the Mo peak tailing was attributed to the thermodynamic spreading when a weakly-adsorbed agent is displacing a strongly-adsorbed species. Therefore, to achieve a high product concentration with efficient stripping, NaOH should be used as the stripping agent for Mo recovery.

4.4.3 CSTR dead volume effects on eluted Mo peak

The Mo elution peaks using 0.1 M NaOH with various stripping residence times (0.5-5 min) and CSTR dead volumes (2.5%-50% column volumes) were simulated. The results are shown in Fig. 4.11a-d. When the residence time is long, the mass transfer efficiency in the column was high, so that the extra-column mixing has a significant effect on peak spreading (Fig. 4.11a). As residence time decreases, the mass transfer resistance in the column becomes the dominant effect on peak spreading, and the elution peaks at different CSTR dead volumes tend to merge (Fig. 4.11b-d). In general, within the range of interest for this process (L/u_s =0.5-5 min), a CSTR dead volume less than 10% of the column volume can be regarded to have negligible effect on the shape of Mo elution peaks.

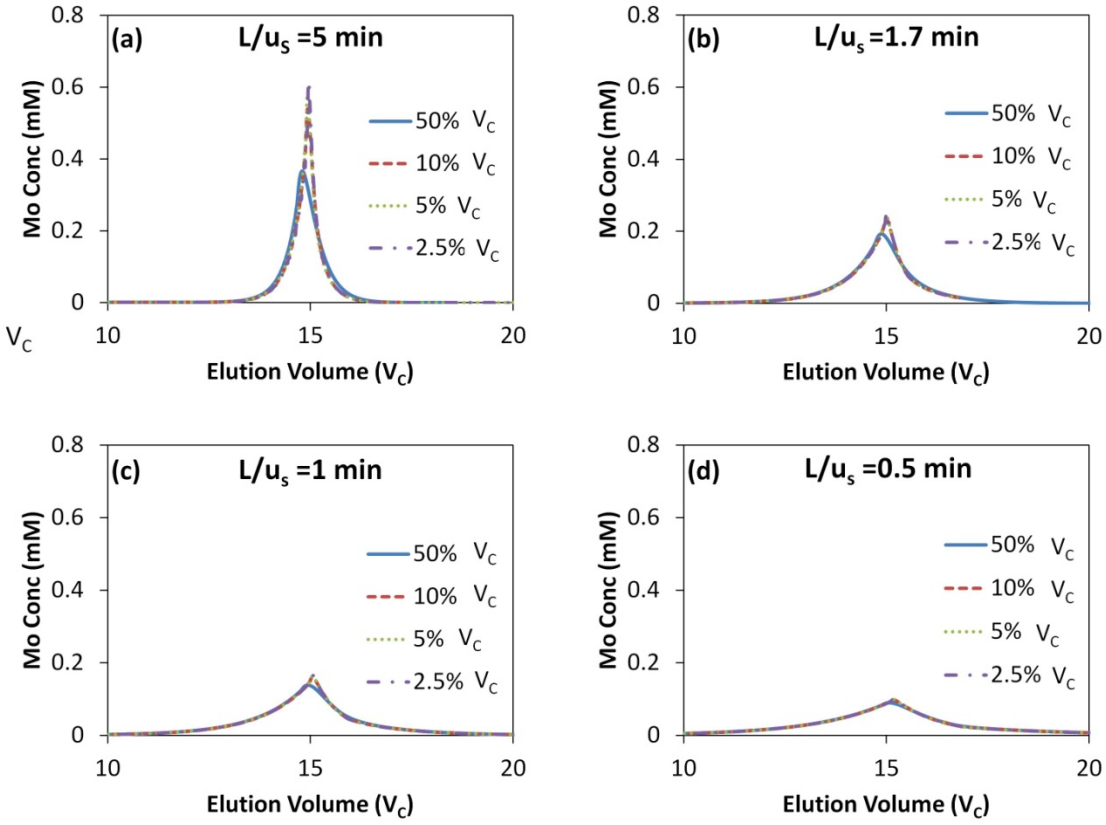

Figure 4.11. Simulated Mo elution peaks with different CSTR volumes and different residence times (L/u_s) for stripping. The column size was 5 cm L × 1 cm ID. The Mo isotherm parameters were the same as those in the 0.55 M U solution. The stripping agent isotherm parameters were the same as those of NaOH in Table 4.9.

4.4.4 Displacement model vs. modulator model for the stripping agent

In affinity chromatography, the target solute can be eluted by a stripping agent with two possible mechanisms: displacement and modulation. In the displacement model, the stripping agent adsorbs more strongly than the target solute, and can favorably replace the target which adheres to the sorbent. In the modulator model, the stripping agent does not adsorb, but acts as a modulator which can lower the affinity between the target and the sorbent. The Langmuir adsorption isotherm equation with modulators (Antia and Horvath 1989) is shown below.

$$q_{Mo} = \frac{ae^{-S_a C_{SA}} C_{Mo}}{1 + be^{-S_b C_{SA}} C_{Mo}} \tag{4.7}$$

where S_a and S_b are the modulator constants.

When using the modulator model, the predicted Mo peak elutes close to the total void volume. Different degrees of peak tailing can be simulated by varying the modulator constants. An example is shown in Fig. 4.12a. However, the modulation model cannot explain the delay of the eluted Mo peak and the NaOH front, which can be well interpreted by the displacement model.

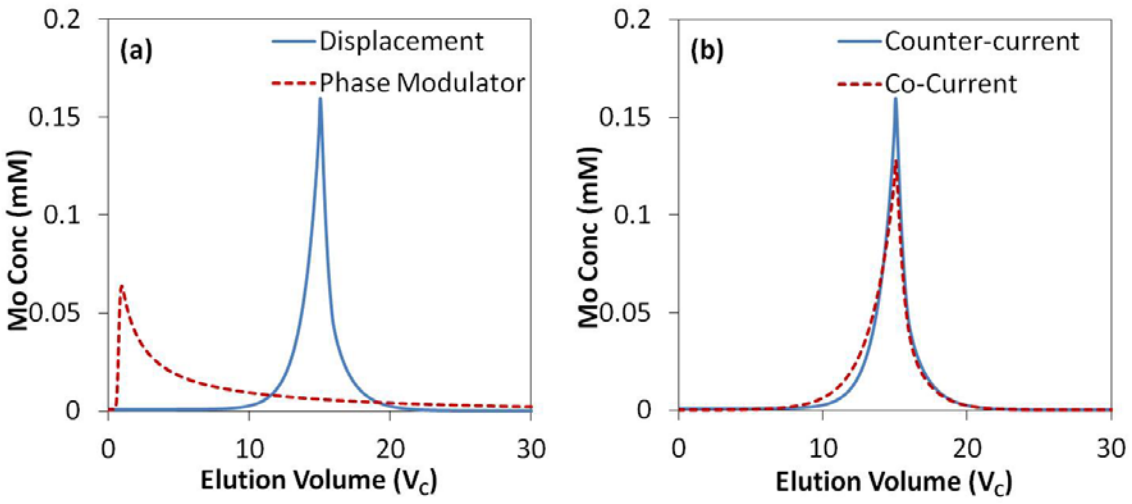

Figure 4.12. Comparison of simulated Mo elution peaks with different stripping mechanisms (a) and different flow directions (b). The column size was 5 cm *L* × 1 cm *ID*. The stripping velocity was 5 cm/min. The CSTR volumes were set 10% of the column volume. The Mo isotherm parameters were the same as those in the 0.55 M U solution.

4.4.5 Counter-current stripping vs. co-current stripping

In designing an efficient stripping process, it is important to understand whether counter–current stripping is advantageous over co-current stripping. The predictions based on the displacement model and parameters for 0.1 M NaOH stripping are shown in Fig. 4.12b. The results show that both stripping methods produce the same mass center of the eluted Mo peaks. Counter-current stripping leads to slightly sharper front and higher Mo product concentration than co-current stripping because the migration distance for the Mo peak is shorter.

4.4.6 Optimal conditions for Mo stripping

The simulated Mo elution peaks at various NaOH concentrations and stripping residence times (L/u_s) are shown in Fig. 4.13. The simulations were based on the displacement model and the counter-current stripping. The feed solutions, which had a Mo concentration of 0.002 mM and a batch volume of 660 mL, were loaded onto a 5 cm L × 1 cm *ID* column for 2 hours. The CSTR dead volume was assumed to be 10% of the column volume. The product concentrations normalized by the feed concentration are shown in Fig. 4.14a. At a fixed residence time, the average concentration of the eluted Mo peak increases with NaOH concentration. As the residence time decreases, the eluted Mo peak becomes more spread. If 1 M NaOH is used for stripping, for example, the average product concentration at L/u_s= 0.5 min is less than 1/3 of that at L/u_s= 5 min.

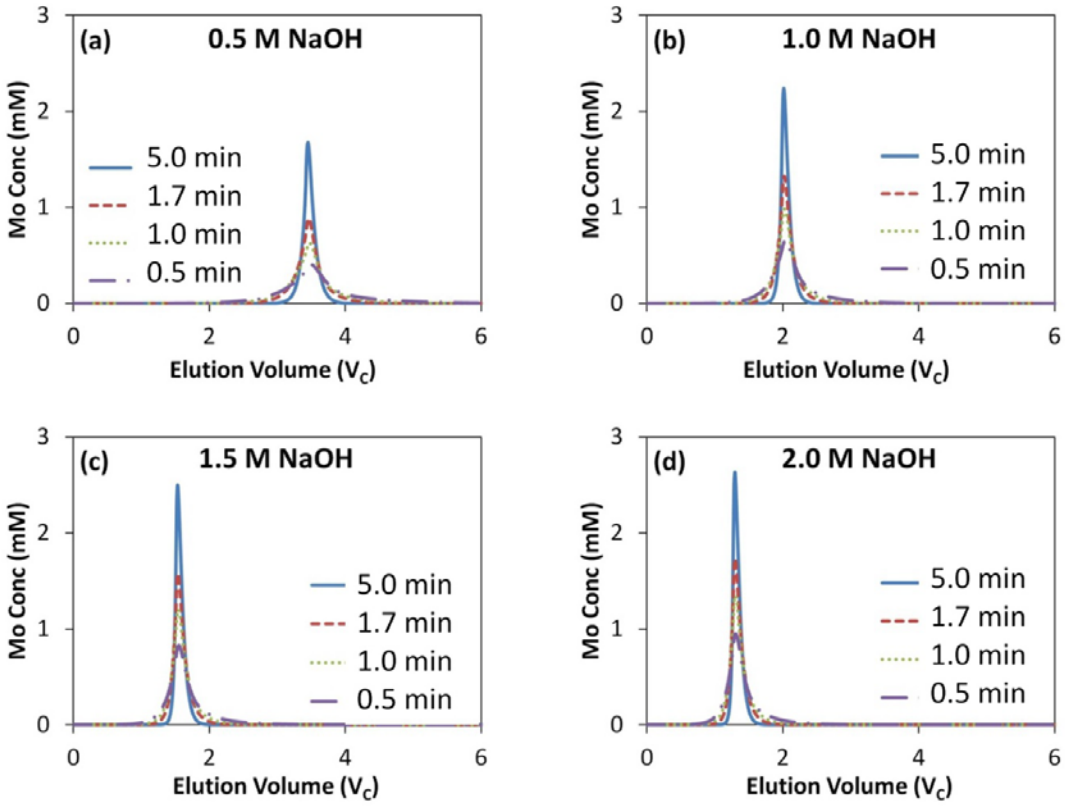

Figure 4.13. Simulated Mo elution peaks with different stripping agent concentrations and residence times (L/u_s). The CSTR volumes were set 10 % of the column volume. The Mo isotherm parameters were the same as those in the 0.55 M U solution. The stripping agent isotherm parameters were the same as those of NaOH in Table 4.9.

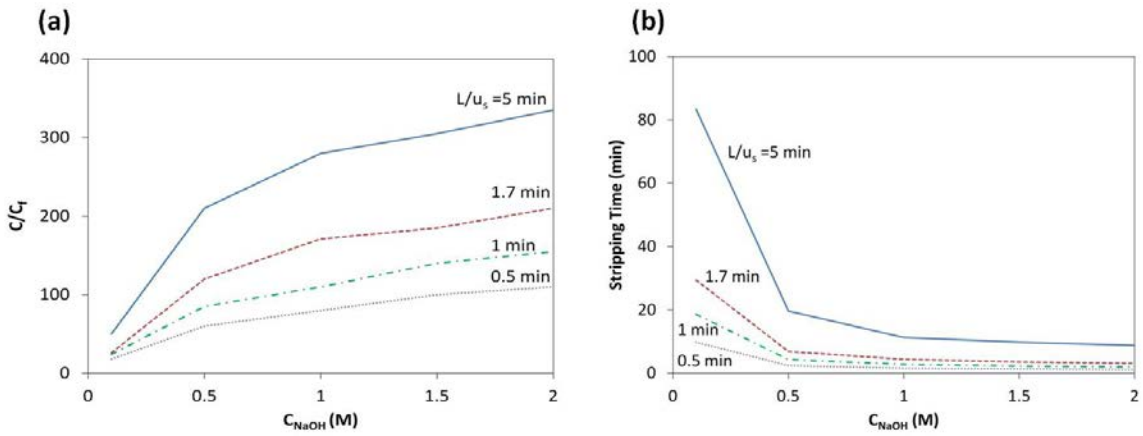

Figure 4.14. Simulated Mo product concentrations (a) and stripping times (b) with different NaOH concentrations and residence times. The CSTR volumes were set 10 % of the column volume. The Mo isotherm parameters were the same as those in the 0.55 M U solution. The stripping agent isotherm parameters were the same as those of NaOH in Table 4.9.

The stripping times as a function of residence time and NaOH concentration are shown in Fig. 4.14b. As expected, a longer residence time leads to a longer stripping time at a fixed NaOH concentration. When NaOH concentration is lower than 0.5 M, the stripping time increases sharply with decreasing NaOH concentration, whereas the stripping time approaches a constant when NaOH concentration exceeds 1 M.

If the stripping time is, for example, required to be less than 20 min, then the stripping should be performed using 1 M NaOH at a residence time of 5 min. Further decrease in residence time does not shorten the stripping time significantly, but drastically lowers the product concentration. Further increase in NaOH concentration has small effect on increasing the product concentration and reducing the stripping time, and it may become highly corrosive to the equipment.

In summary, the experimental and simulation results indicate that NaOH is a more effective stripping agent than NH_4OH. To avoid significant peak spreading due to extra-column mixing, the CSTR dead volume should be kept less than 10% of the column volume. The displacement model predicts that counter-current stripping produces a slightly higher Mo concentration than co-current stripping does. To achieve a short stripping time (<20 min) with a high product concentration, a residence time of 5 min with 1M NaOH concentration is recommended to be used.

4.5 Summary and conclusions

An affinity chromatography process using a titania sorbent was developed for recovering Mo-99 from low-enriched uranium salt solutions. The TiO_2 sorbent has multiple adsorption sites: Brønsted Acid Sites (TiOH), Brønsted Base Sites (Ti-O-Ti),

and Lewis Acid Sites (Ti), and the mechanisms for Mo adsorption and desorption were studied. The loading and stripping processes were properly modeled and simulated. The Mo capture process was designed using the general method based on intrinsic parameters and dimensionless groups (Chapter 3). The minimum column volume, maximum column length, and maximum velocity that satisfy the desired batch size, capture yield, loading time and pressure drop were found rapidly without simulations. Sensitivity analysis can be readily performed to find the safety factor that takes into account possible deviations of material properties and loading conditions from their target values. The designs can be adapted to variations in design criteria, material properties, and feed conditions.

VERSE simulations were used to investigate the adsorption and desorption mechanisms of Mo and to find the desirable conditions for Mo stripping. Simulations which were based on the assumption that the stripping agent adsorbs and acts as a "displacer" can accurately predict the elution time of the Mo peaks. Tailing of the eluted Mo peak in NH_4OH stripping appears to be due to the reaction $NH_4^+ + OH^- \leftrightarrow NH_4OH$. which lowers the effective affinity of OH^- for the sorbent and the concentration of OH^- in the solution. The OH^- is thus unable to favorably displace MoO_4^{2-} from the sorbent, resulting in a diffuse desorption wave of Mo. Such spreading leads to a low Mo product concentration and a long stripping time. Conversely, the Mo peaks stripped by NaOH showed no peak tailing, which suggests that NaOH is a more effective stripping agent than NH_4OH.

Simulations based on the displacement model indicated that the extra-column CSTR dead volume should be kept below 10% of the column volume to avoid significant

dispersion effects of CSTR on the shape of Mo peaks. Counter-current stripping results in a slightly sharper Mo peak than co-current stripping because the migration distance for the Mo peak is shorter. Mo product concentration is higher at a longer residence time for stripping, or a higher NaOH concentration. The latter also decreases the stripping time. In order to achieve a short stripping time (<20 min) with a high product concentration, the residence time is recommended to be 5 min and the NaOH concentration should be 1M.

CHAPTER 5. LIGAND-ASSISTED ELUTION CHROMATOGRAPHY FOR BINARY SEPARATION WITH LINEAR ADSORPTION ISOTHERM

5.1 Introduction

In many liquid chromatography systems, reactions can occur in the mobile phase, resulting in dynamic phenomena different from those in non-reactive systems. Some reactions are desirable and have important applications. For instance, one can analyze the peak areas of the reactants and the products to estimate the rate constants for irreversible reactions (Bolme et al. 1983; LoBrutto et al. 2003) or the reaction stoichiometry and the equilibrium constants for reversible reactions (Grinberg et al. 1989). In a chromatography reactor, if the product peaks for a reversible decomposition reaction are well separated from each other, one can obtain purified products with a higher conversion than the equilibrium conversion in a batch reactor (Wetherold et al. 1974; Cho et al. 1980; Schweich et al. 1982; Hashimoto et al. 1983).

When separating components with similar properties, such as enantiomers and rare earth elements, commercially-available sorbents usually do not have sufficient selectivity. To achieve high-purity and high-yield separation, one can add a ligand, which can react with the solutes to form complexes, into the mobile phase (Ma et al. 2009; Ling and Wang 2014). In some cases, the complexed solutes have substantially different affinities for the sorbent, and thus can be well separated (Owen et al. 1997; Ma et al.

2009). In other cases, the complexed solutes do not adsorb, but the complexation equilibrium constants are significantly different among different solutes. The ligand increases the partition of the preferred solutes in the mobile phase, and thus increases their migration speeds and enables their separation from the less preferred solutes (Rollin et al. 1996; Wang and Ling 2014).

In this study, the dynamic phenomena of ligand-assisted elution chromatography were analyzed. For the sake of simplicity, only binary separations with linear adsorption isotherms were discussed. The first goal was to understand the adsorption and separation mechanisms in such systems. The second goal was to identify the key factors that control the retention and resolution of peaks in elution chromatography. The third goal was to provide general guidelines for designing ligand-assisted elution chromatography systems.

To achieve these goals, we first identified all the independent dimensionless groups from the rate-model equations, which include differential mass-balance equations, boundary conditions, and initial conditions. We then tested the rate model and parameters by comparing simulated chromatograms with experimental data reported by literature. Once the simulation results agreed closely with the data, the models and parameters were validated, and were used to generate chromatograms over a wide range of dimensionless group values. The results were used to identify the key dimensionless groups that control the retention and resolution of solute peaks. Reaction and separation phenomena were analyzed and classified based on the key dimensionless groups. Dynamic column profiles were used to better understand the mechanisms of reactions and separations.

It has been found from this study that the retention and separation of solute peaks highly depend on whether the complexed solutes can adsorb, which can be determined

from the relation between the retention factor and the ligand concentration. If the complexed solutes can adsorb, the overall selectivity approaches the sorbent selectivity for the complexed solutes as ligand concentration increases. High resolution can be achieved at high overall selectivity and low mass transfer resistances. If the complexed solutes do not adsorb, the overall selectivity approaches the ratio of the sorbent selectivity to the ligand selectivity. An additional requirement for achieving high resolution is that the complexation should have comparable strength as the adsorption of free solutes.

5.2 System considered and model testing

Separation of chiral solutes has been widely studied and applied in pharmaceutical industry because enantiomers of many drugs have different physiological effects on living organisms. The separations are always challenging and costly since enantiomers have very similar properties. The system considered in this study were reported by Ma and coworkers (Ma et al. 2009), who attempted to separate two enantiomers of chiral amine hydrochloride salt on C8 and C18 reversed-phase columns by adding sulfated β-cyclodextrin (S-β-CD) as a ligand into the mobile phase. Prior to the injection of enantiomers, the column was pre-equilibrated with the mobile phase containing the ligand, which can form complexes with the enantiomers. The complexed solutes have different affinities for the sorbent. The reaction and adsorption mechanisms are summarized in Fig. 5.1, where L refers to the ligand S-β-CD, R the R-enantiomer, and S the S-enantiomer. LR and LS are the complexed R and S. The complexation and dissociation rate constants are k_+ and k_-, respectively. The ratio k_+/k_- is equal to the complexation equilibrium constant K_C. The adsorption equilibrium constant is K_A.

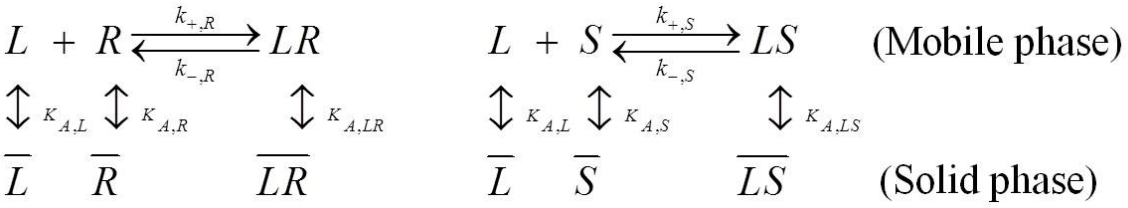

Figure 5.1. Reaction and adsorption mechanisms of ligand-assisted chromatography for separating chiral solutes.

The retention factor, k', was found to be proportional to the overall distribution coefficient, which could be determined from the complexation and the adsorption equilibrium constants (Ma et al. 2009). The final equations are as follows:

$$k_R' = \frac{1}{\varepsilon_t}\left(\frac{K_{A,R} + K_{C,R}K_{A,LR}\,[L]}{1 + K_{C,R}\,[L]}\right) \tag{5.1a}$$

$$k_S' = \frac{1}{\varepsilon_t}\left(\frac{K_{A,S} + K_{C,S}K_{A,LS}\,[L]}{1 + K_{C,S}\,[L]}\right) \tag{5.1b}$$

where ε_t is the total void fraction of the column, and $[L]$ is the ligand concentration, which is constant in each run; $K_{A,R}$ and $K_{A,S}$ are the adsorption equilibrium constants of R and S; $K_{A,LR}$ and $K_{A,LS}$ are the adsorption equilibrium constants of LR and LS; $K_{C,R}$ and $K_{C,S}$ are the complexation equilibrium constants of R and S. Eq. (5.1) applies to HPLC systems with linear adsorption isotherms when complexation and dissociation are at equilibrium.

The retention factors of R and S as a function of the ligand concentration were shown in Fig. 4a of Ma et al. (2009). In the absence of the ligand ($[L]=0$), the retention factors of R and S are the same, indicating that $K_{A,R}=K_{A,S}$, and the sorbent has no selectivity for the solutes. $K_{A,R}$ and $K_{A,S}$ can be calculated from the retention factors k_R' and k_S' by setting $[L]=0$ in Eq. (5.1). The least squares method was then used to find the values of $K_{C,R}$ and $K_{A,LR}$ in Eq. (5.1a), and $K_{C,S}$ and $K_{A,LS}$ in Eq. (5.1b), that can best fit the data of k_R' vs. $[L]$ and k_S' vs. $[L]$, respectively. The obtained equilibrium constants are listed in Table 5.1 and were used in VERSE simulations. Other simulation parameters are listed in Table 5.2. The simulated chromatogram of R/S separation on a C8 column is shown in Fig. 5.2. The peaks have the same widths and retention times as the original data (Fig. 3 of Ma et al. 2009), indicating that the model and the parameters are plausible.

Table 5.1 Adsorption and complexation equilibrium constants

Component	K_A	K_C (mM^{-1})	R^2
R	4.418	-	-
S	4.418	-	-
LR	0.660	86.9	0.998
LS	0.764	95.9	0.999

Table 5.2 Parameters used in VERSE simulations for chiral separations

System Parameters				
L (cm)	ID (cm)	R (μm)	ε_b	ε_p
15	0.46	1.35	0.35	0.25
Operating Conditions				
F (mL/min)		$C_{f,R}$ and $C_{f,S}$ (mM)		t_L (min)
1.5		1		0.01
Reaction Parameters				
Reaction		k_+ ($mM^{-1}min^{-1}$)		k_- (min^{-1})
L+R↔LR		1738		20
L+S↔LS		1918		20
Isotherm Parameters (Langmuir)				
Component		a		b (mM^{-1})
R		4.418		0
S		4.418		0
L		4.418		0
LR		0.66		0
LS		0.764		0
Mass Transfer Parameters				
Component	D_b (cm^2/min)	D_p(cm^2/min)	k_f (cm/min)	E_b (cm^2/min)
All Species	0.001	0.0005	From Wilson and Geankoplis (1966)	From Chung and Wen (1968)
Numerical Parameters				
Axial Elements	Step Size ($L\varepsilon_b/u_s$)	Collocation Points		Tolerance
		Axial	Particle	Absolute (mM)	Relative
100	0.01	4	2	10^{-4}	10^{-4}

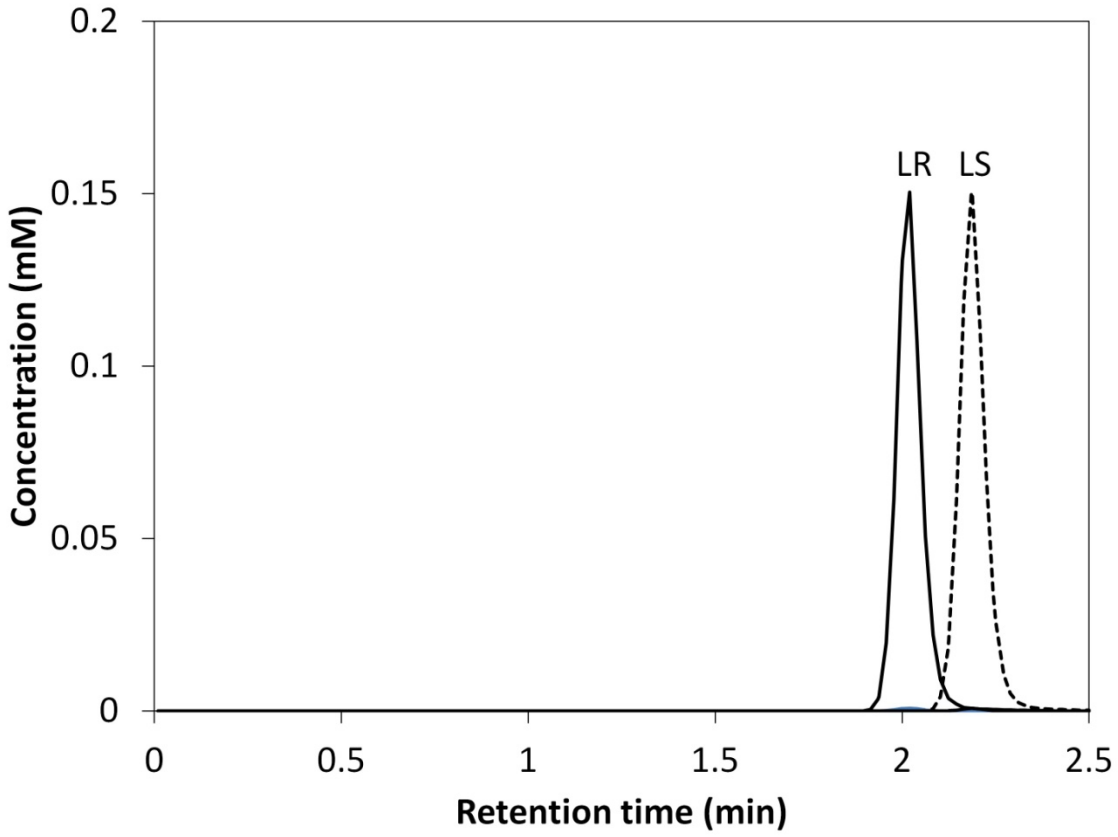

Figure 5.2. Simulated chromatogram for chiral separation. LR is the complexed R-enantiomer, and S is the complexed S-enantiomer. The concentrations of free R and S are negligible. The parameters used in the simulation are listed in Table 5.2.

5.3 Overall selectivity of the system

The overall selectivity α of S over R, in the presence of a mobile-phase additive can be determined from Eq. (5.2).

$$\alpha = \frac{k_S'}{k_R'} = \left(\frac{K_{A,S} + K_{C,S}K_{A,LS}\ [L]}{K_{A,R} + K_{C,R}K_{A,LR}\ [L]} \right) \left(\frac{1 + K_{C,R}\ [L]}{1 + K_{C,S}\ [L]} \right) \tag{5.2}$$

The selectivity depends on the concentration of the ligand [L], the complexation equilibrium constants ($K_{C,R}$ and $K_{C,S}$), and the adsorption equilibrium constants for the complexed solutes and the free solutes ($K_{A,LR}$, $K_{A,LS}$, $K_{A,R}$ and $K_{A,S}$).

If no ligand is present, or [L]=0, α equals sorbent selectivity for the free solutes.

$$\alpha = \frac{K_{A,S}}{K_{A,R}} \tag{5.3}$$

If ligand is present, [L]>0, and the complexed solutes do not adsorb, $K_{A,LR}$=$K_{A,LS}$=0, the overall selectivity in Eq. (5.2) can be simplified as follows:

$$\alpha = \left(\frac{K_{A,S}}{K_{A,R}} \right) \left(\frac{1 + K_{C,R}\ [L]}{1 + K_{C,S}\ [L]} \right) \tag{5.4}$$

If the products $K_{C,R}[L]$ and $K_{C,S}[L]$ are much larger than 1, then the overall selectivity is approximately the ratio of the sorbent selectivity to the ligand selectivity.

$$\alpha \approx \left(\frac{K_{A,S}}{K_{A,R}} \right) \left(\frac{K_{C,R}}{K_{C,S}} \right) \tag{5.5}$$

A high overall selectivity can be obtained if the sorbent and the ligand have opposite relative affinities for the enantiomers. If the sorbent has no selectivity for the free solutes, $K_{A,S}/K_{A,R}$=1, the overall selectivity is determined by the ligand selectivity $K_{C,S}/K_{C,R}$ and the ligand concentration [L].

$$\alpha = \frac{1 + K_{C,R}\,[L]}{1 + K_{C,S}\,[L]} \tag{5.6}$$

For large values of [L], the overall selectivity approaches the value of $K_{C,R}/K_{C,S}$, which is the reciprocal of the ligand selectivity for S.

If [L] >0, and the complexed solutes can adsorb ($K_{A,LR}$, $K_{A,LS}$ >0), the overall selectivity is given by Eq. (5.2). In general, α is a complex function of [L], $K_{A,S}/K_{A,R}$, $K_{C,S}/K_{C,R}$ and $K_{A,LS}/K_{A,LR}$. If [L] is small, the overall selectivity approaches the sorbent selectivity for the free solutes.

$$\alpha \approx \frac{K_{A,S}}{K_{A,R}} \tag{5.7}$$

If [L] is large, then α reduces to

$$\alpha \approx \left(\frac{K_{C,S}K_{A,LS}\,[L]}{K_{C,R}K_{A,LR}\,[L]}\right)\left(\frac{K_{C,R}\,[L]}{K_{C,S}\,[L]}\right) = \frac{K_{A,LS}}{K_{A,LR}} \tag{5.8}$$

Here α is only a function of the sorbent selectivity for the complexed solutes, $K_{A,LS}/K_{A,LR}$. Fig. 5.3 shows α vs. [L] at different values of $K_{C,S}/K_{C,R}$ and $K_{A,LS}/K_{A,LR}$ when the sorbent has no selectivity for the free solutes ($K_{A,S}/K_{A,R}$=1). Graph e with $K_{C,S}/K_{C,R}$ =1.10 and $K_{A,LS}/K_{A,LR}$=1.16 is consistent with the data reported in Ma et al. (2009). The selectivities at [L]=0 mM and [L]=2 mM are consistent with the predictions of Eq. (5.7) and Eq. (5.8).

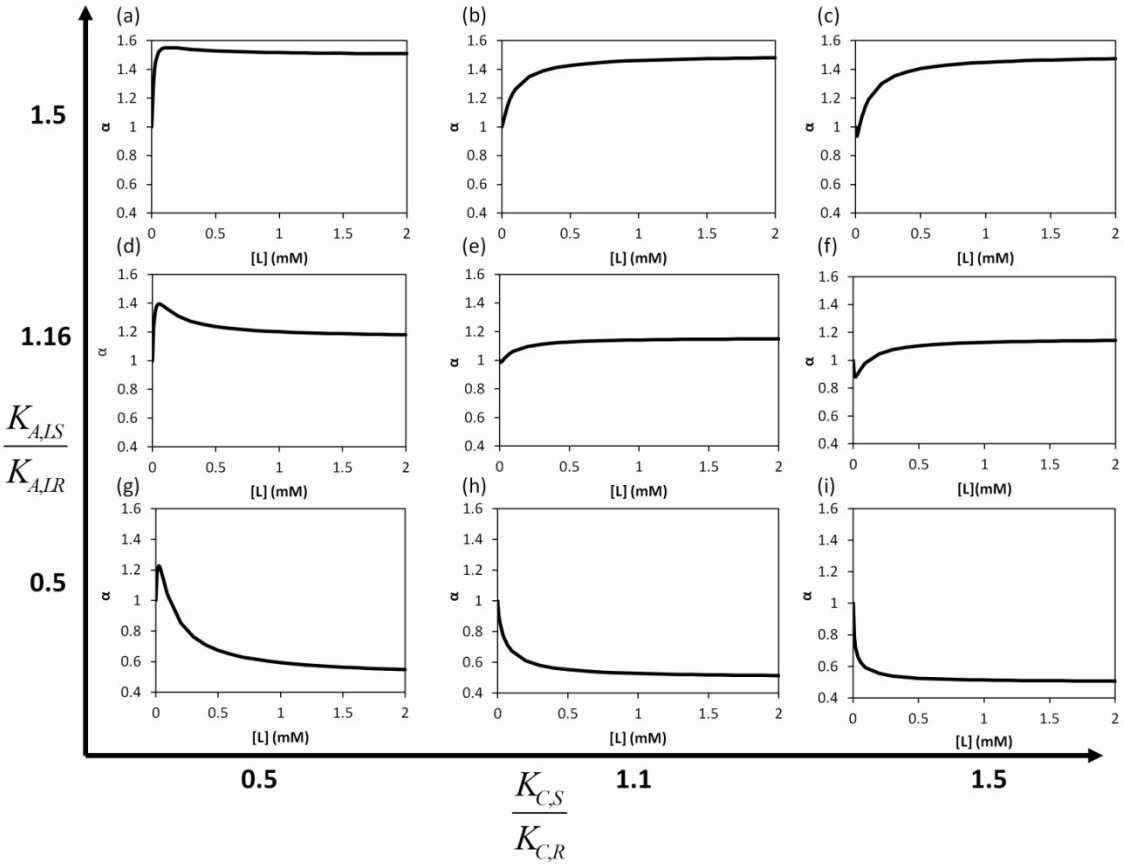

Figure 5.3. Relation of selectivity to ligand concentration at various values of $K_{C,S}/K_{C,R}$ and $K_{A,LS}/K_{A,LR}$. The ratio $K_{A,S}/K_{A,R}$ was assumed to be 1.

Since adsorption of the complexed solutes can affect significantly the overall selectivity, as shown in Eq. (5.2), it is important to determine whether the complexed solutes can adsorb. To achieve this goal, we can rearrange Eq. (5.1) as follows:

$$\frac{1}{k_R'} = \frac{\varepsilon_t(1+K_{C,R}\,[L])}{K_{A,R}+K_{C,R}K_{A,LR}\,[L]} \tag{5.9a}$$

$$\frac{1}{k_S'} = \frac{\varepsilon_t(1+K_{C,S}\,[L])}{K_{A,S}+K_{C,S}K_{A,LS}\,[L]} \tag{5.9b}$$

If the complexed solutes do not adsorb, then $K_{A,LS}$=$K_{A,LR}$=0, the plot of 1/k' vs. [L] is linear. Otherwise, the plot is nonlinear. As shown from the results obtained from Ma et al. (2009), the complexed solutes can adsorb onto the sorbent (Fig. 5.4).

5.4 Improvement of resolution if complexed solutes adsorb

If the complexed solutes can adsorb and the ligand concentration is sufficiently high, the overall selectivity is determined by the sorbent selectivity for the complexed solutes $K_{A,LS}/K_{A,LR}$. High selectivity is necessary but insufficient for achieving high resolution, especially for chromatographic processes coupled with reactions. In this section, we focus on discussing how reaction and mass transfer rates affect the resolution for the system described in Fig. 5.2.

For reactive chromatography systems, the effluent history and column profile are governed by the reaction dimensionless groups (N_{k+} and N_{k-}) as well as the mass transfer dimensionless groups (N_D, Pe_b, and N_f) introduced in Section 3.2.1. N_{k+} and N_{k-} are the complexation rate and the dissociation rate relative to the convection rate, respectively. The definitions of the two dimensionless groups are shown in Eq. (5.10).

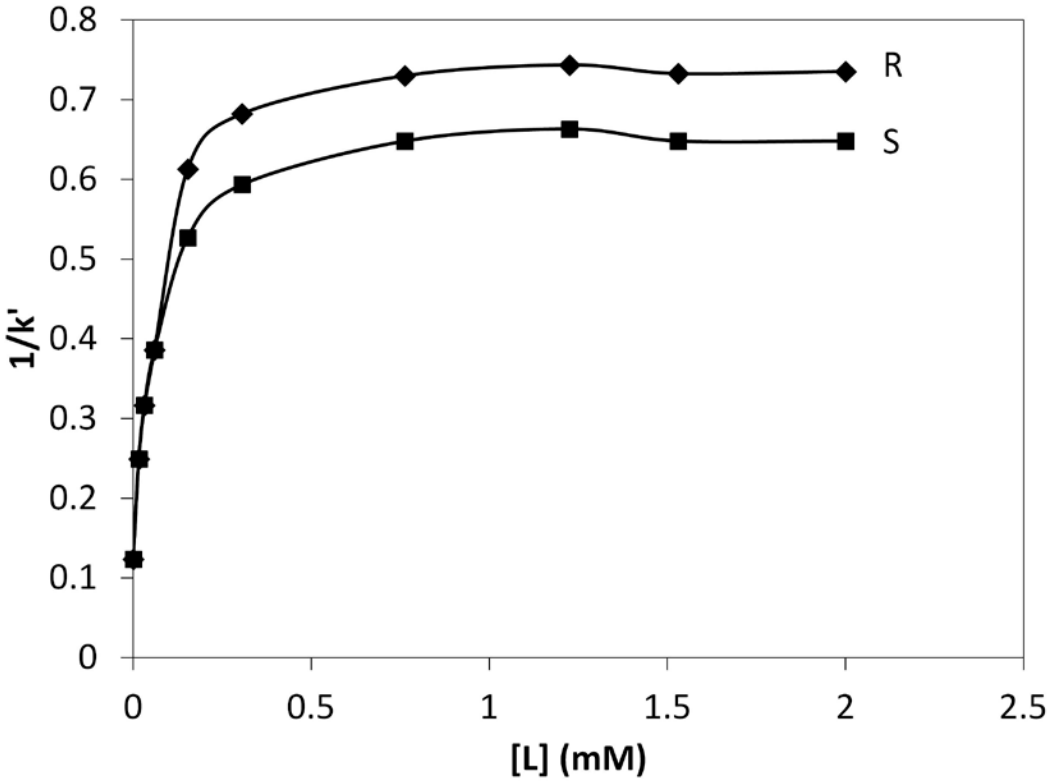

Figure 5.4. Relation between $1/k'$ and ligand concentration. The data points were obtained from Ma et al. (2009).

$$N_{k+} \equiv \frac{Lk_{+}\varepsilon_b[L]}{u_s} \tag{5.10a}$$

$$N_{k-} \equiv \frac{Lk_{-}\varepsilon_b}{u_s} \tag{5.10b}$$

As the relative reaction rates increase, the resolution increases (Fig. 5.5). When the N_{k+} value is small (~10, Fig. 5.5a), the complexation rate is slow, and the time required for the reaction to reach equilibrium is long. As a result, the solutes are primarily in the free forms during migration in the column. Since the sorbent has a high affinity but no selectivity for the free solutes, the two peaks show significant overlap and tailing. When N_{k+} is high (>10^3, Fig. 5.5c-d), the complexation rate is fast, and the complexed solutes are formed immediately after injection. The complexed solutes are eluted separately because a large portion of the column is used for resolving the peaks. The resolution increases with N_{k+} and approaches a constant when $N_{k+,R}$ is greater than 10^3 as shown in Fig. 5.6a. The results indicate that the enantiomers should be dissolved in the ligand solution to allow the complexation and dissociation to reach equilibrium prior to the sample injection, so that the entire column can be used to resolve the solute peaks.

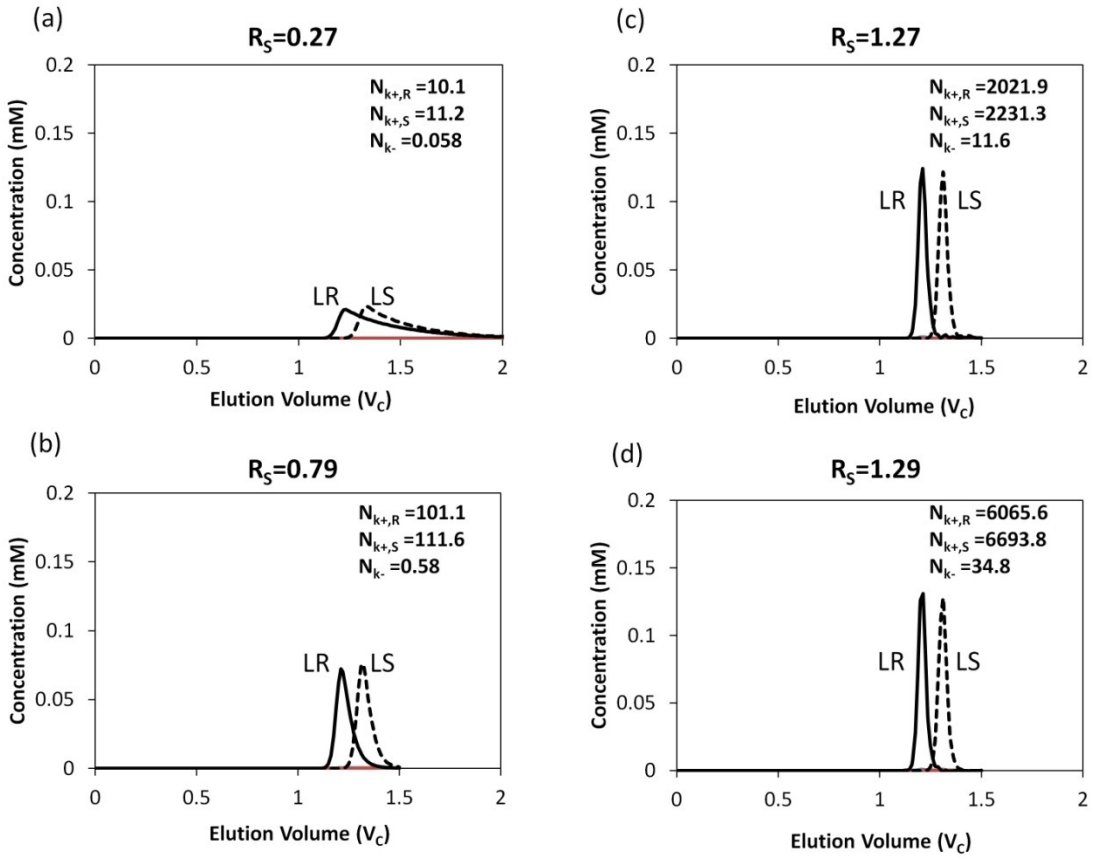

Figure 5.5. Effect of reaction rates on resolution. N_{k+} and N_{k-} are varied by changing k_+ and k_-, while keeping the ratio k_+/k_- constant. The values of N_{k-} for the two reactions are the same. Other parameters are the same as in Figure 5.2.

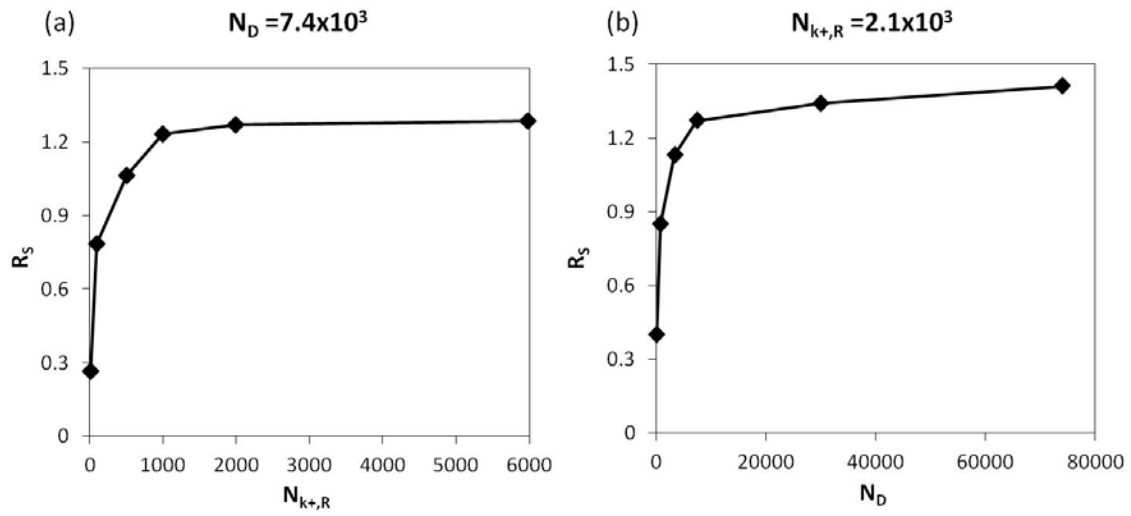

Figure 5.6. Effect of N_{k+} (a) and N_D (b) on resolution. In (a), Pe_b and N_f are the same as in Figure 5.2. In (b), N_{k+} and N_{k-} are the same as in Figure 5.2.

The resolution also increases with decreasing particle size (Fig. 5.7). When R=13.5 μm, (Fig. 5.7a), N_D, Pe_b and N_f are small, resulting in a low resolution. Conversely, when R=1.35 or 0.43 μm (Fig. 5.7c-d), the mass transfer efficiency is high, leading to a high resolution. The resolution increases rapidly with N_D when N_D <10^3, where intra-particle diffusion controls peak spreading (Fig. 5.6b). For N_D larger than 10^3, further gains in resolution are small. Axial dispersion (Pe_b~10^4) and film diffusion (N_f~10^5) also contribute to the peak spreading, but the overall mass transfer effect on the resolution is small.

In summary, to allow the complexation to reach equilibrium soon after sample injection, the value of N_{k+} should be greater than 10^3. To maximize the resolution for the given selectivity, the values of mass transfer dimensionless groups should be in the following range: N_D >10^3, Pe_b >10^4, and N_f >10^4.

5.5 Improvement of resolution if complexed solutes do not adsorb

In some cases, however, the complexed solutes do not adsorb, and the separations arise from the differences in complexation equilibrium constants among different solutes (Rollin et al. 1996; Wang and Ling 2014). As a result, $K_{A,LS}$=$K_{A,LR}$=0, and the retention factor k' in Eq. (5.1) can be reduced to

$$k_R' = \frac{1}{\varepsilon_t} \frac{K_{A,R}}{1 + K_{C,R}\,[L]} \tag{5.11a}$$

$$k_S' = \frac{1}{\varepsilon_t} \frac{K_{A,S}}{1 + K_{C,S}\,[L]} \tag{5.11b}$$

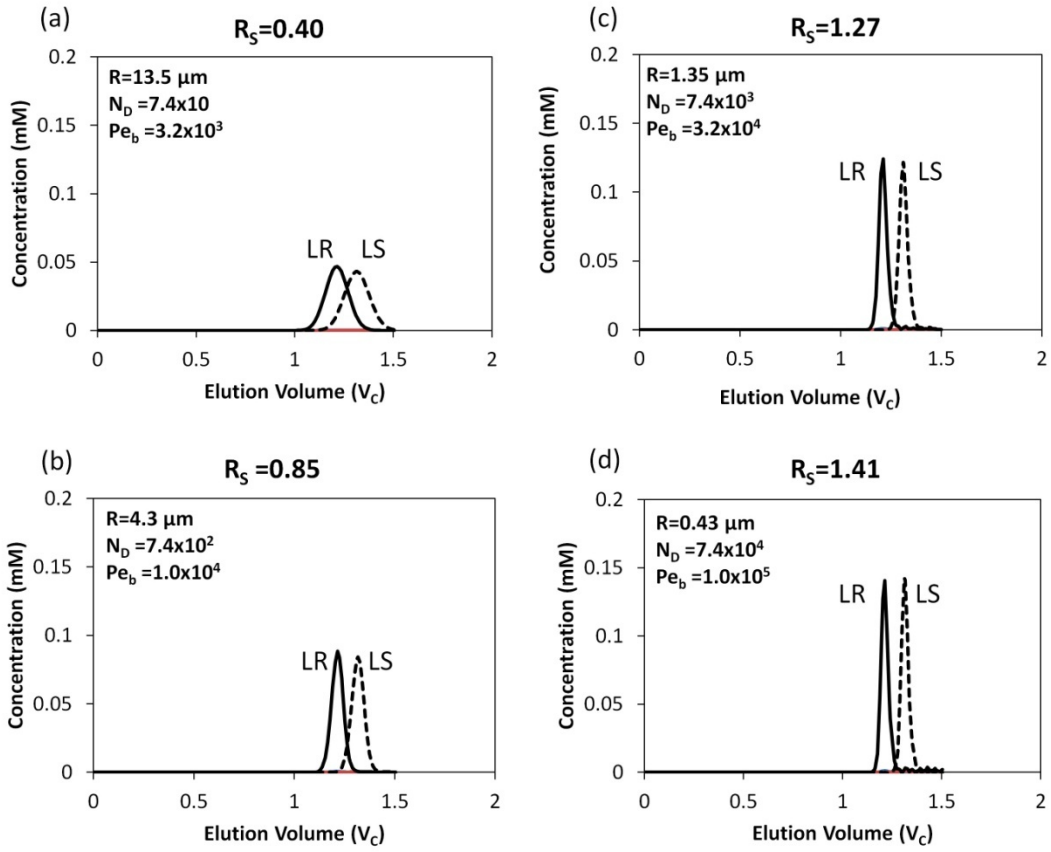

Figure 5.7. Effect of mass transfer resistances on resolution. The particle size is marked in each figure. $N_f = 3.7\times10^4$ (a); 5.5×10^5 (b); 4.7×10^5 (c); 2.5×10^6 (d). Other parameters are the same as in Figure 5.2.

Here R and S refer to two different solutes, not necessarily enantiomers. If the ligand concentration is high, the overall selectivity α is approximately the ratio of the sorbent selectivity to the ligand selectivity, Eq. (5.5). If the sorbent has no selectivity for the free solutes, then α is simply the reciprocal of the ligand selectivity ($K_{C,R}/K_{C,S}$).

In addition to high selectivity, high complexation rates and low mass transfer resistances are also important but still insufficient to guarantee a high resolution. According to Eq. (5.11), if the complexation equilibrium constant K_C or the ligand concentration [L] are large, the product $K_C[L]$ can be much greater than K_A, and the retention factors for both R and S approach zero. Both solutes elute at the total void volume with poor resolution, as shown in Fig. 5.8.

In this example, the sorbent has no selectivity, and the ligand has a selectivity of 2 for S over R. The N_{k+} value is 2.0×10^3 for R and 4.0×10^3 for S, and $N_D = 7.4\times10^3$. Other parameters are the same as those in Table 5.2. The column is pre-equilibrated with the mobile phase containing the ligand, which does not adsorb. When $K_C[L]$ is much larger than $K_{A,R}$ and $K_{A,S}$ (Fig. 5.8a), the values of k_R' and k_S' are less than 0.05 (Table 5.3). The two solutes are eluted close to the total void volume with poor resolution (R_S=0.27). No peak of the free solutes is seen since the solutes bind strongly with the ligand.

As $K_C[L]$ decreases, k_R' and k_S' become larger, and the resolution R_S increases to 0.8 (Fig. 5.8b). When $K_C[L]$ is comparable to the values of $K_{A,R}$ and $K_{A,S}$, the two solutes are well-resolved (R_S=1.63 in Fig 5.8c and R_S=2.13 for Fig. 5.8d). Since complexation rates are fast for R and S, the peaks of R and LR, S and LS, are merged. When $K_C[L]$ is much smaller than $K_{A,R}$ and $K_{A,S}$, the complexation is weak, resulting in longer retention times and broader peaks (Fig. 5.8e). When $K_C[L]$ is much smaller than 1 as shown in Fig

5.8f, the complexation is negligible, and there is little overall selectivity, α(R/S)=1.05 (Table 5.3). Thus, the two solutes co-elute in the free forms with poor resolution (R_S=0.63). To achieve high resolution with minimum peak dilution, a ligand should have a high selectivity (>1.5) and an optimal $K_C[L]$ value, which is of the same order of magnitude as K_A (Table 5.3).

In addition to the value of $K_C[L]$, which equals N_{k+}/N_{k-}, the values of N_{k+} and N_{k-} can also affect peak retention, spreading, and resolution. In Fig. 5.8, the N_{k+} value is fixed at 2×10^3 for R and 4×10^3 for S, and the N_{k-} values are all larger than 10. Under these conditions, the complexation and dissociation reactions are fast, so that the retention times can be predicted from the retention factors of Eq. (5.11), which assumes that the reactions are at equilibrium. Fig. 5.9 shows the peak shapes at different N_{k+} and N_{k-} values. When the reactions are too slow to reach equilibrium (N_{k-}~1, Fig. 5.9a), the complexed solutes tend to elute at the total void volume, whereas the free solutes tend to elute much later (ca. 4.5 V_C). As a result, the peaks of LS and LR are significantly broadened, and the retention times deviate from those given by Eq. (5.11). As N_{k-} increases to 10 (Fig. 5.9b), the peak retention times are consistent with the prediction by Eq. (5.11), but the peaks are spread because of the slow reaction rates. When N_{k-} increases to larger than 10^2 (Fig. 5.9c-d), the spreading due to reactions is reduced, and the resolution is high. In this system, the peak spreading due to the reactions are evident, because N_{k-} values are smaller than those of N_D and Pe_b.

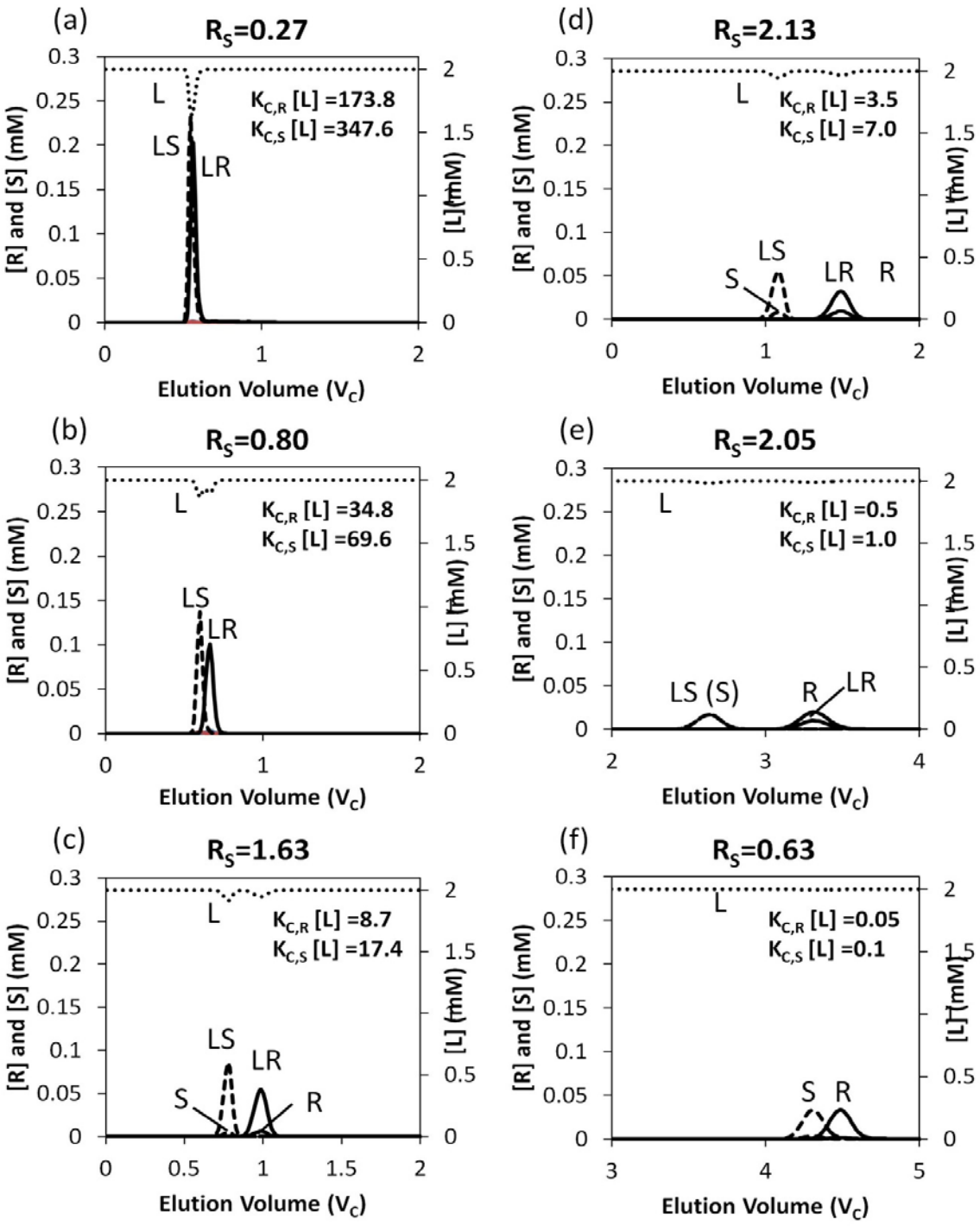

Figure 5.8. Effect of $K_C[L]$ on resolution if the complexed solutes do not adsorb ($K_{A,LR}$= $K_{A,LS}$=0). The sorbent has no selectivity for the free solutes ($K_{A,R}$= $K_{A,S}$=4.418). $K_C[L]$ is varied by changing k_-, whereas k_+ and $[L]$ are kept constant.

Table 5.3 Effects of $K_C[L]$ on retention factor, overall selectivity, and peak resolution if complexed solutes do not adsorb ($K_{A,S}=K_{A,R}=4.418$, $K_{A,LS}=K_{A,LR}=0$, $K_{C,S}/K_{C,R}=2$, $N_{k+}\sim10^3$, $N_{k-}>10$)

Fig. 5.8	$K_{C,R}[L]$	$K_{C,S}[L]$	k_R'	k_S'	α (R/S)	R_S
(a)	173.8	347.6	0.0493	0.0247	2.00	0.27
(b)	34.8	69.6	0.241	0.122	1.98	0.80
(c)	8.7	17.4	0.889	0.469	1.90	1.63
(d)	3.5	7.0	1.92	1.08	1.78	2.13
(e)	0.5	1.0	5.75	4.31	1.33	2.05
(f)	0.05	0.1	8.21	7.84	1.05	0.63

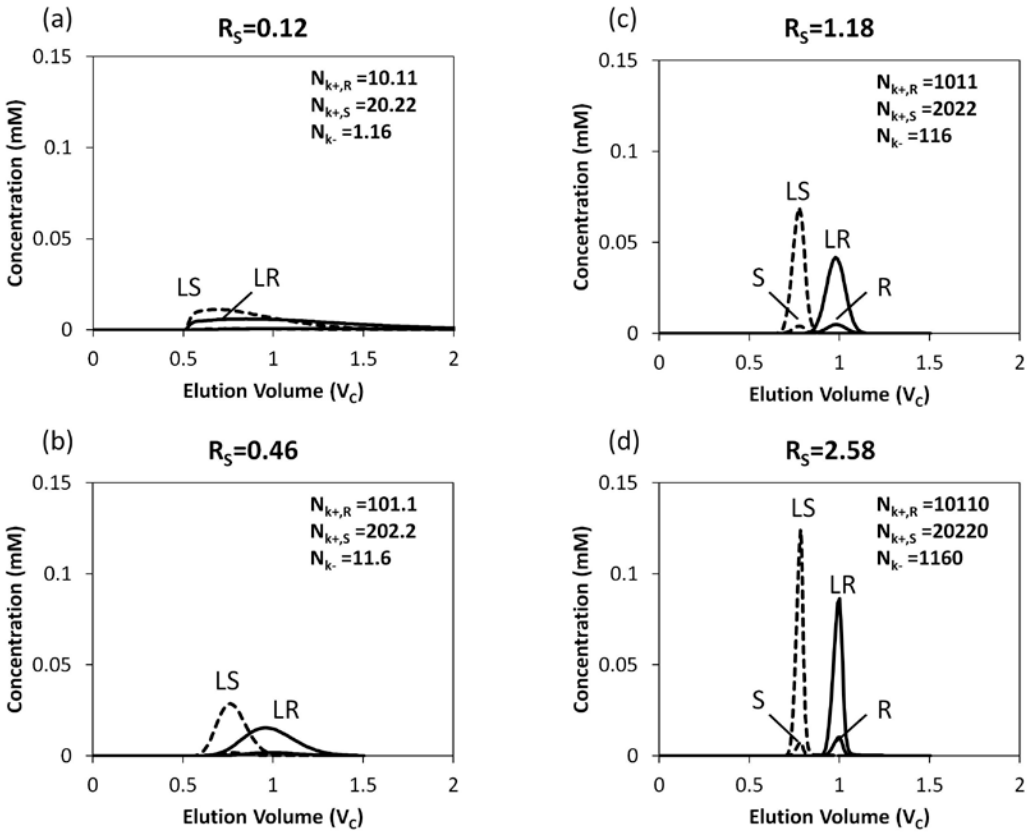

Figure 5.9. Effect of reaction rates on resolution if the complexed solutes do not adsorb ($K_{A,LR}$= $K_{A,LS}$=0). $K_{A,R}$=$K_{A,S}$=4.418, $K_{C,R}[L]$=8.7, and $K_{C,S}[L]$=17.4. N_{k+} and N_{k-} are varied by changing k_+ and k_-. Other parameters are the same as in Figure 5.2.

5.6 Summary and conclusions

Ligand-assisted elution chromatography systems with linear adsorption isotherms have been modeled using VERSE simulations and interpreted with dimensionless groups. The results provided overall guidelines for understanding, designing, and optimizing such chromatography processes. In the case of chiral salts separation using sulfated β-cyclodextrin as the ligand, the complexed solutes can adsorb, which was determined from the highly nonlinear relation between $1/k'$ and ligand concentration [L]. The predicted retention times and peak widths were consistent with the experimental data (Ma et al. 2009). At a high ligand concentration, the selectivity approaches the sorbent selectivity for the complexed solutes, $K_{A,LS}/K_{A,LR}$. At a low ligand concentration, the selectivity is determined jointly by the sorbent selectivity for the free solutes ($K_{A,S}/K_{A,R}$), the ligand selectivity ($K_{C,S}/K_{C,R}$), and the sorbent selectivity for the complexed solutes ($K_{A,LS}/K_{A,LR}$).

If the complexed solutes do not adsorb, the relation between $1/k'$ and [L] is linear. The selectivity increases with the ligand concentration and eventually approaches the ratio of the sorbent selectivity ($K_{A,S}/K_{A,R}$) to the ligand selectivity ($K_{C,S}/K_{C,R}$). If the sorbent has a smaller adsorption equilibrium constant K_A for the solute preferred by the ligand, the sorbent and the ligand can work synergistically for separating the solutes. The value of $K_C[L]$ should be optimized for achieving good resolution. If $K_C[L] >> K_A$, the retention factors are too small, and both solutes co-elute rapidly at the total void volume with a poor resolution. If $K_C[L] <<1$, the retention factors are large, and the overall selectivity approaches the sorbent selectivity, which is generally small. If $K_C[L]$ is of the same order of magnitude as K_A for the free solutes, the solute preferred by the ligand will migrate faster than the other and the two solute peaks will be well-resolved. To avoid

significant peak spreading resulting from the slow reactions, the N_k values should be comparable to those of N_D and Pe_b.

To achieve remarkable separation in the ligand-assisted elution chromatography systems, one should first ensure that the overall selectivity (sorbent selectivity/ligand selectivity) is significantly larger than 1 (>1.5). In addition, the relative reaction and mass transfer rates should be well controlled such that $N_{k+} > 10^3$, $N_D > 10^3$, $Pe_b > 10^4$, and $N_f > 10^4$, and the ligand concentration should be selected to satisfy $K_C[L] \sim K_A$.

CHAPTER 6. LIGAND-ASSISTED ELUTION CHROMATOGRAPHY FOR LANTHANIDES (LN'S) SEPARATION

6.1 Introduction

Lanthanides (Ln's) are rare earth elements, which are critical components of many high-valued products, such as petroleum refining catalysts, phosphors in color television and flat panel displays (cell phones, portable DVDs, and laptops), permanent magnets, and rechargeable batteries for hybrid and electric vehicles (Humphries 2012). Currently, the Ln's used in the U.S. are primarily imported from China, which produces more than 90% of the Ln's used globally (U.S. Department of Energy 2011). Since China has reduced the export quota almost by half since 2010, it is important to develop efficient and cost-effective processes to produce and recover Ln's domestically.

A typical production process for the Ln's involves the following steps (Bril 1964; Wu 1993): (1) physical separations (gravity concentration, flotation, magnetic, or electrostatic separation) which are used to separate rare earth minerals from sands and rocks in the ore; (2) dissolution of rare earth minerals in acidic or caustic solutions; (3) separation of each Ln element from the mixture solutions; (4) precipitation of each Ln element using oxalic acid to obtain solid Ln oxalate, which is then decomposed under heat to form Ln oxide of a single element. Among all the steps, Step 3 is most

challenging and costly because many of the Ln's are present in the solution, and they have very similar chemical properties, ionic sizes, and charges.

The current large-scale purification of Ln's is mainly based on solvent extraction. Almost 20 sequential and parallel extraction steps using organic solvents (naphthenic acid or phosphorous-based extractants) and strong acids (hydrochoric acid or sulfuric acid) are needed to separate the Ln's into eight or ten major fractions (Wu 1993). This method requires large amounts of organic extractants and highly acidic or caustic aqueous solutions. The numerous unit operations require a large footprint, large amounts of solvents, and generate a large amount of environmentally-hazardous wastes..

The feasibility of ligand-assisted displacement chromatography for Ln separation has been reported previously. The Ln's are first loaded onto a cation exchange resin, and then displaced by sodium or ammonium ions in the presence of a ligand. This method using citric acid as the ligand was extensively studied in 1940s-1950s (Spedding et al. 1947; Spedding et al. 1950). However, the productivity of separating Ln's was low and the citrate salts of Ln's were found to precipitate at high pH (>7). After each run, the column has to be regenerated by a concentrated acid solution. In more recent studies, EDTA and other ligands and sorbents were also tested (Spedding and Powell 1959; James et al. 1961; Powell 1964; James et al. 1968; Winget and Lindstrom 1971; Powell and Ling 1985; Moore 2000). To prevent EDTA from precipitation at low pH, the resin cannot be preloaded with H^+ ions, and it has to be preloaded and regenerated by transition metal ions (Spedding and Powell 1959; James et al. 1961; Powell 1964) or heavier Ln ions (Moore 2000). Otherwise, the entire process has to be operated at a high

temperature (90°C) (Winget and Lindstrom 1971). These conditions result in a high separation cost for ligand-assisted displacement chromatography.

Another method for Ln's separation is extraction chromatography, in which a chelating agent is immobilized onto a resin to increase the selectivity of the sorbent for the Ln's. Such resins were developed by Argonne National Laboratory in the 1970's (Horwitz and Bloomquist 1975), and have been tested for analytical applications and small-scale purification (Pin and Zalduegui 1997; Horwitz et al. 2005; Quidelleur et al. 2009). Column test data showed that two small columns (with 0.3 g resin) can be used in tandem to capture and purify six Ln's using two pH elution steps (Pin and Zalduegui 1997). However, the resin is costly and its supply is limited. Recently, Knutson and associates impregnated bis (2-ethylhexyl) phosphoric acid (HDEHP) as the extractant onto C18 columns and used nitric acid as the eluant to separate five Ln's (Knutson et al. 2014). The data were obtained only for HPLC columns. The economical feasibility of using such sorbents for large-scale production still remains an open question.

In this study, we developed a ligand-assisted elution chromatography process for the separation of Ln's using a robust and low-cost inorganic sorbent, titania. The titania column was first preloaded with a ligand. After the Ln's mixture was loaded onto the ligand-immobilized column, a solution of the same ligand was used to elute the adsorbed Ln's. The element that can form a more stable complex with the ligand elutes earlier in the effluent. Theoretical analysis showed that the overall selectivity is approximately the ratio of the ligand selectivity to the sorbent selectivity. In addition, the Ln's can be well separated only if the adsorption isotherm parameters and complexation equilibrium constants are in the same order of magnitude.

Based on the theoretical results, several ligands were screened, among which ethylenediaminetetraacetic acid (EDTA) was found to have the best complexation equilibrium constants for separating the Ln's on a titania column. The separation of a mixture of Pr, Nd, and Sm was obtained under well-designed EDTA concentrations. Linear-gradient elution and step-wise elution were used to concentrate the products and shorten the cycle time. The purity and yield of all three Ln's were above 95%. Rate model simulations taking into account adsorption, mass transfer, and reactions were developed to verify the mechanism of ligand-assisted elution and separation. The simulation results agreed closely with the experimental data.

The separation process developed in this study is much simpler than the conventional sequential and parallel solvent extraction processes. All the Ln's can be separated at room temperature and relatively mild pH conditions. Both the sorbent and the ligand are inexpensive and readily available. The ligand is generally recognized as safe and can be mostly recycled after each run. No harsh or expensive chemicals are needed for column regeneration. To increase sorbent productivity and to reduce the amount of ligand required and the production cost, a continuous counter-current chromatography process with step-wise elution can be developed for large-scale production.

6.2 Mechanism of adsorption, reaction, and separation

6.2.1 Adsorption of Ln's on the titania sorbent

As introduced in Section 4.2.1, titania sorbent has three types of adsorption sites: Brønsted acid (BA), Brønsted base (BB), and Lewis acid (LA) sites. If a ligand

with multiple COO^- groups is preloaded onto a titania sorbent, some of the COO^- groups can bind strongly with the LA sites. Under this condition, the Ln's can adsorb on both the BA sites and the free COO^- groups of the ligand adsorbed on the LA sites. The adsorption data can be correlated using a Bi-Langmuir isotherm model as follows (Lee et al. 2004):

$$q = \frac{a_1 C}{1 + b_1 C} + \frac{a_2 C}{1 + b_2 C} \tag{6.1}$$

where q and C are the solid-phase and the liquid-phase concentrations in local equilibrium; a and b are the linear and nonlinear Langmuir isotherm parameters; subscripts "1" and "2" represent Sites 1 (BA sites) and Sites 2 (LA sites), respectively.

However, if the adsorption sites have much weaker affinity for the Ln's than the ligand in the mobile phase, the sorbent will not be able to retain Ln's in the presence of the ligand. Retention is needed to allow the complexation reactions in the mobile phase to accelerate the migration of the Ln's that have higher affinity for the ligand, resulting in their earlier elution. The effects of adsorption and complexation on Ln separation will be discussed in the next section.

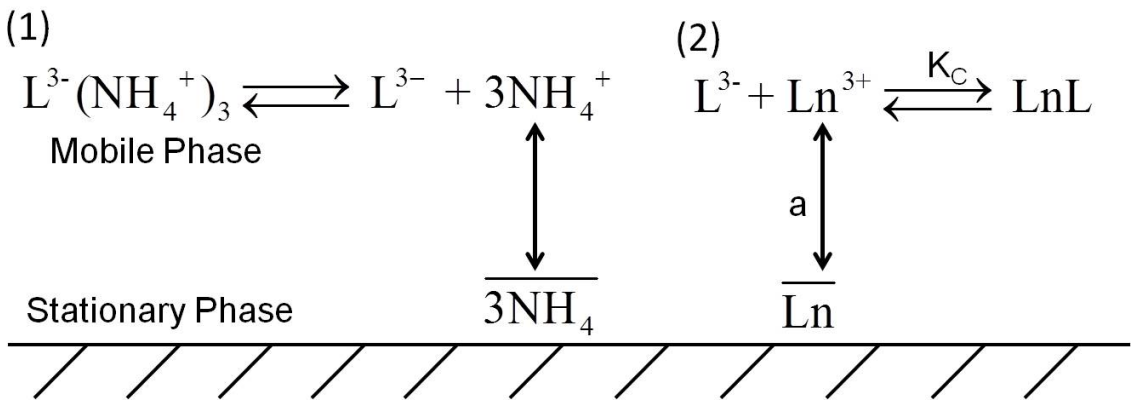

Figure 6.1. Adsorption and complexation of Ln's in the ligand-assisted elution chromatography. L is the ligand, Ln is the lanthanide, LnL is the complex formed by the ligand and the lanthanide. Reaction (1) shows that NH_4^+ is the co-ion of the ligand and it can adsorb onto the sorbent. Reaction (2) shows that lanthanides can form complex with the ligand in the mobile phase and can also adsorb onto the sorbent. K_C is the complexation equilibrium constant, a is the linear Langmuir isotherm parameter.

6.2.2 Ligand-assisted separation of Ln's

In conventional elution chromatography, the migration of solutes along the column results from repetitive adsorption and desorption. In ligand-assisted elution chromatography, the adsorption is strong, and the desorption is driven by a reversible complexation of the solutes and the ligand in the mobile phase (Fig. 6.1). Since different Ln's can form complexes with the ligand with different complexation equilibrium constants, they can migrate at different velocities in the column, resulting in the separation.

It has been shown in Section 5.5 that for a linear isotherm system, if the complexed solutes do not adsorb, the retention factor has the following expression:

$$k' = \frac{1}{\varepsilon_t} \frac{a}{1 + K_C[L]} \tag{6.2}$$

where a is the linear Langmuir isotherm parameter and is equivalent to the "K_A" introduced in Chapter 5. The product $K_C[L]$ can be considered as a dimensionless complexation equilibrium constant. To guarantee a reasonable time scale for elution, $K_C[L]$ must be in the same order of magnitude as a. If $a << K_C[L]$, the complexation reaction is much stronger than the adsorption, resulting in elution of the solutes at the void volume. If $a >> K_C[L]$, the complexation is too weak compared to the adsorption; the solute is likely to be trapped in the column and cannot be eluted.

The ratio of the retention factors of two solutes gives the overall selectivity. In most cases, the complexation is strong and $K_C[L]>>1$, and the overall selectivity is approximately

$$\alpha \approx \left(\frac{a_2}{a_1}\right)\left(\frac{K_{C1}}{K_{C2}}\right) = \frac{\alpha_{Sorbent}}{\alpha_{Ligand}} \tag{6.3}$$

where $\alpha_{Sorbent} = a_2/a_1$ is the sorbent selectivity, and $\alpha_{Ligand} = K_{C2}/K_{C1}$ is the ligand selectivity. If the sorbent has little selectivity for the solutes, the overall selectivity is dominated by the ligand selectivity.

For a nonlinear isotherm system, the retention factor does not have a simple analytical expression. In addition, the co-ion of the ligand, NH_4^+, can also adsorb weakly onto the ligand-loaded LA sites and affect the retention of Ln peaks. Nevertheless, the equations obtained from linear isotherm systems can still serve as guidelines for designing nonlinear isotherm systems. To achieve efficient and high-purity separation, one has to select the ligand such that $K_C[L]$ is comparable to a, and the ratio $\alpha_{Ligand}/\alpha_{Sorbent}$ should be 1.5 or larger.

6.2.3 VERSE simulations for Ln's separation

Although the titania has two types of sites (BA and LA) for Ln adsorption, the BA sites are found to have much weaker affinity for the Ln's than the ligand, and hence have negligible effect on the retention of Ln peaks. This hypothesis has been verified in the simulations, which are not shown here. Therefore, we consider only the high-affinity sites, or the ligand-loaded LA sites, in the simulations, and use the Langmuir adsorption isotherm model instead of the Bi-Langmuir model.

The actual values of K_C, a, and b are large ($>10^7$). If they are used in the simulations, the time required for convergence would be extremely long. In fact, as long as $K_C[L]$ is much greater than 1, the retention of peaks depends primarily on a

dimensionless ratio $a/K_C[L]$, Eq. (6.2), rather than the individual values of *a*, *b*, and K_C. It is expected from dimensionless group analysis and verified using simulations that when the value of $a/K_C[L]$ is fixed, increasing both *a* and $Kc[L]$ does not affect the peak shape or retention time. In order to reduce simulation time, we scale down the values of *a*, *b*, and K_C, while satisfying the following: (1) The ratio K_C(Sm): K_C(Nd): K_C(Pr) is the same as that reported by the literature (Powell 1964); (2) The ratio *a*(Sm): *a*(Nd): *a*(Pr) is the same as the experimental data; (3) The adsorption capacity, or the value of *a/b*, is consistent with the experimental data; (4) The values of $K_C[L]$ are much greater than 1, and they are similar to the Langmuir *a* values.

6.3 Sorbent testing and ligand screening

6.3.1 Displacement test for sorbent testing

The goal of the displacement test was to check if the titania sorbent has sufficiently high selectivity for separating the Ln's. The procedure is described in Section 2.4.1. The chromatogram is shown in Fig. 6.2. Unless otherwise noted, the total volumes shown in the chromatograms of this chapter includes extra-column dead volume (0.13 V_C), total void volume (0.62 V_C), and feed loading volume (0.58 V_C). The sharp change in pH indicates the breakthrough time of the HNO_3 front behind the Sm band.

The bands of Pr and Nd overlapped, indicating that the sorbent has no selectivity for these two elements. The sorbent has higher affinity for Sm than for Pr and Nd, so the band of Sm is behind those of Pr and Nd. However, the bands of Pr and Nd had significant tailing, which severely contaminates the band of Sm. The results indicated that

the selectivity of the titania sorbent is insufficient to separate Ln's with high purity and high yield.

6.3.2 Elution tests for ligand screening

Three ligand candidates, DTPA, EDTA, and citric acid, were tested in elution chromatography processes for Ln's separation. The procedure is described in Section 2.4.2, and the experimental conditions are summarized in Table 6.1. The chromatograms obtained from the elution tests using DTPA and EDTA are shown in Fig. 6.3a and 6.3b, respectively.

When DTPA was used as the ligand, all the Ln's were co-eluted at the void volume. The reason is that DTPA complexed too strongly with the Ln's, which could not adsorb onto the sorbent ($K_C[L] >> a$, see Section 6.2.2). When EDTA was used, the Ln's were eluted separately with a reasonably small retention volume, because EDTA has a high selectivity for the Ln's, and the $K_C[L]$ for the complexation is comparable to the Langmuir a value for Ln's adsorption ($K_C[L] \sim a$). When citric acid was used, none of the Ln's was eluted after 10 column volumes (not shown). The complexation was apparently too weak compared to the adsorption ($K_C[L] << a$), and the Ln's thus strongly adsorbed on the column. To avoid the accumulation of Ln's in the column, concentrated EDTA solution (0.4 M, pH 9) was used as the eluant, and all the Ln's were completely eluted as a single band at the void volume (not shown).

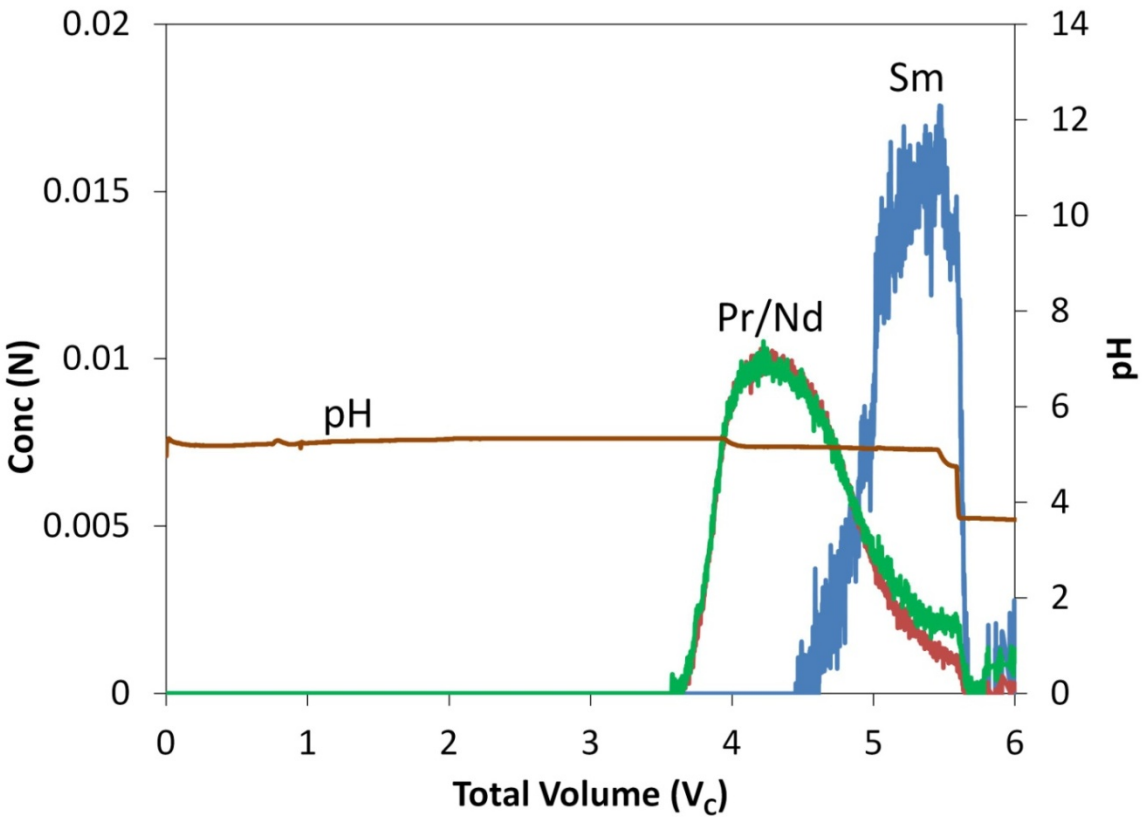

Figure 6.2. Effluent history of Pr, Nd, and Sm in the displacement test using titania. The column size was 49 cm *L* × 1.16 cm *ID*. The superficial velocities for loading and displacement were both 0.2 cm/min. The feed concentration was 0.02 N for each element, and the feed volume was 30 mL or 0.58 V_C. The pH reading can qualitative show the breakthrough of HNO_3 behind the Sm band.

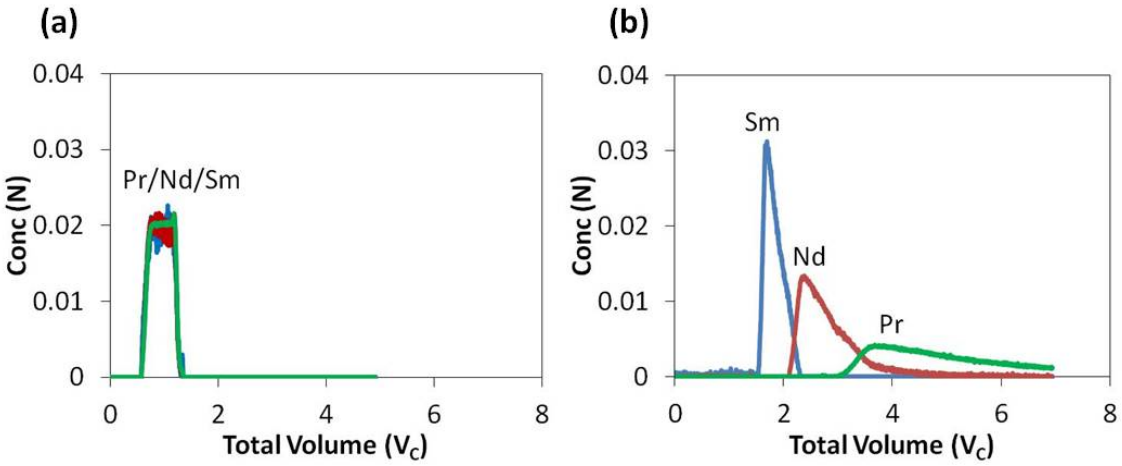

Figure 6.3. Effluent history of Pr, Nd, and Sm for the ligand-assisted elution using 0.04 M DTPA (a) and 0.2 M EDTA (b). The experimental conditions are shown in Table 6.1.

Table 6.1 Experimental conditions for ligand-assisted elution tests

Column size (cm *L* × cm *ID*)	Superficial velocity (cm/min)	Feed concentration (N)	Feed volume (mL)
49 × 1.16	0.2	0.02 for Pr, Nd, Sm	30
Isocratic elution			
Ligand		pH	Presaturant and Eluant Concentration (M)
DTPA		9	0.04
EDTA		9	0.1, 0.2, 0.35, 0.4
Citric acid		7	0.2
Linear gradient elution			
Ligand		pH	Concentration (M)
EDTA		9	0.1-0.4
Step-wise elution			
Ligand		pH	Concentration (M)
EDTA		9	0.15, 0.25, 0.4

6.3.3 Adsorption isotherms of Ln's on the titania sorbent

Since EDTA was found to be the most suitable ligand for Ln's separation on titania, the adsorption isotherms of Ln's on the EDTA-preloaded titania sorbent were investigated. The EDTA-free sorbent was also tested as controls. In the absence of EDTA, the Ln's, if dissolved in DDW, can adsorb weakly on the BA sites of the titania. The pH values of the Ln solutions were around 5. The adsorption isotherms of Nd and Sm are shown in Fig. 6.4a and 6.4b, respectively. The isotherm of Pr was found to be identical as that of Nd, and is not shown separately. The experimental data were correlated closely using the Langmuir isotherm model, and the parameters obtained from the data are listed in Table 6.2.

When the sorbent was preloaded with EDTA (0.4 M, pH 9), the slopes of the isotherm curves and the total capacities for the Ln's increased significantly (Fig. 6.4c and 6.4d), and the data could not be well fitted by the Langmuir model (Table 6.2). The results indicated that the EDTA-preloaded titania has heterogeneous sites for Ln's adsorption. Therefore, the Bi-Langmuir model was found to fit the data better than the Langmuir model (Fig. 6.4e and 6.4f). The parameters showed that one type of adsorption sites has a high affinity but a small capacity for the Ln's, whereas a second type has a low affinity but a large capacity (Table 6.2).

It appears that EDTA adsorbs on the LA sites, and some of the free COO^- groups can serve as additional adsorption sites for the Ln's. Since the interactions between the COO^- groups and the Ln's are strong, the EDTA-loaded LA sites appear to be the high-affinity sites for the Ln's. The BA sites have higher affinity and capacity for the Ln's at pH 9 than at pH 5, but the affinity is still much lower than the EDTA-loaded LA sites.

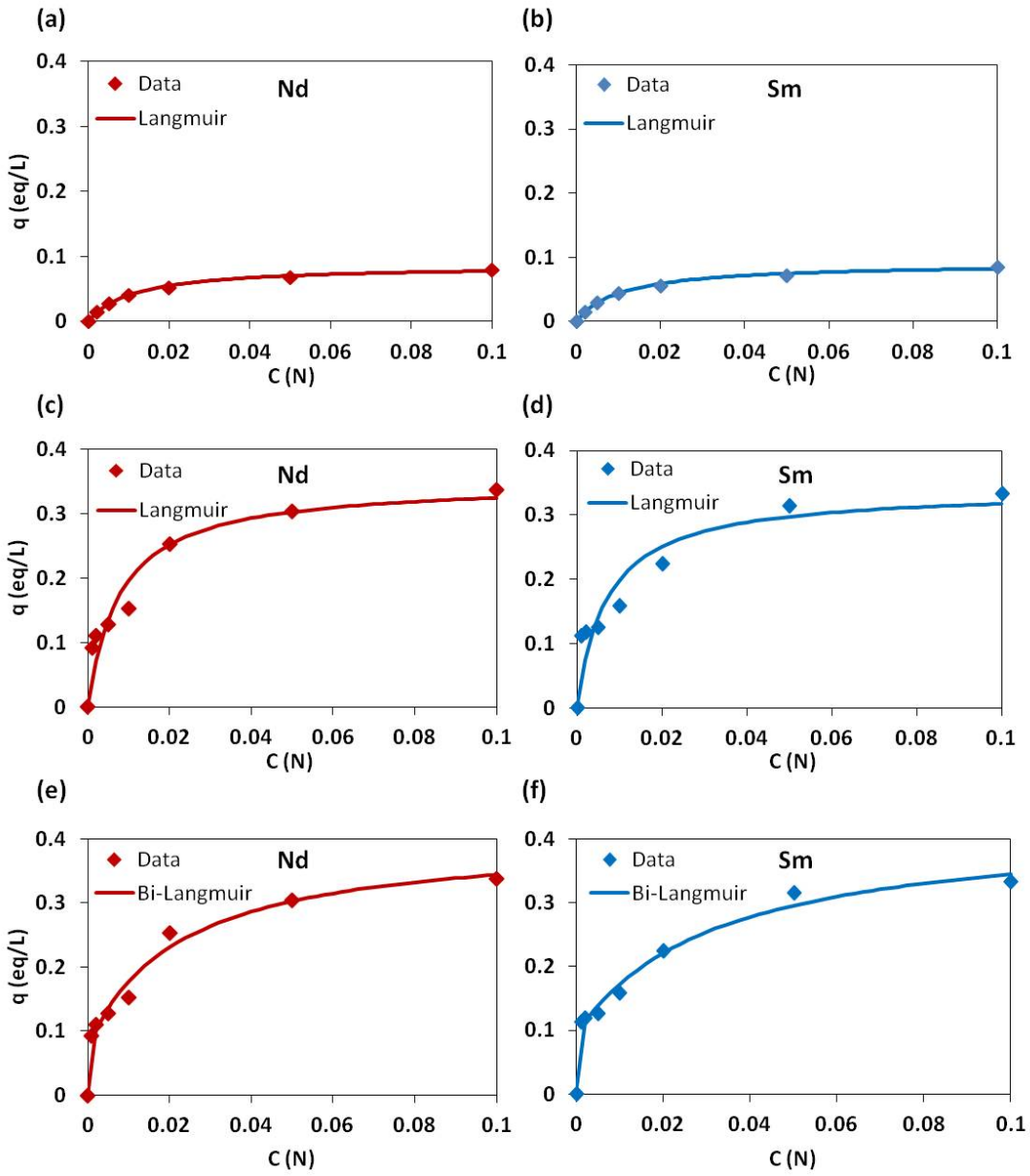

Figure 6.4. Adsorption isotherms for Nd and Sm on EDTA-free (a-b) and EDTA-preloaded (c-f) titania sorbent. The data were obtained from frontal tests. The data points in (c) and (d) are the same as those in (e) and (f), but the fittings were based on different models. In (a)-(d), the data were fitted by the Langmuir model, whereas in (e) and (f), the data were fitted by the Bi-Langmuir model. The isotherm parameters obtained from the fittings are listed in Table 6.2.

Table 6.2 Langmuir and Bi-Langmuir isotherm parameters

Sorbent	Model	Isotherm parameters	Pr/Nd	Sm
EDTA-free titania	Langmuir	a	7.6	8.4
		b (1/N)	88.3	92.4
		R^2	0.995	0.995
EDTA-preloaded titania	Langmuir	a	44.8	47.9
		b (1/N)	128.1	140.9
		R^2	0.920	0.866
	Bi-Langmuir	a_1	14.7	10.7
		b_1 (1/N)	44.7	32.3
		a_2	1.2×10^7	1.9×10^7
		b_2 (1/N)	1.6×10^8	2.4×10^8
		R^2	0.976	0.982

6.4 Isocratic, gradient, and step-wise elution using EDTA for Ln's separation

Since EDTA was found to be the most promising ligand for separating the Ln's on the titania sorbent, it was tested at different concentrations for the elution of the Ln's. The isocratic elution tests were performed at the EDTA concentrations of 0.1 M, 0.2 M, 0.35 M, and 0.4 M, and the results are shown in Fig. 6.5. When the EDTA concentration was low (0.1 M), the Ln peaks were well resolved, but the product concentrations were low and the retention times were long. When the EDTA concentration was high (0.4 M), the product concentrations were high but the resolution was poor.

In order to achieve relatively high product concentrations without sacrificing the purities, linear gradient elution and step-wise elution were tested for separating the Ln's. In linear gradient elution, the EDTA concentration was increased from 0.1 M to 0.4 M linearly over 750 minutes, or from 1.9 V_C to 4.8 V_C in the effluent, Fig. 6.6a. In step-wise elution, the EDTA concentration was increased from 0.15 M to 0.25 and then to 0.4 M, Fig. 6.6b. The total elution times for the two methods were similar to that for the isocratic elution with 0.2 M EDTA, but the product concentrations and the purities of the slow-moving elements (Nd and Pr) were significantly higher. As shown in Table 6.3, the purity and yield for all three elements were 95% or higher for both methods.

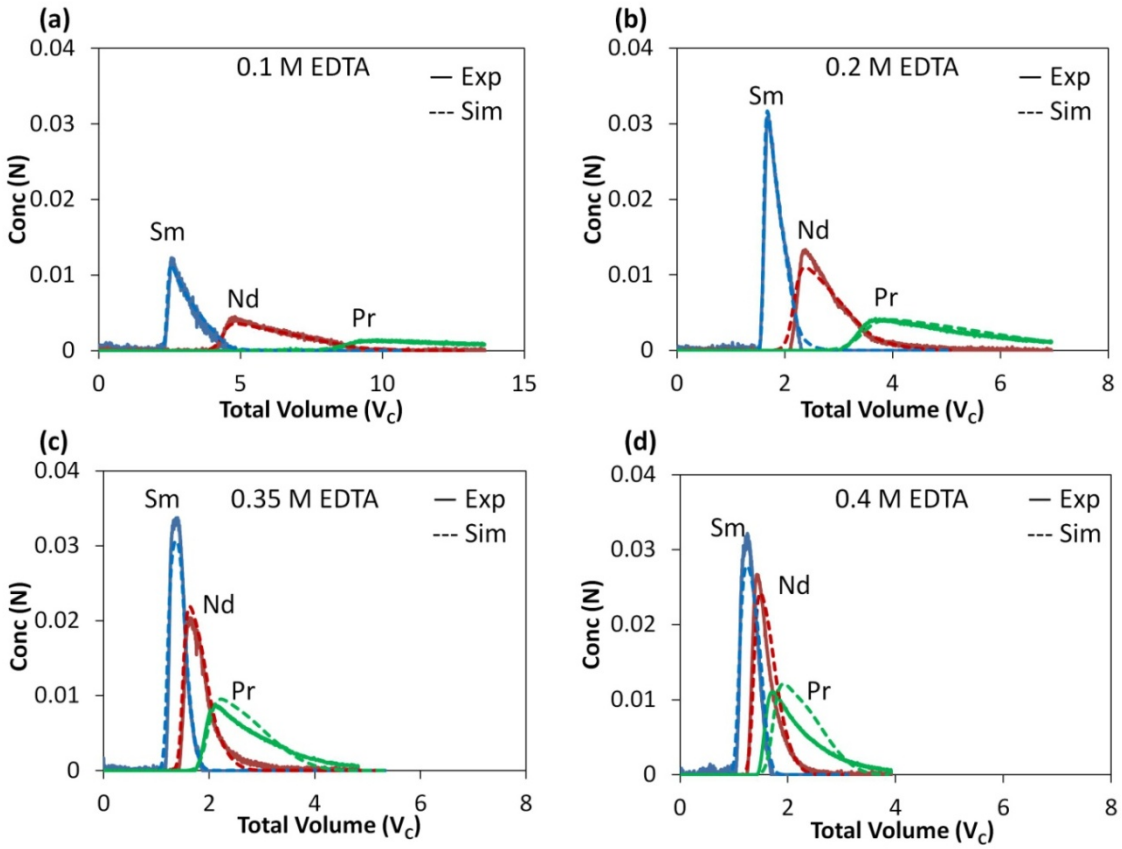

Figure 6.5. Isocratic elution tests for the separation of Pr, Nd, and Sm using EDTA (pH 9) as the ligand. The concentrations of EDTA are shown in each figure. The solid lines were obtained from experiments and the dashed lines were obtained from simulations. The experimental conditions and the parameters used in the simulations are listed in Table 6.1 and Table 6.4, respectively.

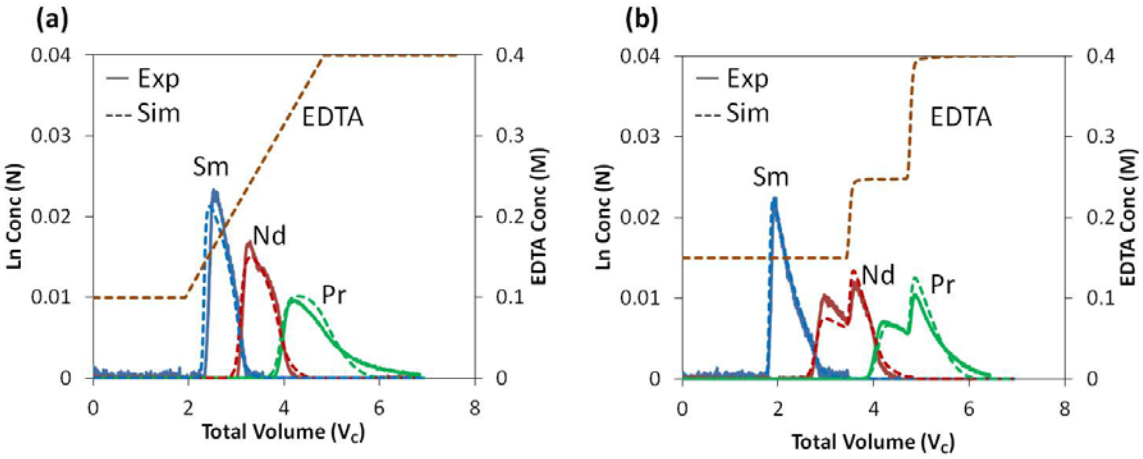

Figure 6.6. Linear gradient elution (a) and step-wise elution (b) for the separation of Pr, Nd, and Sm using EDTA (pH 9) as the ligand. In (a), the EDTA concentration increased from 0.1 M to 0.4 M. In (b), the EDTA concentration increased from 0.1 M to 0.25 M to 0.4 M. The solid lines were obtained from experiments and the dashed lines were obtained from simulations. The experimental conditions and the parameters used in the simulations are listed in Table 6.1 and Table 6.4, respectively. The purities and yields for each component are listed in Table 6.3.

Table 6.3 Purities and yields obtained in the linear gradient elution and step-wise elution

Lanthanide Element	Linear gradient elution		Step-wise elution	
	Purity (%)	Yield (%)	Purity (%)	Yield (%)
Sm	99	97	99	98
Nd	95	96	96	95
Pr	97	96	95	98

The dashed lines in Figs. 6.5 and 6.6 were obtained from VERSE simulations. The models and the assumptions considered in the simulations are explained in Section 6.2.3. Since the affinity of the BA sites for the Ln's is negligible compared to the complexation of EDTA and the Ln's in the solution phase (Table 6.2), only the adsorption on the modified LA sites were considered in the simulations, and the Langmuir isotherm model was used. The parameters used in the simulations are summarized in Table 6.4. The close agreement between the simulations and the experimental data supported the proposed mechanisms and the models.

The step-wise elution process can be operated in a continuous mode to increase the productivity and reduce the cost of Ln's separation. An entire cycle for ternary separation contains three major zones: feeding, elution, and washing (Fig. 6.7a). In the feeding zone, the Ln mixture is loaded onto the column. In the elution zone, different Ln's can be eluted at different EDTA concentrations. In the washing zone, the column is flushed by a diluted EDTA solution. The concentrated EDTA solution in the effluent can be collected and reused. After the washing step, the next cycle will start with the feeding step. Since EDTA has significant selectivity for all adjacent Ln pairs (Table 6.5), it is possible that the ligand-assisted elution process can be developed for the separation of other Ln's.

Table 6.4 Parameters used in VERSE simulations for EDTA-assisted elution on titania

System Parameters				
L (cm)	ID (cm)	R (μm)	ε_b	ε_p
49	1.16	40	0.35	0.4

Reaction Parameters			
Reaction	k_+ ($M^{-1}min^{-1}$)	k_- (min^{-1})	K_C (M^{-1})
Pr+EDTA↔PrEDTA	375	3	125
Nd+EDTA↔NdEDTA	675	3	225
Sm+EDTA↔SmEDTA	2160	3	720

Isotherm Parameters (Langmuir)		
Component	a	b (M^{-1})
Pr	1000	37500
Nd	1000	37500
Sm	1600	60000
NH_4	0.64	8
others	0	0

Mass Transfer Parameters				
Component	D_b (cm^2/min)	D_p (cm^2/min)	E_b (cm^2/min)	k_f (cm/min)
All Species	0.0004	0.00004	From Chung and Wen [19]	From Wilson and Geankoplis [20]

Numerical Parameters					
Axial Elements	Step Size ($L\varepsilon_b/u_s$)	Collocation Points		Tolerance	
		Axial	Particle	Absolute (M)	Relative
50	0.1	4	1	10^{-5}	10^{-4}

Table 6.5 Selectivity of EDTA for adjacent Ln's (Powell 1964)

Ln pairs	α_{EDTA}
Ce-La	3.7
Pr-Ce	2.5
Nd-Pr	1.8
Pm-Nd Sm-Pm	α_{EDTA}(Sm-Nd)=3.2
Eu-Sm	1.5
Gd-Eu	1.05
Tb-Gd	4.2
Dy-Tb	2.3
Ho-Dy	2.6
Er-Ho	1.8
Tm-Er	3.1
Yb-Tm	1.8
Lu-Yb	1.9

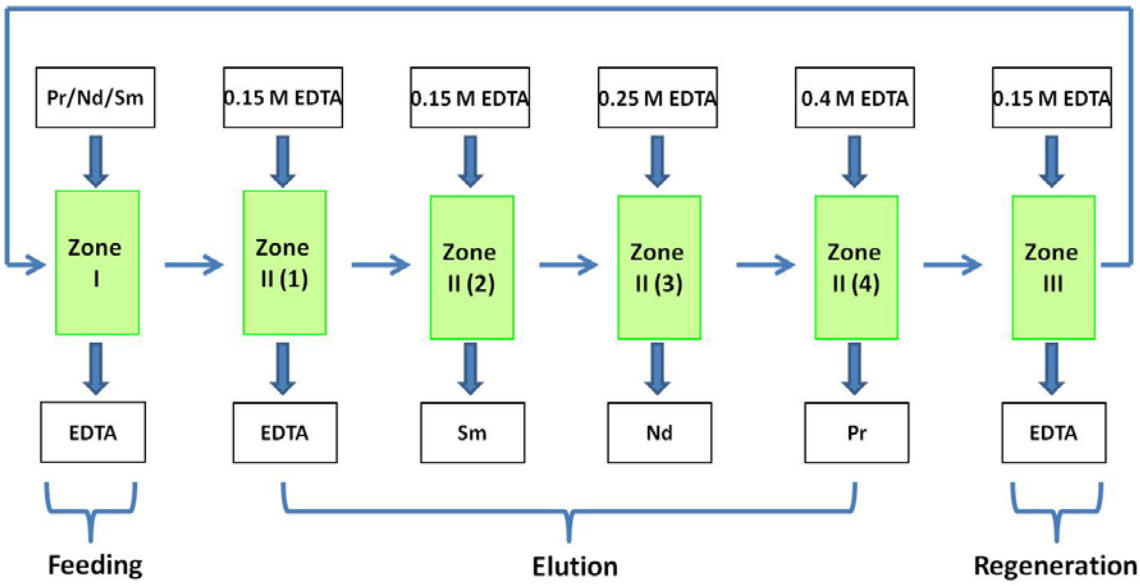

Figure 6.7. Proposed continuous stepwise elution process for the separation of Pr, Nd, and Sm using EDTA (pH 9) as the ligand.

6.5 Summary and conclusions

A ligand-assisted elution chromatography process has been developed for the separation of Ln's. The mechanisms of Ln separation in titania in the presence of a ligand have been proposed. The Ln's can be well separated only if the overall selectivity, which approximates the ratio of the ligand selectivity to the sorbent selectivity, is significantly greater than 1, and the dimensionless complexation equilibrium constant $K_C[L]$ and the Langmuir a value are in the same order of magnitude ($K_C[L]/a \sim 1$).

Based on the theoretical analysis, several ligands have been tested, among which EDTA was found to be the best ligand for separating the Ln's on a titania column. The process was demonstrated by the separation of a mixture of Pr, Nd, and Sm. Pure products of all the elements were obtained under well-designed elution conditions. In order to concentrate the products and shorten the cycle time, linear-gradient elution and step-wise elution were used, and the purity and yield of all three elements were greater than 95%. Rate model simulations taking into account adsorption, mass transfer, and reactions were used to verify the proposed mechanisms and to elucidate the dynamics of ligand-assisted separation. The effluent histories obtained from the simulations agreed closely with the experimental data.

The ligand-assisted elution processes developed in this study have a smaller footprint, require less solvent, and have less environmental impact than the current solvent extraction processes. For large-scale production, economical continuous processes can be developed for Ln's separation to increase sorbent productivity, reduce the amount of ligand, and lower the separation cost.

CHAPTER 7. CONCLUSIONS AND RECOMMENDATIONS

7.1 Conclusions

In this dissertation, we investigated the effects of different variables on chromatography separations based on the analyses of dimensionless groups, and developed systematic methods for designing LC processes for capture and purification.

In Chapter 3, a general method was developed for designing the capture step of affinity chromatography. This method is based on intrinsic parameters and dimensionless groups, which reduce the complex design space into two dimension. For Langmuir isotherm systems, if material properties and feed conditions are known, the minimum column volume and the maximum operating velocity governed by yield, loading time, and pressure drop requirements can be determined readily without additional experiments or simulations. If the design requirements or material properties are varied, their effects on the column volume can be shown graphically, and the new solution can be found rapidly. This method has been verified by a wide variety of literature data for antibody purification, and is applicable to different capture systems and production scales.

In Chapter 4, an affinity chromatography process was developed for Mo-99 recovery from uranium fission products. The design of TiO_2-packed columns for Mo capture was based on the general method we describe in Chapter 3. The required column

volume, diameter, and operating velocity were found for production scale processes. The desirable conditions for Mo stripping were found using VERSE simulations, which were based on the experimentally-determined capacities of the various adsorption sites and the understandings of Mo adsorption and desorption mechanisms. The results indicated that NaOH is a more efficient stripping agent than NH_4OH, because the latter has the reaction of $NH_4^+ + OH^- \leftrightarrow NH_4OH$, which reduces the OH^- concentration in the solution, and the effective affinity of OH^- for the sorbent. The extra-column CSTR dead volume should be less than 10% of the column volume, and the counter-current stripping is advantageous over the co-current stripping. The optimal conditions for achieving a short stripping time (<20 min) and a high product concentration are: L/u_s =5 min and C_{NaOH} = 1 M.

In Chapter 5, the mechanisms of reactions and separations in ligand-assisted chromatography systems were elucidated. The key dimensionless groups that control the performance for multi-component purification were identified. If the complexed solutes adsorb, the overall selectivity approaches the sorbent selectivity for the complexed solutes, $K_{A,LS}/K_{A,LR}$, in the presence of a concentrated ligand. A high overall selectivity and high dimensionless mass transfer rates (N_D, Pe_b, N_f) are needed for obtaining well-resolved peaks. If the complexed solutes do not adsorb, the overall selectivity approaches the ratio of the sorbent selectivity ($K_{A,S}/K_{A,R}$) to the ligand selectivity ($K_{C,S}/K_{C,R}$). An additional requirement for achieving good separation is that complexation and adsorption should have comparable strengths ($K_C[L]$~K_A).

In Chapter 6, ligand-assisted elution chromatography processes were developed for the separation of lanthanides (Ln's) using a robust TiO_2 sorbent. EDTA was found to be the best ligand because it allows the system to have a high overall selectivity and

similar strengths of complexation and adsorption. Ternary separations of Pr, Nd, and Sm were tested. The purity and yield of all three elements were greater than 95% when linear-gradient elution or step-wise elution was used. VERSE simulations were carried out for the ligand-assisted separation processes, and the results agreed closely with the experimental data. Compared to the existing solvent extraction processes, the ligand-assisted elution chromatography processes require a smaller footprint and less solvent, and is more environmentally friendly. For large-scale production, the processes can be operated in a continuous mode to increase sorbent productivity, reduce the amount of ligand, and lower the separation cost.

7.2 Recommendations

In this dissertation, we focused on discussing how to design affinity capture processes for single-component recovery, and how to develop ligand-assisted elution processes for multi-component purification. Both capture and purification are batch processes. In the future, we recommend to investigate the effects of other components on capture, the effects of pH and feed concentration on purification, and the technical and economical feasibility of developing the capture and purification processes into continuous modes.

In the design of affinity capture, we assumed that there is only one target solute, and all the impurities are non-adsorbing components. However, if some of the impurities can compete with the target solute for the adsorption sites, or more than one target solute need to be captured by the sorbent, the current design method cannot be directly used. It

is desirable to develop a more general design method which can take into account the effects of other competing species on the capture of target solute(s).

For batch capture processes, the column utilization can never reach 100% without significant yield loss. One way to break this limit is to employ continuous capture processes by using, for example, three columns in a row. The first column is fully utilized to capture the feed solution; the second column is used to retain the spread wave front; the third column is undergoing stripping and regeneration. The inlet and outlet ports are moving around the three columns periodically. In this manner, the columns can be fully utilized so that the sorbent productivity is high. A systematic method for designing such processes to meet throughput and pressure drop requirements will be highly favorable.

For ligand-assisted elution processes, we tested ternary separations at a fixed pH with varied ligand concentrations. Another way to perform gradient or step-wise elution is to fix the ligand concentration but varying pH, which is recommended to be studied in the follow-up research. The effects of feed concentration and feed composition on the purity and yield may also need to be deeply investigated. In addition, although only separations of three Ln's are tested and modeled in this dissertation, we believe the processes we develop can be tailored for separating other critical Ln's or other similar species, such as actinides. The proof of the versatility of the processes is important.

In the last part of Chapter 6, we proposed a continuous step-wise elution process which has the potential to increase sorbent productivity and reduce the ligand consumption. It is highly recommended to experimentally verify this process, and compare the total costs with those of the existing solvent extraction processes.

BIBLIOGRAPHY

BIBLIOGRAPHY

AbSoluteTM by Novasep: High performance protein A media for the capture of monoclonal and polyclonal antibodies, Product data profile, http://www.novasep.com/Upload/pdf/Datasheet-Absolute-Protein-A.pdf.

Antia, F. D., C. Horvath, Gradient elution in non-linear preparative liquid chromatography, J. Chromatogr. 484 (1989) 1.

Ball, R. M., Medical Isotope Production Reactor, U.S. Patent No. 5,596,611 (1997).

Berninger, J. A., R. D. Whitley, X. Zhang, N.-H. L. Wang, A versatile model for simulation of reaction and nonequilibrium dynamics in multicomponent fixed-Bed adsorption processes, Comput. Chem. Eng. 15 (1991) 749.

Bolme, M. W., S. H. Langer, The liquid chromatographic reactor for kinetic studies, J. Phys. Chem. 87 (1983), 3363.

Bril, K. J., Mass extraction and separation, Progress in the Science and Technology of the Rare Earths, Vol.1, Macmillian, New York, 1964.

Carta, G., Predicting protein dynamic binding capacity from batch adsorption tests, Biotechnol. J. 7 (2012) 1216.

Chuen, C., S. Parrish, W. C. Potter, E. Sokova, HEU Minimization: The Technical-Political Nexus, Proceedings of the International Meeting on Reduced Enrichment for Research and Test Reactors, September-October, 2006, Cape Town, South Africa.

Chung, S. F., C. Y. Wen, Longitudinal dispersion of liquid flowing through fixed and fluidized beds, AIChE J. 14 (1968) 857.

Chung, P., J. G. Bugayong, C. Chin, N.-H. L. Wang, A parallel pore and surface diffusion model for predicting the adsorption and elution profiles of lispro insulin and two impurities in gradient-elution reversed phase chromatography, J. Chromatogr. A. 1217 (2010) 8103.

Cho, B., R. Carr, R. Aris, A continuous chromatographic reactor, Chem. Eng. Sci. 35 (1980) 74.

Cooney, D. O., E. N. Lightfoot, Existence of asymptotic solutions to fixed-bed separations and exchange equations, Ind. Eng. Chem. Fundam. 4 (1965) 233.

Crittenden, J. C., P. S. Reddy, H. Arora, J. Trynoski, D. W. Hand, D. L. Perram, R. S. Summers, Predicting GAC performance with rapid small-scale column tests, J. Am. Water Works Assoc. 83 (1991) 77.

Cuatrecasas, P. C., B. Anfinsen, Affinity chromatography, Annu. Rev. Biochem. 40 (1971) 259.

Cussler, E. L., Diffusion: Mass Transfer in Fluid Systems, Cambridge University Press, London, UK, 1984.

Garcia A. A., M. R. Bonen, J. Ramirez-Vick, M. Sadaka, A. Vuppu, Bioseparation Process Science, Blackwell Science, Inc., Malden, MA, 1999.

Garg, D. R., D. M. Ruthven, Linear driving force approximations for diffusion controlled adsorption in molecular sieve columns, AIChE J. 21 (1975) 200.

Glenn, D. E., Method and Apparatus for the Extraction and Processing of Molybdenum-99, U.S. Patent No. 0206,579 (2011).

Grinberg, N., R. Blanco, D. M. Yarmush, B. L. Karger, Protein aggregation in high-performance liquid chromatography: hydrophobic interaction chromatography of beta-lactoglobulin A, Anal. Chem. 61 (1989) 514.

Hashimoto, K., S. Adachi, H. Noujima, Y. Ueda, A new process combining adsorption and enzyme reaction for producing higher-fructose syrup, Biotechnol. Bioeng. 25 (1983) 2371.

Hober, S., K. Nord, M. Linhult, Protein A chromatography for antibody purification, J. Chromatogr. B. 848 (2007) 40.

Horwitz, E. P., C. A. A. Bloomquist, Chemical separations for super-heavy element searches in irradiated uranium targets, J. Inorg. Nucl. Chem. 37 (1975) 425.

Horwitz, E. P., D. R. McAlister, A. H. Bond, and R. E. Barrans, Jr., Novel extraction chromatographic resins based on tetraalkyldiglycolamides: Characterization and potential applications, Solvent Extr. Ion Exch. 23 (2005) 219.

Hritzko, B. J., D. Walker, N.-H. L. Wang, Design of a carousel process for cesium removal using crystalline silicotitanate, AIChE J. 46 (2000) 552.

Humphries, M., Rare Earth Elements: The Global Supply Chain, Congressional Research Service Report, 2012.

James, D. B., J. E. Powell, F. H. Spedding, Cation-exchange elution sequences-I Divalent and rare-earth cations with EDTA, HEDTA and citrate, J. Inorg. Nucl. Chem. 19 (1961) 133.

James, D. B., J. E. Powell, H. R. Burkholder, Displacement ion-exchange separation of ternary rare earth mixtures with chelating eluants, J. Chromatog. 35 (1968) 423.

Jenkins, I. L., Ion exchange in the atomic energy industry with particular reference to actinide and fission product separations-A review, Hydrometallurgy 5 (1979) 1.

Katoh, S., M. Imada, N. Takeda, T. Katsuda, H. Miyahara, M. Inoue, S. Nakamura, Optimization of silica-based media for antibody purification by protein A affinity chromatography, J. Chromatogr. A. 1161 (2007) 36.

Knutson, H-K., M. Max-Hansen, C. Jonsson, N. Bog, B. Nilsson, Experimental productivity rate optimization of rare earth element separation through preparative solid phase extraction chromatography, J. Chromatogr. A. 1348 (2014) 47.

Lee, H.-J., Y. Xie, Y.-M. Koo, and N.-H. L. Wang, Separation of lactic acid from acetic acid using a four-zone SMB, Biotechnol. Progr. 20 (2004) 179.

Ling, L., P. Chung, A. Youker, D. Stepinski, G. F. Vandegrift, N.-H. L. Wang, Capture chromatography for Mo-99 recovery from uranyl sulfate solutions: Minimum-column-volume design method, J. Chromatogr. A. 1309 (2013) 1.

Ling, L., N.-H. L. Wang, Analysis of dynamic phenomena in liquid chromatography systems with reactions in the mobile phase, Advances in Chromatography Series, Vol 52, CRC Press, Taylor and Francis, Boca Raton, FL, 2014.

Ling, L., L. Kao, N.-H. L. Wang, A new general method for designing affinity chromatography processes, J. Chromatogr. A. 1355 (2014) 86.

LoBrutto, R., Y. Bereznitski, T. J. Novak, L. DiMichele, L. Pan, M. Journet, J. Kowal, N. Grinberg, Kinetic analysis and subambient temperature on-line on-column derivatization of an active aldehyde, J. Chromatogr. A. 995 (2003) 67.

Lowe, J. T., W. H. Hale, D. F. Hallman, Development of a pressurized cation exchange chromatographic process for separation of transplutonium actinides, Ind. Eng. Chem. Process Des. Develop. 10 (1971) 131.

Ma, S., S. Shen, N. Haddad, W. Tang, J. Wang, H. Lee, N. Yee, C. Senanayake, N. Grinberg, Chromatographic and spectroscopic studies on the chiral recognition of sulfated beta-cyclodextrin as chiral mobile phase additive enantiomeric separation of a chiral amine, J. Chromatogr. A. 1216 (2009) 1232.

Marcus, Y., Ion Properties, Marcel Dekker, Inc., New York, 1997.

McNeff, C., B. Yan, J. Winkler, Polymer Coated Titania for Analytical and Preparative Reversed-Phase Chromatography, PITTCON 2005 (56th Pittsburgh Conference on Analytical Chemistry and Applied Spectroscopy), February 26 - March 4, 2005, Orlando, FL.

Michaels, A. S., Simplified method of interpreting kinetic data in fixed-bed ion exchange, Ind. Eng. Chem. Res. 44 (1952) 1922.

Miyahara, H., R. Nakashima, M. Inoue, T. Katsuda, H. Yamaji, S. Katoh, Optimization and performance of silica-based media for industrial-scale antibody purification, Chem. Eng. Technol. 35 (2012) 157.

Montgomery, D. C., E. A. Peck, G. G. Vining, Introduction to Linear Regression Analysis (5th edition), Wiley, New York, 2012.

Moore, B. W., Selective separation of rare earth elements by ion exchange in an iminodiacetic resin, U.S. Patent No. 6,093,376 (2000).

Moreno-Pirajan, J. C., D. Rangel, B. Amaya, E. M. Vargas, L. Giraldo, Design and construction of equipment to make adsorption at pilot plant scale of heavy metals, Z. Naturforsch., A: Phys. Sci. 63 (2008) 453.

Murphy, J. C., D. L. Jewell, K. I. White, G. E. Fox, R. C. Wilson, Nucleic acid separations utilizing immobilized metal affinity chromatography, Biotechnol Prog. 19 (2003) 982.

Naja, G., B. Volesky, Behavior of the mass transfer zone in a biosorption column, Environ. Sci. Technol. 40 (2006) 3996.

Ng, C. K., H. Osuna-Sachez, E. Valery, E. Sorensen, D. G. Bracewell, Design of high productivity antibody capture by protein A chromatography using an integrated experimental and modeling approach, J. Chromatogr. B. 899 (2012) 116.

Owens, P. K., A. F. Fell, M. W. Coleman, J. C. Berridge, Chiral recognition in liquid chromatography utilising chargeable cyclodextrins for resolution of doxazosin enantiomers, Chirality 9 (1997) 184.

Perez-Almodovar, E. X., G. Carta, IgG adsorption on a new protein A sorbent based on macroporous hydrophilic polymers II. Pressure – flow curves and optimization for capture, J. Chromatogr. A. 1216 (2009) 8348.

Perez-Almodovar, E. X., G. Carta, IgG adsorption on a new protein A sorbent based on macroporous hydrophilic polymers I. Adsorption equilibrium and kinetics, J. Chromatogr. A. 1216 (2009) 8339.

Piefer, G., Device and Method for Producing Medical Isotopes, U.S. Patent No. 0096,887 (2011).

Pin, C., J. F. S. Zalduegui, Sequential separation of light rare-earth elements, thorium and uranium by miniaturized extraction chromatography: Application to isotopic analyses of silicate rocks, Analytica Chimica Acta, 339 (1997) 79.

Porath, J., J. Carlsson, I. Olsson, G. Belfrage, Metal chelate affinity chromatography, a new approach to protein fractionation, Nature 258 (1975) 598.

Powell, J. E., The separation of rare earths by ion exchange, Progress in the Science and Technology of the Rare Earths, Vol.1, Macmillian, New York, 1964.

Powell, J. E., D. R. Ling, On altering the lanthanide chelate formation constant sequence to improve Am^{3+}-Ln^{3+} separations in cation-exchange elutions, Inorg. Chem. 24 (1985) 2967.

Quidelleur, S., M. Granet, I. Laszak, H. Isnard, E. Pons-Branchu, R. Brennetot, and C. Caussignac, One step U-Pu-Cs-Ln-steel separation using TRU preconditioned extraction resins from Eichrom for application on transmutation targets, J. Radioanal. Nucl. Chem. 280 (2009) 507.

Rollin, S., Z. Kopatjtic, B. Wernli, B. Magyar, Determination of lanthanides and actinides in uranium materials by high-performance liquid chromatography with inductively coupled plasma mass spectrometric detection, J. Chromatogr. A. 739 (1996) 139.

Rosen, J. B., Kinetics of a fixed bed system for solid diffusion into spherical particles, J. Chem. Phys. 20 (1952) 387.

Rosen, J. B., General numerical solution for solid diffusion in fixed beds, Ind. Eng. Chem. Res. 46 (1954) 1590.

Rudge S. R., M. R. Ladisch, Process considerations for scale-up of liquid chromatography and electrophoresis, Separation, Recovery, and Purification in Biotechnology, Vol 314, ACS Symposium Series, Washington, 1986.

Ruthven, D. M., Principles of Adsorption and Adsorption Processes, Wiley, New York, 1984.

Schweich, D., J. Villermaux, The Preparative chromatographic reactor revisited, Chem. Eng. J. 24 (1982) 99.

Spedding, F. H., A. F. Voigt, E. M. Gladrow, N. R. Sleight, The separation of rare earths by ion exchange. I. Cerium and yttrium, J. Am. Chem. Soc. 69 (1947) 2777.

Spedding, F. H., A. F. Voigt, E. M. Gladrow, N. R. Sleight, J. E. Powell, J. M. Wright, T. A. Butler, P. Figard, The separation of rare earths by ion exchange. II. Neodymium and praseodymium, J. Am. Chem. Soc. 69 (1947) 2786.

Spedding, F. H., E. I. Fulmer, T. A. Butler, E. M. Gladrow, M. Gobush, P. E. Porter, J. E. Powell, J. M. Wright, The separation of rare earths by ion exchange. III. Pilot plant scale separations, J. Am. Chem. Soc. 69 (1947) 2812.

Spedding, F. H., E. I. Fulmer, T. A. Butler, J. E. Powell, The separation of rare earths by ion exchange. IV. Investigations concerning variables involved in the separation of samarium, neodymium, and praseodymium, J. Am. Chem. Soc. 72 (1950) 2349.

Spedding, F. H., E. I. Fulmer, J. E. Powell, T. A. Butler, The separation of rare earths by ion exchange. V. Investigations with one-tenth percent. citric acid-ammonium citrate solutions, J. Am. Chem. Soc. 72 (1950) 2354.

Spedding, F. H., J. E. Powell, The separation of rare earths by ion exchange, Trans. Am. Inst. Min. Metall. Eng. 215 (1959) 457.

Stepinski, D. C., A. V. Guelis, P. Gentner, A. Bakel, G. F. Vandegrift, Evaluation of Radsorb, Isosorb (Termoxid) and PZC as Potential Sorbents for Separation of ^{99}Mo from a Homogeneous-Reactor Fuel Solution, Proceedings of the International Meeting on Reduced Enrichment for Research and Test Reactors, June 20- 22, 2007, Vienna, Austria.

Stepinski, D. C., A. Youker, J. A. Fortner, J. L. Jerden, A. J. Bakel, G. F. Vandegrift, Facts and Myths about Molybdenum Adsorption on Titania and Alumina Surfaces, 34th Annual Actinide Separations Conference, May 17-20, 2010, Argonne, IL, USA.

U.S. Department of Energy, Critical Materials Strategy, 2011.

Vandegrift, G. F., Facts and Myths Concerning ^{99}Mo Production with HEU and LEU Targets, Proceedings of the International Meeting on Reduced Enrichment for Research and Test Reactors, November 6-10, 2005, Boston, MA.

Van Noorden, R., The medical testing crisis, Nature 504 (2013) 202.

Wang, N.-H. L., L. Ling, Ligand-assisted Chromatography for Lanthanides Separation, US Provisional Patent, Application number 62/026,487.

Wetherold, R., E. Wissler, K. Bischoff, An experimental and computational study of the hydrolysis of methyl formate in a chromatographic reactor, Adv. Chem. Ser. 133 (1975) 181.

Wilson, E. J., C. Geankoplis, Liquid mass transfer at very low Reynolds numbers in packed beds, Ind. Eng. Chem. Res. 5 (1966) 9.

Winget, J. O., R. E. Lindstrom, Separation of Rare earth Elements by Ion Exchange, U.S. Patent No. 3,615,173 (1971).

Wu, B., Rare Earth Metallurgy, Chinese Nonferrous Metal Corporation, 1993 (in Chinese)

Xie, Y., S. Mun, J. Kim, N.-H. L. Wang, Standing wave design and experimental validation of a tandem simulated moving bed process for insulin purification, Biotechnol. Prog. 18 (2002) 1332.

Yu, C., S. Mun, N.-H. L. Wang, Theoretical analysis of the effects of reversible dimerization in size exclusion chromatography, J. Chromatogr. A. 1132 (2006) 99.

APPENDICES

Appendix A. Assumptions and equations of VERSE model

The VERSE model and simulations applied in the study were formulated based on the following assumptions: the column has uniform packing and flow distribution; the particles are homogeneous spheres with uniform size distribution, uniform pore size, isothermal behavior, and constant physical properties; all processes within the column are isothermal; the concentration gradients in the radial direction of the column and in the angular directions of the particle are negligible; and effective intra-particle diffusivity is constant. The dimensionless mass-balance equations, initial conditions, and boundary conditions for each component are as follows:

Bulk phase:

$$\frac{\partial c_{b,i}}{\partial \theta} = \frac{1}{Pe_{b,i}} \frac{\partial^2 c_{b,i}}{\partial x^2} - \frac{\partial c_{b,i}}{\partial x} - N_{f,i}(c_{b,i} - c_{p,i,\xi=1}) \tag{A1a}$$

$$x = 0, \quad \frac{\partial c_{b,i}}{\partial x} = Pe_{b,i}(c_{b,i} - c_{f,i}(\theta)) \tag{A1b}$$

$$x = 1, \quad \frac{\partial c_{b,i}}{\partial x} = 0 \tag{A1c}$$

$$\theta = 0, \quad c_{b,i} = c_{b,i}(0, x) \tag{A1d}$$

Pore phase:

$$Ke_i \varepsilon_p \frac{\partial c_{p,i}}{\partial \theta} = N_{p,i} \frac{1}{\xi^2} \frac{\partial}{\partial \xi}\left(\xi^2 \frac{\partial c_{p,i}}{\partial \xi}\right) - \frac{Y_{l,i}}{\varphi_{L,i}} \tag{A2a}$$

$$\xi = 0, \quad \frac{\partial c_{p,i}}{\partial \xi} = 0 \tag{A2b}$$

$$\xi = 1, \quad \frac{\partial c_{b,i}}{\partial \xi} = Bi_i (c_{b,i} - c_{p,i}) \tag{A2c}$$

$$\theta = 0, \quad c_{p,i} = c_{p,i}(0, \xi) \tag{A2d}$$

Dimensionless space, time and concentrations are defined below.

$$x \equiv \frac{z}{L} \text{ (A3a)}; \ \xi \equiv \frac{r}{R} \text{ (A3b)}; \ \theta \equiv \frac{t}{\tau} \text{ (A3c)}; \ \tau \equiv \frac{L}{u_0} = \frac{L\varepsilon_b}{u_s} \text{ (A3d)}$$

$$c_{b,i} \equiv \frac{C_{b,i}}{C_{f,i}} \text{ (A4a)}; \ c_{p,i} \equiv \frac{C_{p,i}}{C_{f,i}} \text{ (A4b)}; \ \overline{c_{p,i}} \equiv \frac{\overline{C_{p,i}}}{\overline{C_{T,i}}} \text{ (A4c)}; \ \varphi_{L,i} \equiv \frac{C_{f,i}}{\overline{C_{T,i}}\left(1-\varepsilon_p\right)} \text{ (A4d)}$$

where z is the column position, r is the position inside the particle, t is the time, u_0 is the mobile phase interstitial velocity ($u_0 = u_s/\varepsilon_b$). $C_{f,i}$ is the feed concentration for component i, $\overline{C_{T,i}}$ is the maximum capacity for component i, $C_{b,i}$, $C_{p,i}$ and $\overline{C_{p,i}}$ are the concentrations of component i in bulk phase, pore phase and solid phase, respectively. Ke_i is the size exclusion factor of the species i. $Y_{l,i}$ describes the net loss of component i in the pore phase due to adsorption to the solid phase at local equilibrium as follows:

$$Y_{l,i} = \sum_{j=1}^{N} \left[\frac{\partial \overline{c_{p,i}}}{\partial c_{p,j}} \frac{\partial c_{p,j}}{\partial \theta} \right] \tag{A5}$$

Appendix B. Analytical correlations for the constant pattern BL curves

For nonlinear isotherm systems, the frontal wave can reach constant pattern if the column is sufficiently long. At the column outlet, the difference in the breakthrough times of two arbitrarily selected breakthrough concentrations $C_{br1}=\phi_1 C_f$ and $C_{br2}=\phi_2 C_f$ with Langmuir isotherm can be calculated as follows (Garg and Ruthven 1975):

$$t_{br2}-t_{br1}=\Delta t=\frac{\frac{1+bC_f}{bC_f}\ln[\frac{\phi_2(1-\phi_1)}{\phi_1(1-\phi_2)}]+\ln(\frac{1-\phi_2}{1-\phi_1})}{K_f\frac{(1+bC_f)(1-\varepsilon_b)}{a}} \tag{B1}$$

where K_f is the lumped mass transfer coefficient in a linear driving force model, and it can be expressed as a function of the intra-particle diffusivity, film mass transfer coefficient, and axial dispersion coefficient for a linear isotherm system (Ruthven 1984).

$$\frac{1}{K_f}=\frac{R^2}{15\varepsilon_p D_p}+\frac{R}{3k_f}+\frac{E_b\varepsilon_b(1-\varepsilon_b)}{u_s^{\,2}} \tag{B2}$$

If ϕ_2 is selected to be 1- ϕ_1, then Eq. (B1) can be reduced to the following form:

$$t_{br2}-t_{br1}=\Delta t=\frac{(-1+2\frac{1+bC_f}{bC_f})\ln(\frac{1-\phi_1}{\phi_1})}{K_f\frac{(1+bC_f)(1-\varepsilon_b)}{a}} \tag{B3}$$

The mass transfer zone length L_{MTZ} in a column for a constant pattern wave equals the product of Δt and the shock wave velocity u_{sh}.

$$L_{MTZ}=(\Delta t)(u_{sh})=[\frac{(-1+2\frac{1+bC_f}{bC_f})\ln(\frac{1-\phi_1}{\phi_1})}{K_f\frac{(1+bC_f)(1-\varepsilon_b)}{a}}][\frac{u_s}{\varepsilon_b+(1-\varepsilon_b)\varepsilon_p+\frac{a}{1+bC_f}}] \tag{B4}$$

Since $a/(1+bC_f)$ is much greater than $\varepsilon_b+(1-\varepsilon_b)\varepsilon_p$, Eq. (B4) can be further simplified.

$$L_{MTZ} = \frac{(-1+2\frac{1+bC_f}{bC_f})\ln(\frac{1-\phi_1}{\phi_1})u_s}{K_f(1-\varepsilon_b)} \tag{B5}$$

If the frontal wave is assumed to be symmetric, then the loading fraction L_f has an analytical correlation with L_{MTZ} and column length L.

$$L_f = 1-\frac{1}{2}\frac{L_{MTZ}}{L} = 1-\frac{(-1+2\frac{1+bC_f}{bC_f})\ln(\frac{1-\phi_1}{\phi_1})u_s}{2LK_f(1-\varepsilon_b)} \tag{B6}$$

If intra-particle diffusion dominates mass transfer, from Eq. (B2) we have $K_f \approx 15\varepsilon_p D_p/R^2$, which can be substituted into Eq. (B6).

$$\begin{aligned} L_f &= 1-\frac{1}{2}\frac{L_{MTZ}}{L} = 1-\frac{(-1+2\frac{1+bC_f}{bC_f})\ln(\frac{1-\phi_1}{\phi_1})}{2}\frac{u_s R^2}{15(1-\varepsilon_b)\varepsilon_p D_p L} \\ &= 1-\frac{1}{2}\left[(-1+2\frac{1+bC_f}{bC_f})\ln(\frac{1-\phi_1}{\phi_1})\right]\frac{1}{15N_D} \end{aligned} \tag{B7}$$

This equation is Eq. (3.8) in Section 3.3.3, which is used to generate the BL curves for any breakthrough limits for constant pattern systems. The correlations for different breakthrough limits (0.05, 0.1 and 0.15) are shown in Table 3.2. Since Eq. (B2) is derived for linear isotherm systems, the leading portion of the frontal curves based on Eq. (B2) for $C_{br}/C_f < 0.05$ is less sharp than the frontal curves obtained from the rate model simulations. For this reason, no correlation equations for $C_{br}/C_f < 0.05$ are shown in Table 3.2. For most applications, accurate measurement of a breakthrough concentration less than 5% of the feed concentration can be challenging, especially for a low feed concentration. Any design based on such a low breakthrough limit, $C_{br}/C_f < 0.05$, cannot

be tested easily. The BL curves for the breakthrough limit of 0.05 in Table 3.2 can meet a yield requirement higher than 98.5% for all Langmuir systems with N_D >0.1.

VITA

VITA

Lei Ling was born to Zhemin Ling and Kangli Zhang on January 28, 1988 in Hangzhou, China. He graduated from the Shenzhen Senior High School in June, 2005. He entered the Tsinghua University in August, 2005. He received his B.E. in Chemical Engineering in July, 2009. He pursued his doctoral degree at Purdue University, West Lafayette, Indiana (USA), under the supervision of Prof. Nien-Hwa Linda Wang. He received his Ph.D. in Chemical Engineering in December, 2014.